A Study of Deactivating Carbon Species during Methanation on a Ni/Al2O3 Catalyst

Olesen, Sine Ellemann

Publication date:
2017

Document Version
Publisher's PDF, also known as Version of record

A Study of Deactivating Carbon Species during Methanation on a Ni/Al_2O_3 Catalyst

Ph.D. dissertation by
Sine E. Olesen

Supervisors:
Ib Chorkendorff
Klas J. Andersson

July 2017

Department of Physics
Technical University of Denmark

Kongens Lyngby

DTU Physics
Department of Physics

HALDOR TOPSOE
CATALYZING YOUR BUSINESS

Contents

Abstract

This Ph.D. thesis describes the research and findings from experimental testing of a methanation catalyst and the characterisation of said catalyst. Methanation is the conversion of syngas (CO and H_2) typically from coal or biomass to methane and water. Methane is the biggest constituent of natural gas and as the infrastructure is already in place for natural gas, it is an attractive alternative to depleting oil resources. Catalysts based on nickel are the most common choice within industry due to the relatively low price of nickel and its acceptable performance. However, nickel catalysts are prone to deactivate due to sintering and carbon deposition. The latter process is not well understood and thus, this work attempted to further the research in low temperature carbon formation. In order to obtain fundamental knowledge, the experimental setup had to be free of impurities and great care was taken to eliminate potential sources. Experiments designed for that purpose established that the influence of sulfur was negligible. Through a series of experiments of temperature programmed hydrogenation (TPH) - methanation - TPH, the carbon build-up during the methanation was studied by the second TPH. Four types of carbon were identified and especially one was found to be the main cause of deactivation. Through x-ray diffraction (XRD) it was established that part of the carbon dissolved into the nickel particles expanding the crystal structure. No carbon was observed during transmission electron microscopy (TEM). Yet by scanning transmission electron microscopy (STEM) energy dispersive spectroscopy (EDS) carbon was discovered in proximity to the nickel particles. However, this was not as well-defined shells and thus, it was deduced that the particles were not encapsulated by carbon. Instead, the carbon was likely very inhomogeneously distributed across the nickel surface, which was supported by remaining activity observed during the methanation tests. Preliminary results on the effect of particle size, temperature and total pressure of methanation showed that especially temperature greatly affected the types of carbon deposited.

Resumé

De eksperimentelle tests udført i forbindelse med ph.d.-projektet, som beskrives i denne ph.d.-afhandling, bestod dels af metaniseringsforsøg med en nikkelkatalysator, dels af karakteriseringen af denne katalysator. Metanisering er omdannelsen af syntesegas (CO og H_2) typisk fra kul eller biomasse til metan. Metan er hovedbestanddelen af naturgas, og da infrastrukturen til naturgas er veletableret, er det et attraktivt alternativ til den snart udtømte olie. Katalysatorer er oftest baseret på nikkel i industrien pga. den relativt lave pris på nikkel og den acceptable aktivitet. Desværre er nikkelkatalysatorer tilbøjelige til at deaktivere pga. sintring og kuldannelse. Kuldannelse er ikke en velbeskrevet proces, og dette projekt har forsøgt at bidrage til en større forståelse af kuldannelse ved lave temperaturer. For at opnå fundamental viden er det essentielt, at opstillingen er fri for urenheder, og der blev derfor foretaget mange tiltag for at eliminere potentielle kilder til bl.a. oxygen og svovl. Eksperimenter designet til formålet kundgjorde, at en eventuel indflydelse af svovl var ubetydelig. Gennem den eksperimentelle procedure; temperaturprogrammeret hydrogenering (TPH) - metanisering - TPH, blev kul opbygget under metanisering undersøgt vha. den anden TPH. Fire kultyper blev identificeret, og især den ene type viste sig at være den deaktiverende. Opløst kul i nikkel-nanopartiklerne, som ekspanderede krystalskrukturen, kunne påvises via røntgendiffraktion. I transmissionselektronmikroskopi (TEM) kunne ingen kulstrukturer observeres. I stedet måltes vha. scanning transmissions elektronmikroskopi (STEM) kombineret med energi spektroskopi (EDS), at kul var i forbindelse med nikkelpartiklerne men ikke i en skal-lignende struktur. Derfor kunne det konkluderes, at kullet ikke omsluttede nikkelpartiklerne, men snarere var uhomogent spredt ud på nikkeloverfladen, hvilket blev understøttet af den tilbageværende aktivitet og problemerne med at se kullet i TEM. Foreløbige resultater omkring effekten af partikelstørrelse, temperatur og totalt tryk viste, at især temperatur har stor indflydelse på, hvilke kultyper, der deponeres.

Preface

This thesis is submitted as partial fulfilment of the Ph.D. degree in physics at the Technical University of Denmark (DTU). The work was carried out at the Department of Physics from October 2013 until January 2017. Professor Ib Chorkendorff and Ph.D. Klas J. Andersson supervised and the project was supported by a research grant (9455) from VILLUM FONDEN and co-funded by Haldor Topsoe A/S. I would like to thank my supervisors for giving me the opportunity to work on a great project and for their help and guidance. It has been a great pleasure. In addition, I thank Christian D. Damsgaard for finding time to become a valuable part of the project, and I am grateful for his efforts.

I thank Debasish Chakraborty for his supervision during my master's, which was the catalyst for me to seek a Ph.D. and for his help to achieve a Ph.D. position. Starting out I was very happy to work in close collaboration with Irek Sharafutdinov, and I thank him for his great work on the design of the VHP setup. I much appreciate the help and time Robert Jensen and Kenneth Nielsen were always ready to give. I also thank Helge Kildahl Rasmussen for the dependable supply of gas bottles, Susanne Kruse & Sinh Hy Nguyen from DTU Environment for ICP MS measurements, Béla Sebök for ISS and XPS and Jakob Kibsgaard for help with my first submission of a paper. I send a large thank you to all the people who helped me proof-read my thesis, a list that includes supervisors, colleagues and friends!

I thank all of my former and current colleagues and students at SurfCat (& CINF) for creating a great work atmosphere and always being available for both fruitful work-related discussions and recreational activities. A special thanks to the running club very much including Jakob Riedel and Claudie Roy, to Brian Peter Knudsen, Karl Toudahl, Hugo Silva and to my office-roommate, Ann-Louise.

I thank my friends and family for being there, both when I needed to talk about work, and especially for when I needed *not* to talk about work! I am forever grateful to Mikkel Stensberg for his everlasting patience and understanding e.g. when experiments ran (very) late and for making my life easier and more enjoyable particularly during the last months.
Last but not least, a huge thank you to all you great people who sent much love my way in the last months. It was hugely appreciated and I feel lucky to have you as my friends!

Sine E. Olesen
Kongens Lyngby
31st of December, 2016

List of Figures

List of Tables

Acronyms

BPR back pressure regulator.

DFT density functional theory.

DOE Department of Energy.

EDS energy-dispersive spectrometry.

FID flame ionisation detector.

FTS Fischer Tropsch synthesis.

FWHM full width half maximum.

GC gas chromatograph.

HRTEM high resolution transmission electron microscope.

ICP-MS inductively coupled plasma mass spectrometry.

ISS ion scattering spectroscopy.

LEIS low-energy ion spectroscopy.

MFCs mass flow controllers.

MS mass spectrometer.

RT room temperature.

SNG synthetic natural gas.

STEM scanning transmission electron microscope.

STM scanning tunneling microscopy.

TCD thermal conductivity detector.

TEM transmission electron microscope.

TOS time on stream.

TPD temperature programmed desorption.

TPH temperature programmed hydrogenation.

wt% weight percent.

XPS x-ray photoelectron spectroscopy.

XRD X-ray diffraction.

List of Publications

Deactivating carbon formation on a Ni/Al_2O_3 catalyst under methanation conditions.
Sine E. Olesen, Klas J. Andersson, Christian Danvad Damsgaard, and Ib Chorkendorff

Published online in the Journal of Physical Chemistry C: 14th of July 2017

DOI: 10.1021/acs.jpcc.7b03754

A study of carbon in and on nickel nanoparticles by XRD and TEM.
Sine E. Olesen, Christian Danvad Damsgaard, Klas J. Andersson, and Ib Chorkendorff

In preparation

1 Introduction

This Ph.D. thesis is about the carbon species that build up on the nickel catalyst during low temperature CO methanation and thereby deactivate the catalyst over time. Methanation is an industrial process producing methane i.e. substitute natural gas which may prove to become an important part in the future energy mix. In this chapter the central concepts such as catalysis and methanation are introduced to prepare the reader for what is to come. An introduction into the relevant literature is also included to establish the foundation on which the work carried out in this Ph.D. project rests and to aid the discussion of results presented in the subsequent chapters. Furthermore choice of experimental conditions and setup is introduced.

1.1 Methanation and catalysis

Methanation is the process of converting synthesis gas (often shortened to syngas), a mixture of carbon monoxide and hydrogen, into methane and water [1]:

$$CO + 3H_2 \rightleftharpoons CH_4 + H_2O \tag{1.1}$$

Conversion of CO_2 to methane is equally called methanation [2] and typically one distinguishes by specifying "CO methanation" or "CO_2 methanation" if necessary to do so.
Methanation is a highly exothermic reaction (for CO methanation: $\Delta H_R^\circ = -206$ kJ/mol [3]) and thus, thermodynamics suggest operation at low temperatures and high pressures as observed by Le Châtelier's Principle [4]. However, the rate of a reaction is commonly increased by increasing temperature because more reactants will have sufficient energy to react, making low temperature kinetically unfavourable. Reactions are governed by thermodynamics but may be influenced by kinetics which are manipulated by catalysis. Catalysis is immensely important for everyday life as e.g. 85-90% of chemicals including chemicals for food production are produced by catalytic processes, and catalysts significantly reduce pollution in

car exhaust. A catalyst accelerates a reaction by providing an alternative route with a lower energy barrier compared to the non-catalysed route. The concept is illustrated in figure 1.1.

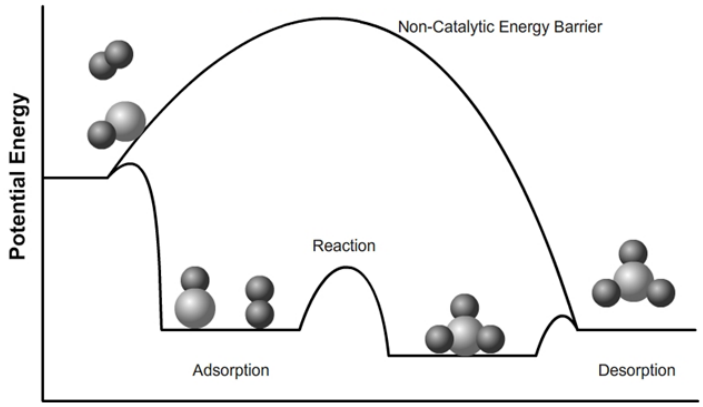

Figure 1.1: Illustration of how a catalyst works by showing the difference in potential energy for the catalysed and non-catalysed reaction. Reprinted from [5].

In principle, the catalytic process is a cycle of adsorption of reactants and reaction intermediates and desorption of products leaving the catalyst unspoiled and non-consumed. The reactants react to form product when sufficient energy is available to overcome the activation barrier and by adsorbing on the catalyst surface, the required activation energy is smaller. This allows for intuitively accepting the Sabatier Principle which states that there is an optimum adsorption strength. If the adsorption is too weak, it will not sufficiently aid the bond breaking but if the adsorption is too strong, the adsorbates will not readily desorb. Therefore an optimum heat of adsorption exists for optimal activity leading to a volcano curve [6]. Overall reactions may involve numerous elementary steps and these are listed for methanation in the table reprinted from [3] in figure 1.2.

(1)	$CO\,(g) + {}^* \rightleftarrows CO^*$
(2)	$H_2\,(g) + 2^* \rightleftarrows 2\,H^*$
(3)	$CO^* + H^* \rightleftarrows C^* + OH^*$
(4)	$C^* + H^* \rightleftarrows CH^* + {}^*$
(5)	$CH^* + H^* \rightleftarrows CH_2^* + {}^*$
(6)	$CH_2^* + H^* \rightleftarrows CH_3^* + {}^*$
(7)	$CH_3^* + H^* \rightleftarrows CH_4\,(g) + 2^*$
(8)	$OH^* + H^* \rightleftarrows H_2O\,(g) + 2^*$

*Figure 1.2: Table of elementary steps in CO methanation. * denotes free adsorption site or adsorbed species. Reprinted from [3].*

Naturally the Sabatier principle is equally relevant for reactants and any intermediates that are involved in the reaction and the descriptor for the volcano curve can be chosen to relate to the rate limiting step. [6] Bligaard et al. [7] plotted the methanation activity based on the dissociative CO adsorption energy for different metals as seen in figure 1.3.

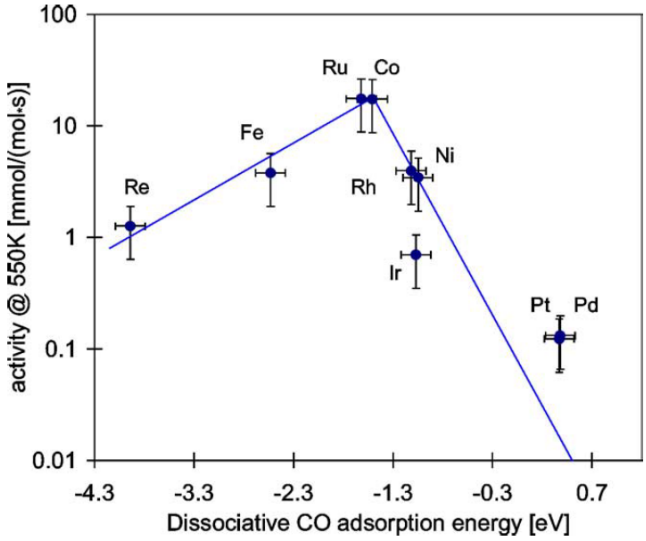

Figure 1.3: The methanation activity for different metals as a function of dissociative CO adsorption energy. Reprinted from [7].

Clearly different metals catalyse the methanation reaction including ruthenium, cobalt, nickel, and iron which was also reported by Vannice [8]. The highest activity is not achieved by nickel as both ruthenium and cobalt are much nearer the top of the volcano. However, the optimum catalyst is not only determined by activity and in practice a catalyst is not unspoiled as surface species deposit on the catalyst during reaction. Thus, parameters such as selectivity towards the sought end product, resistance towards deactivation, non-scarcity of the catalytic materials and structural stability are also important [6]. Nickel is more selective than ruthenium and cobalt towards the production of methane as opposed to higher hydrocarbons [8,9] and significantly cheaper than ruthenium. High selectivity as opposed to activity in combination with being relatively cheap means nickel is the favoured catalytic material in industry[9].

1.2 Motivation for Researching Methanation

Industrially the methanation reaction is well known and has long been used to clean up the hydrogen gas feed in ammonia plants [10,11]. Ammonia is one of the most produced chemicals worldwide due to the use of fertilisers [6] which already suggests the importance of methanation. More recently methanation has also become relevant in the energy perspective via the production of synthetic natural gas (SNG). In October 2013 Haldor Topsoe successfully started Qinghua, the largest SNG plant ever built in the world, in the Northwestern part of China with an annual output of 1.4 billion normal cubic meters of SNG [12]. SNG could renewably be produced from biomass [13–15]. When produced from coal [13,14] it may prolong the use of fossil fuels since coal reserves are significantly larger than oil [16] but also provide a cleaner combustion compared to oil or coal [17,18]. According to the Department of Energy (DOE) of the United States of America worldwide roughly 15 million vehicles are powered by natural gas which have significantly longer range than electric vehicles [19]. As (S)NG is a fuel already extensively used for cooking, transportation, and power generation, the infrastructure for the transportation of (S)NG is largely in place [13]. On top of and due to an existing infrastructure, clean combustion and large or renewable feedstocks, in a future with renewable energy technologies such as sunlight powered and wind powered productions of electricity as well as hydrogen from water splitting, methanation could play an important role in the storage of hydrogen [20,21]. Methane has triple the energy density of hydrogen [22] and can provide a route for CO_2 fixation which may reduce the emissions of CO_2 and lead to CO_2-neutral fuel [23]. Due to both wind and sun being intermittent resources, storage of energy will be paramount and schemes of converting power to gas as exemplified in figure 1.4 are being investigated [21,24–26]. As seen in figure 1.4 the idea could be to use the electricity generated by wind mills or photovoltaics to produce hydrogen through electrolysis. Subsequently the hydrogen could be used directly but e.g. due to legislation limiting hydrogen content in the gas grid, it could instead be converted into methane. Audi visions CO_2-neutral driving with methane powered internal combustion engine vehicles and has ventured into a project with the company SolarFuel. A plant has been built that generates methane ("Audi e-gas") from water and CO_2 derived from biogas through electrolysis and methanation [27]. Haldor Topsoe is similarly part of a project that "upgrades" biogas by converting the CO_2 in biogas to methane via methanation using hydrogen supplied from wind powered electrolysers [28].

Clearly heterogeneous catalysis methanation may continue to be a large scale important industrial reaction in the future especially since selective and efficient electrochemical production of methane is still a challenge [29–31].

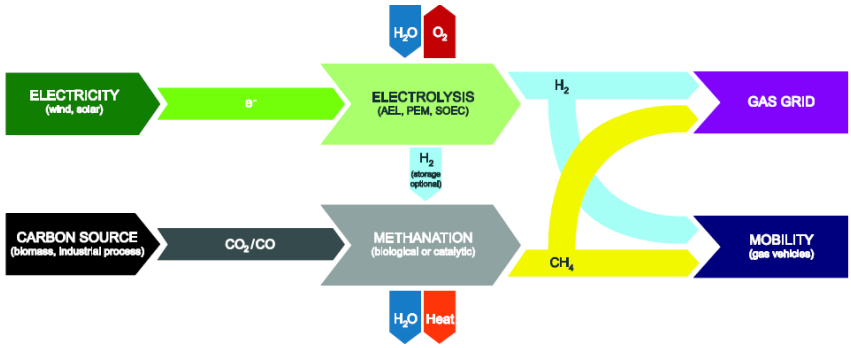

Figure 1.4: Illustration of power to gas concept as a way to store renewably produced electricity. Reprinted from [21].

1.3 Methanation in the Literature

As mentioned, methanation catalysts based on nickel are preferred in industry [2,9] due to a relatively low price and good selectivity towards methane [9]. However, nickel catalysts are prone to deactivation at high temperature through sintering [2,32–34] and at low temperature through carbon deposition [2,34–36]. As the methanation reaction is highly exothermic [3], large temperature gradients may potentially be created within the methanation reactors and as seen industrially in combination with deactivation, the temperature within the catalyst bed may be increased by more than 300 °C very rapidly [34]. This could explain why high temperature effects like sintering are well-studied [33] but the focus of this Ph.D. project is the low temperature carbon formation. The literature is extensive and multiple reviews have been written on carbon formation and deactivation [36–38]. However, reaction conditions like partial pressure of CO and reaction temperature hugely affect the deactivation and which carbon structures are involved [2] so not all literature is as relevant as it first appears. In the following paragraphs an overview of the reported results and findings most relevant for this work is presented loosely structured in an order of appearance.

1.3.1 Carbon on Nickel

Surface carbon may be categorised based on its reactivity with H_2, which dates back to McCarty and Wise [39], who after exposing a nickel alumina catalyst to CO at 550 K assigned the terms "α"-carbon and "β"-carbon to chemisorbed carbon atoms (highly reactive carbon) and polymerised amorphous carbon (less reactive carbon) respectively. They also discussed that α-carbon (C_α) was unstable and could be converted into the more polymerised β-carbon (C_β) and at higher temperatures could further transform into graphite. In addition, they assigned an γ-phase to bulk nickel carbide. There was no discussion of deactivation by carbon. The review by C. Bartholomew [36] on carbon types kept in line with this nomenclature though he specified that polymerised carbon could include amorphous films

(C_β) and filamentous or whiskers carbon (C_V). A main conclusion was that which specific types of carbon were formed was highly sensitive to the reaction temperature. It was reported that carbon formed below 325 °C was carbidic and above 325 °C it was polymerised. Also though only discussed very briefly, it was observed that different carbon types deactivated through different mechanisms and not all deposited carbon species led to deactivation. Agrawal et al. [40] (briefly referenced by Bartholomew [36]) studied carbon deactivation at 548 K and 673 K at atmospheric pressure in 1 % and 4 % CO in H_2 on nickel as well as ruthenium, cobalt, and iron. They showed that ruthenium and nickel behaved similarly whereas cobalt and iron also appeared similar but significantly different compared to Ni and Ru. Slow deactivation was observed on both nickel and ruthenium and although only carbon was observed on nickel, it was expected that carbon was the cause of deactivation and by auger electron spectroscopy they assigned carbon on nickel to graphitic carbon. Both the Ni and Ru catalysts could be fully regenerated by treatment with hydrogen at 673 K. The catalysts of Co and even worse Fe deactivated severely, could not be regenerated, and evidence of both graphite and bulk carburisation was found.
Gierlich et al. [35] reported that deactivation during methanation in the temperature range of 300-350 °C was caused by carbidic carbon becoming polymerised carbon that encapsulated the nickel particles. However, no actual characterisation of the carbon was included in the article.
Mirodatos et al. [41] noted two types of carbon formed during methanation on nickel supported on silica in the temperature range of 473-523 K. By temperature programmed hydrogenation (TPH) they assigned the low temperature carbon to surface carbide but the higher temperature carbon was unassigned though suggested to be deactivating. In a later bigger study by Mirodatos et al [42] carbon deactivation during methanation on Ni/Al_2O_3, Ni/MgO, and Ni/SiO_2 was studied for various times on stream up to 40 hours. Three carbon types distinguished by TPH were observed at low (<523 K), intermediate (523-723 K), and high (∼780 K) temperature. The low temperature carbon ("reactive carbon") was assigned to surface carbide and the amount was found to be independent of time on stream (TOS), pressure, and support. The intermediate species, not found on the silica catalyst, were assigned to be formate species by infrared spectroscopy analysis. The high temperature carbon increased with TOS and after regeneration at 873 K, it built up again during reaction conditions. It was speculated that the 780 K carbon was the main cause for deactivation and suggested that it was amorphous or graphitic or whisker-like. Comparable findings were published by Hayes et al. [43,44] who found that there was evidence of more than one type of carbon as well as a transformation from more active to less active species. When larger deactivation had occurred, a higher temperature hydrogen treatment was required to regenerate the catalyst. X-ray photoelectron spectroscopy spectra showed graphitic-like species though not entirely graphite. Carbon reacted off by hydrogen at higher than 600 K was found to increase in quantity with time in stream and to shift up in temperature when deposited at higher temperature. It was speculated that these high temperature TPH species were some structured amorphous carbon and

the cause for deactivation.
The carbon studies done by disproportionation of CO [36,39,44] have clearly shown that different carbon species may be built up on the catalyst surface and that the temperature during the carbon deposition is an important parameter. However, not only temperature is a key parameter but the presence of hydrogen hugely affects both which types and in which quantities carbon species may be formed [41,43,44]. Hayes et al. [43] showed by electron microscopy that filamentous carbon was not formed in hydrogen-rich environments while Mirodatos et al. [41] saw that only surface carbide was formed in the presence of hydrogen as opposed to formation of bulk carbide during CO disproportionation. Interestingly, CO methanation at high temperature results in the formation of filamentous carbon even in hydrogen-rich environments on nickel catalysts [45,46] as well as ruthenium catalysts [47]. As steam reforming is commonly done at higher temperature than methanation [36] and since whisker formation primarily occurs during high temperature methanation, it is reasonable that the main carbon species deposited during steam reforming are whiskers [48] but pyrolytic and encapsulating species are also formed [49].
It is clear that the exact conditions are extremely important and therefore the massive literature on carbon formation must be critically evaluated.

1.3.2 The active site and carbon chemistry

In order to develop the most active catalyst possible for any reaction, the number of *stable* active sites must be maximised which of course requires knowledge on what the active site is. Surface science studies on nickel single crystals with the methanation perspective in mind have been performed. Early studies e.g. by Madey et al. [50] and Kelley et al. [51] suggested that the methanation reaction was structurally independent because similar turnover rates for CO hydrogenation were found for Ni(1 1 1), Ni(1 0 0), and for high surface area (polycrystalline) catalysts. However, more recent studies have shown that Ni steps are significantly more active for CO dissociation. By poisoning the steps on Ni(14 13 13) with as little as 0.05 monolayers of sulfur, the CO dissociation was virtually stopped and hardly no carbon was deposited on the nickel surface [52]. Andersson et al. [53] who did surface science experiments as well as density functional theory (DFT) calculations similarly concluded that in ultra-high vacuum without hydrogen present only the steps were active for CO dissociation. In addition when hydrogen was present, the steps were still significantly more active in the dissociation of CO and the group provided evidence that the dissociation occurred via a transition state of COH, also the rate limiting step. DFT calculations by Bengaard et al. [54] also point to that nickel step sites are more active for CO dissociation than terraces and other facets. Step sites under steam reforming conditions thus acted as nucleation sites for graphite formation and the growing onto the Ni(1 1 1) facets was found to be slow process. As graphite formation is initiated at the steps, it was also reported that graphite formation can be completely suppressed by blocking the step sites. On Ni(1 1 1) Yang et al. [55] did very detailed studies of the chemistry of

CH_x adsorbates and found that above 250 K carbon species coupled to form C_2H_2 which could further transform into benzene-like rings and eventually polymerise into cyclic hydrocarbons. Detailed surface science studies are highly informative and may provide a lot of knowledge on stabilities of various adsorbates as well as the formation of carbon structures. However, due to experimental limitations (incompatibility of high pressures of hydrogen with high vacuum conditions) [56] none of the surface science papers include TPH results, so it is difficult to directly compare to the TPH results on supported catalysts. Both types of studies are necessary and compliment each other and together they may paint a more enlightened picture.

1.3.3 Fischer-Tropsch and Cobalt

As will be clear later in this thesis, results reported in Fischer Tropsch synthesis (FTS) literature match the results in this Ph.D. well. Therefore a quick summary of selected results and papers that will be referenced later is briefly presented. FTS is the conversion of CO and H_2 into long chain hydrocarbons and typically cobalt is the catalyst of choice [57]. With a similar initial gas composition as methanation and a catalyst with similar surface carbon chemistry as nickel [58], it is reasonable to expect some common ground.
Characterisation after FT reaction show different carbon types on the cobalt surface including surface carbide and polymeric carbon [56,57,59–61]. Polymeric carbon has been reported to be the most relevant in terms of deactivation by carbon [60,61]. Weststrate et al. [56,62,63] have submitted a detailed carbon chain growth mechanism on cobalt motivated by understanding deactivation through carbon formation during FTS, proposing that polymeric carbon formed via a side reaction is the most relevant in terms of deactivation by carbon. Through a thorough analysis of their data as well as published activity data, DFT, scanning tunneling microscopy (STM) data etc. it is suggested that cyclo-polymerisation is based on CH-species (methylidyne) coupling to form C_2H_2-species (acetylene) which rearrange to ethylidyne onto which another CH is coupled forming propyne which again becomes propylidyne and so on and so forth. This is in good agreement with the mechanism of chain growth on Ni briefly described above presented by Yang et al. [55].

1.3.4 Challenges

The literature on methanation and carbon deposition on nickel is clearly extensive. However, a number of highly relevant questions have yet to be answered, some of which this thesis attempts to be useful in answering. Although numerous studies have focused on deactivation by carbon and it was reported that more carbon resulted in higher degree of deactivation [42], no studies have quantitatively correlated the catalyst deactivation during low temperature methanation with surface carbon. Despite many important findings on deactivating carbon, the morphology, location, and distribution of this carbon on the nickel nanoparticles remain

unknown and though the carbon has been categorised in different types, it is unclear whether these are hydrogenated structures. Experimental conditions have been shown to be crucial for carbon formation but a detailed understanding is still lacking.
Building on prior knowledge it was attempted in this Ph.D. project to provide evidence and insights into carbon deactivation at low temperature CO methanation. Better understanding of the deactivating carbon structures and the formation process may aid the design of catalysts more resistant towards carbon formation and consequently aid the development of better catalysts.

1.4 The experimental platform

The motivation for understanding carbon formation at low temperature methanation is to push towards a more efficient process industrially and therefore the experimental conditions in this work was chosen to provoke carbon formation at low temperature methanation. Industrially the gas feed may originate from e.g. coal or biomass gasifiers which results in a feed containing in addition to CO and H_2 also significant amounts of various gasses such as H_2O, CO_2, and CH_4 as well as poisons such as sulfur [13]. Including mild oxidants in the gas stream such as H_2O and CO_2 greatly reduces the potential for carbon formation [36] meaning the conditions in this work were quite harsh. Thus, the degree of deactivation in our experiments (where such oxidants were omitted and at low temperature) may be exaggerated compared to optimal and industrial conditions. However, no poisons were co-fed either. Sulfur is known to be an impurity/poison that reduces the catalyst activity greatly, and can lead to a faster and more detrimental carbon deposition during CO methanation conditions [35,64]. Published results suggest that the carbon involved in methanation and sulfur are in competition for adsorption sites on nickel [65,66]. Part of the motivation for this Ph.D. project was to perform the research sulfur-free to study more fundamental deactivation by carbon and this work was therefore carried out with much awareness of potential sulfur sources as well as attempting to minimise sulfur effects. The activity setup was designed for the dual purpose of methanation and higher alcohol synthesis. It was built during the first months of this project, meaning that no previous sulfur experiments could have impaired it. Furthermore, the setup was fitted with a catalyst functioning as an absorber to capture any potential impurities including sulfur, high purity gasses were used and the setup was always thoroughly pumped out after having been open to the atmosphere, where sulfur is present.
In a fashion the setup was built to bridge the gap between well-controlled surface science experiments and industrial realistic pilot plant tests. Therefore certain functionalities such as elevated temperature and elevated pressure were required in combination with the well-defined conditions such as clean gas supply.

1.5 Outline of the thesis

This thesis is divided into seven chapters following this introduction. In **chapter two** the activity setup and characterisation methods are described, followed in **chapter three** by presenting the experiments that are prerequisite to further analysis of data e.g. demonstrating negligible influence of sulfur. In **chapter four** the experiments producing the main findings are described and the carbon species of these experiments are discussed in **chapter five**. In **chapter six** preliminary results on the effect of changing the methanation temperature and pressure as well as particle size are described. **Chapter seven** provides a short motivation on what would have been a neat experiment and **chapter eight** summarises the findings.

2

Experimental Foundation

In this chapter the experimental setup and the characterisation techniques employed during this Ph.D. project are described. Most of the data presented later in the dissertation was achieved from measurements in the experimental setup and thus the setup and the related technologies are the main focus of this chapter. It was designed and built during the first year of this Ph.D. and experimental procedures were established and improved during the second year, all of which was a time-consuming process. Although changes to the setup were made along the way, the setup is described as it appeared at the end.

2.1 The Setup

The setup for activity measurements and in-situ characterisation by temperature programmed hydrogenation (TPH) and temperature programmed desorption (TPD) is located at DTU Physics in building 312. It is known as the "Very High Pressure Setup" or VHP setup for short (very high pressure because 1 bar is considered high pressure in building 312). The schematics of the VHP setup is presented in figure 2.1. In general terms the flow controlled by mass flow controllers (MFCs) and cleaned by a $Cu/Zn/Al_2O_3$ absorbing catalyst is sent through the catalyst-filled plug-flow reactor, which is placed inside a furnace and the exit gas is measured on stream by a mass spectrometer (MS) and a gas chromatograph (GC). A more detailed description is provided in the following sections based on the various parts.

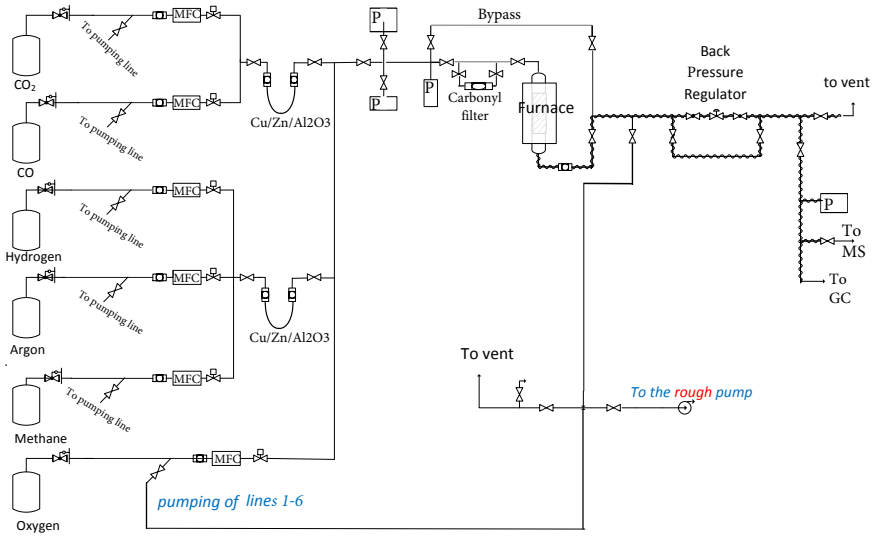

Figure 2.1: Schematic of the experimental setup.

2.1.1 Gas handling

The setup was built of mostly 1/8 inch tubing using copper sealed VCR connections and standard VCR components supplied by Swagelok. Upstream components were used that are compatible with up to 100 bar. There were six permanent gas lines on the VHP setup. Each gas was provided by a 50 l gas bottle of purity 6.0, if available, supplied by AGA. Brooks mass flow controllers (MFCs) with 0-100 ml/min range controlled the flow and to limit small leaks through the MFCs, a high pressure pneumatic valve was connected in series immediately after each MFC. To absorb impurities such as oxygen and sulfur from the gas supply, the gasses were directed through a reduced $Cu/Zn/Al_2O_3$ catalyst at room temperature (RT) placed in U-shaped reactors. CO and CO_2 were mixed and sent through one such U-reactor and H_2, Ar, and CH_4 were directed through another. Oxygen was not cleaned but also little used. By high pressure needle valves the gas could be led through three routes: the bypass of the catalyst-filled reactor, through a commercial carbonyl trap (Pall Gaskleen Purifier) and into the reactor, or bypassing the trap i.e. directly to the reactor. For flows entering the reactor, the carbonyl trap was *not* bypassed, unless oxidising flows were used. Exiting the reactor the gas was sent through the back pressure regulator (baumann 51000), which controlled the pressure upstream. It was possible to bypass the back pressure regulator (BPR) but as the BPR allows the setup to be at ambient pressure, this was never necessary. After the BPR, the gas passed at ambient pressure, no matter the upstream pressure, past the glass capillary which acted as a sniffer to the mass spectrometer (MS), following the principles described by B. Kasemo [67] and further through to the gas chromatograph (GC) from where it was vented. After the reactor before the BPR, a tube led to an oil-free roughing pump, which through the reactor could

pump down all gas lines from the pneumatic valves in front of the MFCs to the pneumatic valve in front of the GC to the low mbar range. Only pneumatic valves were involved in pumping down the tubing which meant this could be automated in the experiments, whereas the directing of flow through bypass or reactor by needle valves needed to be done manually.

2.1.2 The Plug-flow Reactors and Considerations Concerning Them

There are many reactor designs available but according to the ten commandments for testing catalysts, reprinted in [6], plug-flow reactors or continuously stirred tank reactors are typically preferred for laboratory use. According to Hill [68] the best direction of flow is downward minimising catalyst movement, and the direction of vhp-setup is indeed downward. Another of the ten commandments is that the diameter of the reactor should be at least 10× that of the catalyst particles's diameter and the catalyst bed should be at 50× that of the catalyst particles's diameter[6]. The reactors were Ti-enhanced steel tubes with an inner diameter of 3.87 mm and an outer diameter of 6.35 mm (1/4 inch). The length was 55 cm. Catalyst particles were sieved and selected to sizes between 100-300 µm, satisfying the commandment of reactor diameter being at least 10 times that of the particles. Equally, the catalyst bed would be required to be at least 1.5 cm to satisfy the commandment which was also the case. Temperature gradients must be avoided, as the catalyst activity is highly dependent on temperature. One way to minimise temperature gradients is to keep conversion low by diluting the catalyst with inert material [6]. The catalyst was diluted for testing and initial conversion was limited to ∼15%. To prevent nickel carbonyl formation from the CO flow and the nickel in the steel, the reactors were glass coated by SilcoTek prior to use. VCR-fittings were welded compatible with high pressures.

2.1.3 Mass Spectrometry

As is described above in section 2.1.1, the exiting gas was analysed by mass spectrometry (MS) and gas chromatography (GC). It was a strong combination as the MS provided excellent time resolution, whereas the GC provided high sensitivity towards hydrocarbons. Here the technical details behind MS is described in brief based on literature provided by Pfeiffer Vacuum GmbH [69,70] and in section 2.1.4 the GC will be described.
Mass spectrometry is the analysis of gaseous compounds by ionisation and filtering a mass-to-charge ratio. It is a complex vacuum system that includes an inlet, the ionisation filament, the quadrupole rods, and ion detection and a pressure gauge as illustrated in figure 2.2.

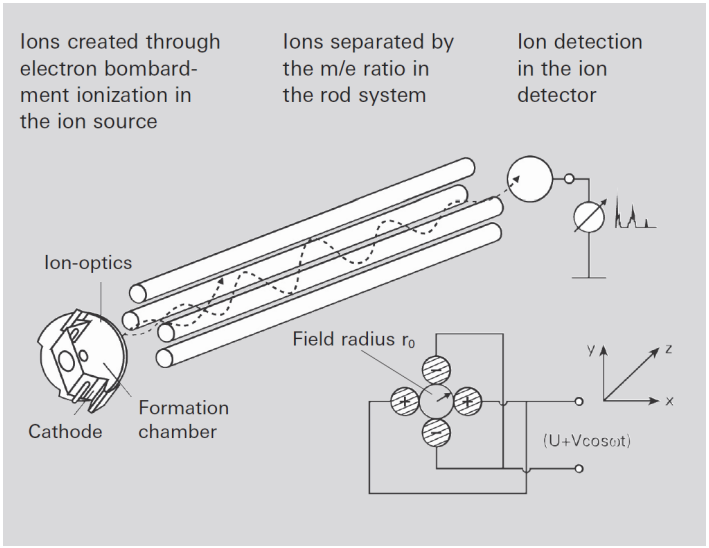

Figure 2.2: Details of the quadrople mass spectrometer. Reprinted from [70]

.

As mentioned, a thin quartz tube allowed for operation at ambient pressure and mass detection at 10^{-7} mbar range and thus, only a small fraction of the gas is analysed. The gas molecules are ionised in the formation chamber upon impact with low energy electrons emitted from the heated filament (metal wire). The electrons are accelerated by an electric field and knock out valences electrons of the gas molecules creating positive ions. The success rate of ionisation is dependent on the energy of the ionisation electrons, where maximum yield is found for acceleration voltages between 50-150 eV. As well as ionising the molecules, some with a single charge and some with multiple charges, the molecules are also fragmented and charged, sometimes doubly charged, giving rise to the distinct mass spectrometry patterns found in tables for each element e.g. as methane seen below in figure 2.3.

Typically, one must be attentive to the fragments as well, as they provide information on how to distinguish between different molecules and how to best measure a compound. The exact collection of the charged molecule and its fragments are dependent on the ionisation energy and the specific mass spectrometer and might therefore vary slightly compared to tabulated values. The ions are directed through a slit to mass analysis by a small potential difference and enter with similar energies. The separation based on mass-to-charge is done by four rods which are pair-wise connected and a quadrupole electric field is applied by a combination of a DC voltage and an AC voltage of a certain amplitude and frequency, deflecting the ions travelling through. By tuning of the ratio between the DC and the AC components of the field, only selected mass-to-charge ions reach the detector. To create a full mass spectrum the quadrupole electric field is varied to scan across m/z values. The detection was based on a Faraday cup converting the ion currents

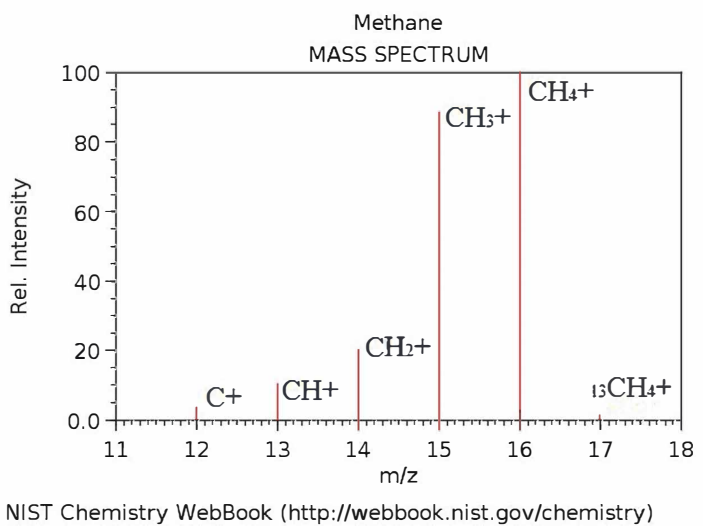

Figure 2.3: The ionisation of methane provided by NIST Chemistry WebBook [71] with captions added by author.

.

into voltage and a secondary electron multiplier for amplification.

Specifics of the MS on the VHP Setup

The quadrupole mass spectrometer is a QMA 125 with a tungsten axial beam filament. The SEM was set to 2000 V, the ionisation energy was 70 eV, and in operation the typical pressure was 7×10^{-7} Torr.

2.1.4 Gas Chromatography

The mass spectrometer measures simple molecules very well and with excellent time resolution. However, because of the cross-over due to fragmentation of the molecules, bigger molecules are more sensitively measured by a gas chromatograph (GC). First, the overall technical aspects are briefly described in this section. Then a description of the specific GC on the VHP setup follows, the detailed diagram of which can be found in appendix A.

The GC separates the analyte in its component due to differences in retention times within the GC columns. A simplified schematic of a GC is seen in figure 2.4. The inert carrier gas brings the analyte from the inlet to the column(s), which are either packed columns or capillary columns. The packed column is packed with a solid material coated by a stationary liquid layer which the sample interacts with. Dependent on the interaction, different elements will be retained for different amounts of time. The capillary column works in a similar fashion but although significantly thinner and longer, the coating is also much thinner, reduc-

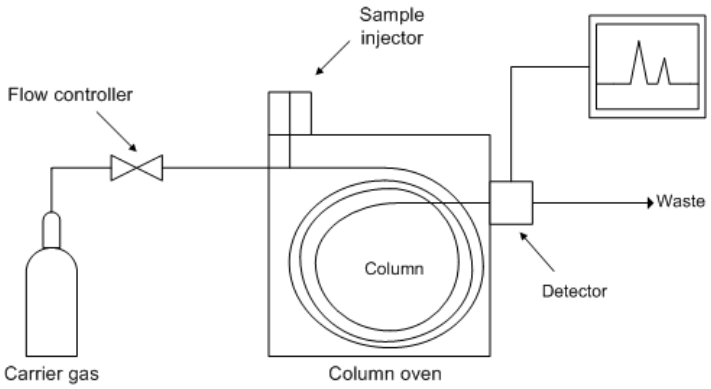

Figure 2.4: Simple schematics of a GC. Reprinted from [72]

.

ing the over-all time the samples spend in the column. Generally, the resolution is much higher for capillary columns. The columns are placed in an oven, and the temperature greatly affects the retention time of different compounds in the columns. The suitable temperature is dependent on the boiling point of the compounds and the separation required. The pressure set on the columns by the carrier gas equally affects the retention time and a suitable relation between temperature and pressure must be found. Many types of detectors are available, but two types of detectors are relevant for this Ph.D. project: flame ionisation detector (FID) and thermal conductivity detector (TCD). In the FID the sample is burnt in a hydrogen-air flame, and thus only flammable gasses can be detected excluding e.g. argon. Organics produce ions when burnt in the flame, which may be measured by applying a voltage between the tip where the flame is produced and the electrode. The ion current is directly correlated to the amount of carbon atoms, making the FID very sensitive to hydrocarbons. The TCD is based upon the resistance change in a filament when it is heated up due to the sample reducing its thermal conductivity and is a comparison of the sample-affected filament versus the reference filament. The signal is dependent on gas concentration and unlike the FID, all gasses can be detected although with significantly lower sensitivity compared to the FID. [73]

Specifics of the GC on the VHP Setup

The GC connected to VHP setup was bought from Agilent Technologies. It was equipped with two FIDs, one TCD, and five columns. The concept is of course the same as in the generic simplification seen in figure 2.4 and all columns were placed in the same oven and thus, were subject to the same temperature. However, the exhaust gas from the VHP setup flowed to the front inlet of the GC, and in "OFF" mode filled/injected three sample loops in series, one for each detector. These loops could have had different carrier gas, and pressure in each loop was controlled individually, making up for the same temperature in the column. In addition,

rather than keeping the oven temperature constant, it was ramped up after each injection during the measurement, affecting the retention time in the columns and aiding separation between species. Also multiple columns and controllable valves in the same sample loop allow for having some sample in a "waiting" column to be measured later to aid the separation. While the sample loops are filled when the valves are in "OFF" mode, the carrier gas is sent through the columns emptying these and sending the analyte in these through to the detectors. When the mode is "ON", the carrier gas is carried through the sample filled loops, emptying these and sending the analyte into the columns.
The interplay between temperature in the oven and pressure set by the carrier gas as well as which valves are "ON" or "OFF" is governed by the method/recipe. Different recipes can be defined depending on needs such as short measurement duration or expertly separation of certain elements but it is essential to empty the columns in each injection. In this work mostly the same recipe was used for all measurements because all measurements were similar in analysed gas components. Also, the mass spectrometer ensured high time resolution and thus, it was not necessary to optimise the GC recipes with respect to time for different needs.
One FID is connected to a capillary column which was dedicated to methane and other hydrocarbons, allowing for excellent distinction between these. In front of the second FID a "methaniser" converted carbon monoxide to methane, giving a much lower detection limit than if CO had to be measured by the TCD, which was mainly used for measuring argon and hydrogen. The resulting spectrum of the methane flows 10 ml/min CO, 40 ml/min H_2 and 50 ml/min Ar sent through bypass of the reactor is seen in figure 2.5. The areas under the peaks were converted to molecular quantities by having calibrated with known quantities previously. These values, when bypassing the reactor, acted as a check, whether the columns were changing over time and needed to be recalibrated. In figure 2.5, it is seen that CO was detected by all detectors but equally, it is seen that the peak for the second FID is by far the strongest. Because of the similar thermal conductivity between helium (reference gas) and hydrogen, hydrogen is measured negatively in the TCD.

In figure 2.6 the result on the first FID of an injection during methanation at 300 °C with with 10 ml/min CO, 40 ml/min H_2 and 50 ml/min Ar is presented. It indicates the excellent hydrocarbon sensitivity mentioned which is achieved by a combination of a capillary column and the detector type as well as a well chosen recipe. In order to distinguish between close lying peaks, the software was set to register even very small changes to the background and therefore "peaks" that do not represent a proper peak or elements in very minor quantities are also registered.

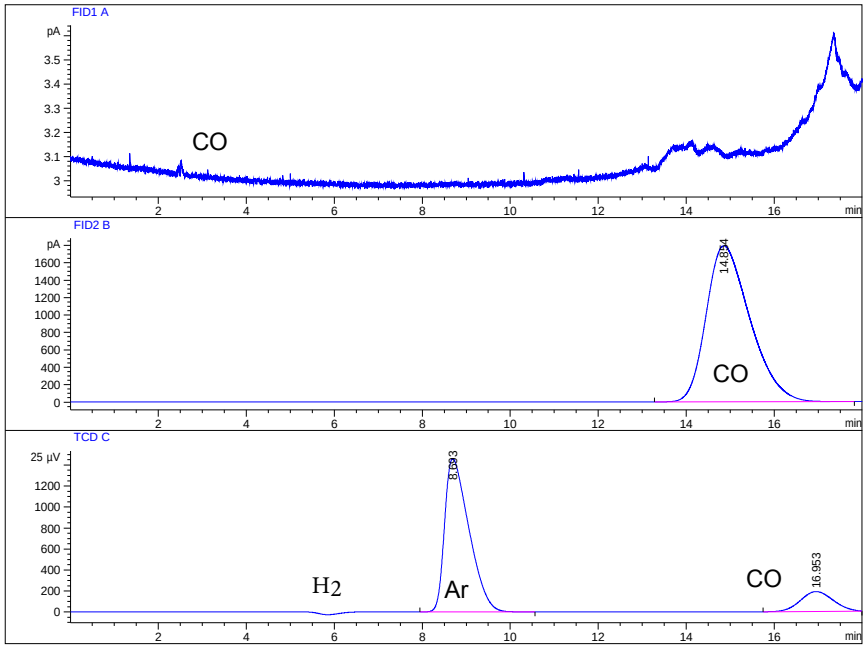

Figure 2.5: The GC response to the methanation flow of 10 ml/min CO, 40 ml/min H_2 and 50 ml/min Ar

.

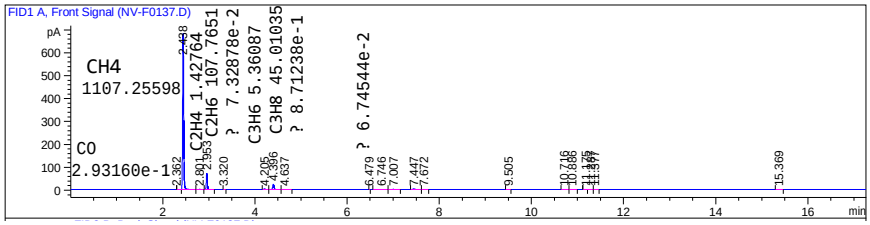

Figure 2.6: The FID1 signals of an injection during methanation at 300 °C with 10 ml/min CO, 40 ml/min H_2 and 50 ml/min Ar. Selected peaks are labelled by element and area in pA·s.

.

2.2 Characterisation Techniques

The main characterisation technique employed in this Ph.D. is X-ray diffraction (XRD). Other methods used briefly and typically to a very specific end include ion scattering spectroscopy (ISS), x-ray photoelectron spectroscopy (XPS), transmission electron microscope (TEM), scanning transmission electron microscope (STEM) energy-dispersive spectrometry (EDS), and inductively coupled plasma mass spectrometry (ICP-MS). In order to reflect their importance and the extent

of their use as well as time spent, only XRD, XPS and ISS are described in the following sections. Primarily the fundamentals and technical details that explain how and why a certain method is used are in focus. Methods used only fairly limited are presented in connection with the data discussion, these include TEM, STEM EDS, and ICP-MS.

2.2.1 X-Ray Diffraction

X-ray diffraction (XRD) is a characterisation technique often used in catalysis which can provide structural information such as crystallite phases and sizes and can be performed both ex-situ and under reaction conditions [6].
The following introduction into crystal structure and x-ray diffraction theory is based on the textbook by L. Gerward [74] and crystal structure specifics on nickel are reported based on [6].
XRD is the study of materials by x-rays that are directed towards the sample and are subsequently scattered by said sample, whereby a distinct diffraction pattern based on the sample's crystal structure is formed. Crystalline materials are made up of periodically repeated building blocks; unit cells of atoms. The position of the atoms in the cubic unit cells are defined by the lattice constant and the planes in cubic lattice are described by the miller indices. Different elements crystallise in different structures with a unique lattice constant. In figure 2.7 examples of crystal planes and their miller indices are illustrated.

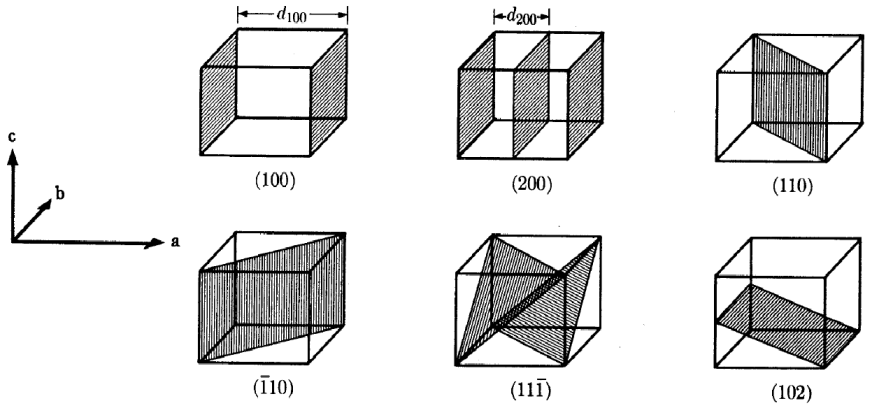

Figure 2.7: Illustration of lattice planes described by miller indices. Reprinted with minor alterations from [74]

.

The spacing between the planes is called the lattice spacing which can be related to the lattice constant and the miller indices:

$$\mathrm{d_{hkl}} = \frac{\mathrm{a}}{\sqrt{h^2 + k^2 + l^2}} \tag{2.1}$$

where d = lattice spacing, a = lattice constant, and hkl = miller indices of the plane.
The lattice spacing is what is analysed in XRD on the basis of Bragg's law which states that constructive interference between the scattered incoming x-rays only occurs for a crystalline structure in the directions where the path difference of the scattered waves is an integer of the incoming wavelength:

$$\mathrm{n}\lambda = 2\mathrm{d}\sin(\theta) \tag{2.2}$$

where n = order of diffraction, λ = radiation wavelength, d = lattice spacing, and θ = the angle of diffraction. In figure 2.8 the principle is illustrated with d and θ labelled.

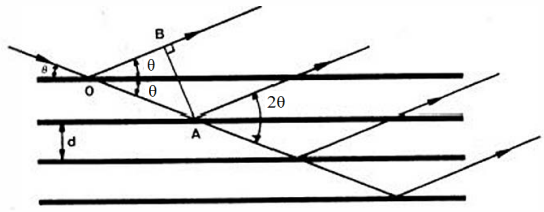

Figure 2.8: Illustration of Bragg diffraction. Reprinted from [74]

.

The order of diffraction, n, can be related to the diffracting planes. Diffraction of the (220) plane can be seen as the first order of this plane or the second order of the (110) plane therefore setting n to 1 will mean that the d-spacing is that of the plane from which the diffraction occurred.
The X-rays for XRD are generated in the anode of the equipment and because x-rays are characteristic for the element from which they originate, the material chosen for anode dictates the wavelength by which the diffraction is measured. Copper is often chosen as anode material because the wavelength of 1.54 Å is sufficiently small to resolve crystal unit cells and the radiation spectrum for Cu is quite simple with a strong signal for the $\mathrm{K}_{\alpha 1}$.
Naturally, only planes oriented in a way that enable the diffracted waves to reach the detector are measured but when measuring on a powder sample, all planes are randomly distributed and by scanning across a range of angles, the diffraction pattern is an average of all planes in the sample. Bragg's law assumes an infinite crystal, which means that realistic samples of finite thickness give a peak broadening related to the crystallite size. This is expressed by the Scherrer equation:

$$B = \frac{K \cdot \lambda}{D\cos(\theta)} \tag{2.3}$$

where B = the broadening, K = the shape factor, λ = radiation wavelength, D = diameter of crystallite, and θ = the angle of diffraction. In practice, the B is the full width half maximum (FWHM) of the peak and K is 0.9 assuming spherical particles.
The diffraction pattern of specific crystal structures are indicative of the material which by use of reference patterns found in databases can be identified. Nickel for instance crystallises in a face centred cubic (FCC) structure with a lattice constant of 3.52 Å.
Thus, diffractograms yield the crystal structures with different planes being evident in the sample and these patterns can thus be analysed to give the present phases as well as crystallite size.

Specifics of XRD used for this work

The XRD equipment employed for this Ph.D. work was a PANalytical Empyrean with Cu $K_{\alpha 1}$ radiation of 1.541 Å that had a diffracted beam monochromator fitted.

2.2.2 X-Ray Photoelectron Spectroscopy

This section and the following section on ISS are based on literature from [6],[75]. The sections do not venture very far into the theory of these techniques and especially XPS is somewhat more complicated because of transportation loss mechanisms and atomic relaxations. Like XRD, XPS is a very common characterisation technique but because it relies on the detection of ejected electrons from the sample which have a relatively short mean free path, it is a much more surface sensitive technique. XPS is based on the photoelectric effect which is the process of electrons being emitted due to their absorption of sufficient photon energy. As the electron structure of materials is unique, XPS is a surface sensitive technique that yields information on the elements present in the sample and their oxidation state. The energy of the photoelectrons carry information about the photon energy and the energy level whence it came. The kinetic energy of the emitted electrons are detected by the energy analyser and the relation to their binding energy in the material is given by:

$$E_k = h\nu - E_b - \Phi \tag{2.4}$$

where E_k is the kinetic energy of the generated photoelectron, h is Planck's constant, ν is the radiation frequency, E_b is the binding energy of the generated photoelectron with respect to the Fermi level of the sample, and Φ is the work function of the spectrometer doing the detection of the photoelectron.
The intensity of the photoelectrons is measured as a function of their kinetic energy and through equation 2.4, the kinetic energy is converted into binding energy. The binding energy, as mentioned, is characteristic of the element as well as the element's chemical state whence it originated. Converting to a binding energy regime although kinetic energy is what is being measured means that spectra are

more readily analysed and different spectra from different equipment are easily compared. Naturally, the photon energy defines how deep into the energy levels, electrons can be emitted. Typically aluminium or magnesium anodes are used as these emit sufficiently high energy to reach the core level electrons. Not only does the binding energy provide information about which element but also the quantity (by relative electron density for different materials and ionisation cross section) and chemical state (by shifts in binding energy e.g. an oxidised state). However, quantification also requires a good background subtraction and knowledge of the sample to account for non-uniform distribution of elements in the sample and the accuracy is limited. XPS peaks are labelled by the quantum numbers of the originating level and the spin.

Specifics on the XPS used for this work

XPS was done in vacuum chamber provided by Scienta Omicron, which had a base pressure of roughly 10^{-11} mbar and was equipped with a SPECS XR 50 X-ray gun coupled to an Omicron NanoSAM 7 channel energy analyser. MgK_α radiation was used.

2.2.3 Ion Scattering Spectroscopy

Ion scattering spectroscopy (ISS) or low-energy ion spectroscopy (LEIS) is even more surface sensitive than XPS. In ISS low-energy light ions (H^+ or He^+) are scattered on the surface of the sample, and the energy with which the scattered ions return to the detector is a function of the mass of the atoms, they scattered upon. The principle is illustrated in figure 3.9 and the energy relation can be expressed:

$$\frac{E}{E_0} = \left[\frac{\sqrt{M_{atom}^2 - M_{ion}^2 \sin^2(\theta)} + M_{ion}\cos(\theta)}{M_{atom} + M_{ion}} \right]^2 \tag{2.5}$$

where E_0 is the incident ion energy, E is the energy after scattering, θ is the scattering angle, M_{atom} is the mass of the atom in sample that the ion collided with, and M_{ion} is the mass of the incident ion.
Thus, the energy spectrum of the scattered ions is fully equivalent to mass spectrum of the surface. As the ions are light, the damage is to the surface is minimal. The ions are scattered almost entirely on the surface because 99% of the ions penetrating through a single atomic layer would be neutralised. However, the mass resolution is typically too low to distinguish surface elements that are closely located in the periodic system as their masses are too similar. [6],[75]

Specifics on the ISS used for this work

ISS was done in the same chamber as XPS with an Omicron ISE100 ion gun for ISS. 1keV He^+ ions were used and the scattering angle was 146.7°.

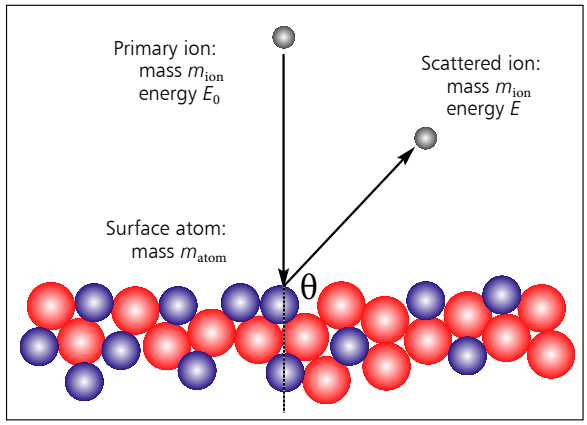

Figure 2.9: Illustration of the principle of ISS. Reprinted from [76] with minor alterations.

3

The Experimental Procedure

In this chapter, the experiments and results that provide a strong foundation for later conclusions are presented. These results include that no nickel is lost during experiments and that there is negligible influence of sulfur and show that the experimental setup is functioning well. Although not particularly interesting on their own, they are a prerequisite to interpret other results. Initially, in section 3.1, the standard experiment is described to introduce the experiment methodology, the intent of which is to prepare the reader for the discussion of the setup but equally for the results presented in the following chapters. In section 3.2 the catalyst and the experimental procedure concerning the catalyst is presented. In section 3.3 the effect the initial reduction is discussed. In section 3.4 the strength of experimental procedures is discussed and in section 3.5 the experiments related to discussion of any sulfur influence are presented.

3.1 Details on Flows and Temperature

As mentioned, the setup was built during this Ph.D. which also meant that there were no established procedures to start from. Developing good experimental procedures producing reproducible experiments was a prerequisite to any exciting measurements. The procedure of the "standard experiments" is presented in this chapter and it follows the different teachings of the first (many) experiments. Naturally there is no such thing as a standard experiment. However, many of the main findings were based on methanation conditions of 300 °C, total pressure of 3 bar, and experimental series of TPH - methanation - TPH. The schematic of such an experiment is seen in figure 3.1.

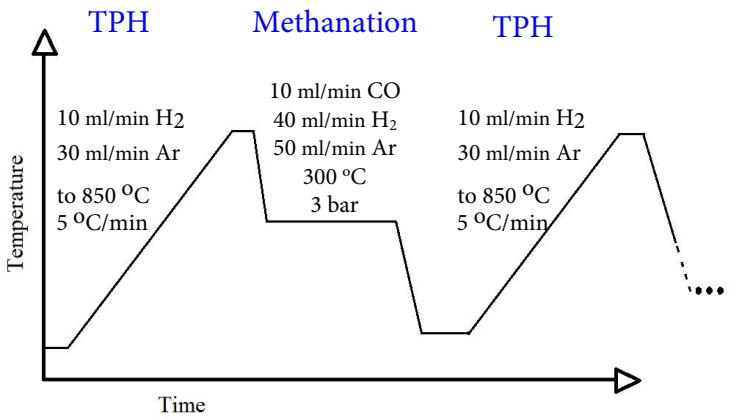

Figure 3.1: Temperature profile of a "standard" experiment.

In the chapters to come, the procedure will be described again, but the schematic in figure 3.1 is only presented here. The experiments were typically started by a TPH to reduce the catalyst. TPHs throughout this thesis (unless very specifically written) were ramping up the temperature with 5 °C/min to 850 °C at ambient pressure in 10 ml/min H_2 and 30 ml/min Ar and after having been at 850 °C for 15 minutes, cooling down in the same flow of hydrogen and argon. To initiate methanation the pressure was ramped up in steps in 40 ml/min H_2 and 60 ml/min Ar. When the temperature was stable at 300 °C and the pressure was stable at 3 bar, Ar was reduced to 50 ml/min and CO set to 10 ml/min. Thus, the methanation measurements were performed with a CO partial pressure of 0.3 bar and a CO-to-H_2 ratio of 1-to-4 at 300 °C and 3 bar. The used partial pressure of CO was so low to be sure of no nickel carbonyl formation (also at lower temperatures). As will be obvious in the following experimental results, these methanation conditions were kept for varying lengths of time. All methanation experiments were ended by relieving the pressure at 300 °C with the methanation flows to protect the roughing pump from elevated pressures. Once at near ambient pressure after roughly 20 minutes, the valves opened automatically and pumping started and the furnace was turned off to start cooling. The setup was pumped to a few mbar three times interspersed by filling with Ar to $\sim$ 800 mbar. Choice of how the methanation experiment was ended affected the subsequent TPH as seen in figure 3.2.

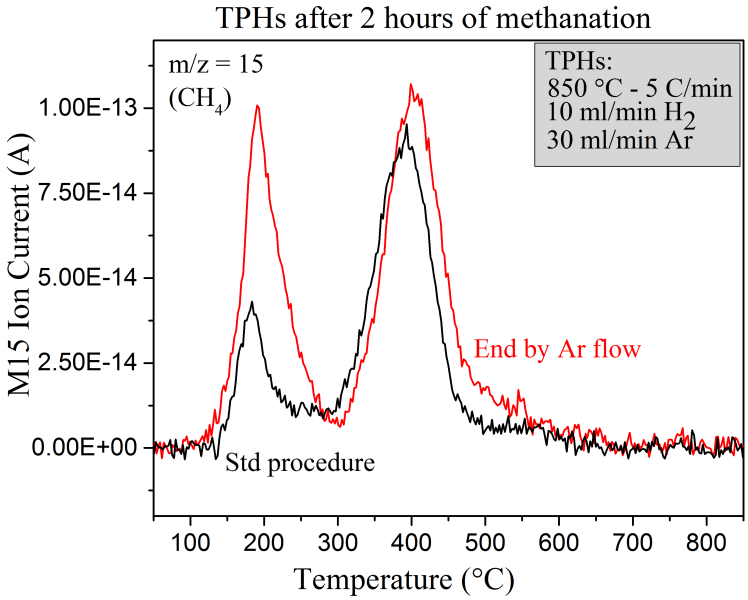

Figure 3.2: The effect of the shutdown procedure after methanation is investigated. In black the methane signal during a TPH following a 2-hour methanation experiment with the standard shutdown procedure of relieving pressure in reaction gas. The red curve is instead a TPH curve after a methanation where the pressure was relieved in a flow of Ar.

In figure 3.2 TPH following two 2-hour methanation experiments are presented. The black curve is an experiment that was ended by the standard shutdown procedure just described that was used in all subsequent experiments unless very specifically stated. As just mentioned, the methanation was ended by relieving the pressure in the reactant gas (10 ml/min CO, 40 ml/min H_2, and 50 ml/min Ar) at 300 °C and then pumping out. The methanation before the TPH measurement of the red curve was instead ended by a flow of only argon for about an hour before the setup was pumped out. It is seen that the shutdown procedure primarily affects the low temperature TPH peak at $\sim$ 200 °C. The peak is less intense and appears to be very slightly shifted. Either the argon flow contained a carbon containing impurity that increased the carbon deposition or more likely some carbon is reacted off during the standard shutdown procedure, not unlike what was also reported by Agrawal [40]. The $\sim$ 400 °C methane desorption peak could appear slightly broader with a slightly bigger feature on the left of the intense peak. However, it seems more likely that this discrepancy is a sign of the spread in this kind of experiment. As mentioned in the introduction, results reported in the literature suggest that primarily carbon desorbing at high temperature during TPHs are deactivating [41–44]. Therefore these carbon types are the more interesting and the effect of the shutdown procedure on the low temperature carbon is not of big importance. One must keep in mind though that discussing the amount

of this specific type of carbon is not particularly meaningful.
Once temperature was at $\sim$ 50 °C, the second TPH was started by stabilising the MS background levels with the relevant flows of 10 ml/min H_2 and 30 ml/min Ar and only then starting the heating to 850 °C with 5 °C/min. Experiments could end by this TPH or it could be succeeded by a second methanation to test whether the activity had been returned etc. In general experiments as just described were done by preparing a file of all the flows, temperatures etc. which was loaded into LabView in the beginning of each experiment. This meant the setup could run experiments overnight and over the weekends. In addition, it ensured that the same experiment could be repeated, as the same file was simply loaded and generally it meant procedures were similar for all experiments that were intended to be similar.

3.2 The Catalyst and Loading the Reactor

Having described the experimental procedure in section 3.1 in terms of flows and temperatures, it follows to describe the procedure in terms of the catalyst. The model catalyst was provided by Haldor Topsoe A/S. The as-prepared catalyst reportedly consisted of 22.5 $\pm$ 2.5 weight percent (wt%) nickel supported on γ-alumina. According to specifications by Haldor Topsoe A/S the total surface area was 160 m^2/g as determined by BET with a nickel surface area of 13 $\pm$ 1.3 m^2/g determined by the sulfur capacity method [77]. The pore volume was 450 ml/kg with an average pore diameter of 55 Å as characterised by Hg porosimetry and the nickel particle size was about 8 nm which had been determined by x-ray diffraction. The catalyst was pre-reduced prior to it being given to DTU. As mentioned in order to keep the conversion low the catalyst was diluted for experiments with γ-alumina inert material. Both the catalyst and alumina were crushed and sieved to sizes of 100 and 300 µm and typically 12.5 mg catalyst and 122 mg alumina were weighed off resulting in a bed height of 1.5 cm. The catalyst and additional alumina were thoroughly mixed and placed in the reactor (described in section 2.1.2) in between two plugs of quartz wool. The reactor was placed within the uniform temperature zone of the furnace, which had previously been identified. When inserting the reactor, the setup was closed off to limit the exposure to air to as small a section as possible. Once the reactor was inserted and the VRC fittings tightened, the entire setup was pumped down twice to a few mbar, filling up in Ar in between.

3.3 TPH affecting Particle Size

In section 3.2 it was mentioned that the catalyst as received reportedly had particle sizes of approximately 8 nm and was pre-reduced. However, the catalyst needed to be reduced again as the nickel particles were expected to have oxidised due to the exposure to air during transport and storage. In principle the pre-reduction meant that a fast reduction at relatively low temperature ahead of methanation would suffice but since methanation would be succeeded by TPH, reduction was done by TPH as well. This TPH ensured a clean catalyst surface. Thereby, later

there would be no adsorbates on the surface that were not a result of methanation or could be reacted off at the relevant temperatures. Thus, only molecules related to the methanation would desorb in the second TPH. In addition by performing a TPH initially, a sort of steady-state was expected as any effects of the high temperature would happen in the initial TPH.
By x-ray diffraction (XRD) the effect of the TPH-procedure was investigated as it would likely affect the crystallite size. The catalyst was reduced in the XRD setup in 25 % H_2 and 75 % He which allowed heating the catalyst and measuring XRD in situ. The catalyst was reduced at 300 °C, 700 °C, and a second treatment at 700 °C. However, as the crystallite size is affected by the thermal expansion of the crystal structure seen at elevated temperatures, the catalyst was cooled after an hour at each step to room temperature where the values presented in table 3.1 were measured. The catalyst was only treated to 700 °C instead of 850 °C because the XRD setup could not reach 850 °C in a hydrogen flow. However, 700 °C was expected to be sufficient to discuss how multiple TPHs might affect particle size although the actual values would not be the same as at 850 °C. The crystallite size was calculated using the Scherrer equation (equation 2.3 in section 2.2.1) assuming spherical particles (K = 0.9).

Treatment	hkl	Peak position	d (Å)	$d_{average}$ (Å)
300 °C	111	44.344 °	87	83
	002	51.619 °	76	
	022	76.042 °	85	
700 °C $_{1st}$	111	44.124 °	108	97
	002	51.341 °	85	
	022	75.540 °	97	
700 °C $_{2nd}$	111	44.117 °	110	97
	002	51.341 °	85	
	022	75.540 °	104	

Table 3.1: Extracted peak values based on Pseudo-Voigt fitting of XRD patterns and the nickel particle size calculated by the Scherrer equation.

Despite the variation in calculated crystallite size in table 3.1, the results showed that the first TPH increased the average crystallite size from about 8 nm to about 10 nm but a second TPH did not further increase the average size. Therefore a third, fourth etc. was equally expected to only further increase the crystallite size insignificantly. Change of particle size results in change in surface area and assuming spherical particles, the relation between specific surface area (SA), particle size (d) and density (ρ) is:

$$d = \frac{6}{SA \cdot \rho} \tag{3.1}$$

By this relation the specific surface can be estimated for the crystallites. As will be seen in chapter 5 section 5.2, TPH to 850 °C yielded a crystallite size of 11 nm (as opposed to the 10 nm found here for TPH to 700 °C). Thus, the specific surface area was calculated using 11 nm. Then the specific surface area calculated for the reported crystallite size of 8 nm for the fresh catalyst was also calculated. The ratio between these two specific areas (or directly the crystallite sizes as the other components of the equation 3.1 are the same) gave the factor of estimating, how much smaller the new nickel surface area would be. Thus, the nickel surface area was found to be 9.5 m^2/g (∼73% of the initial 13 m^2/g). Thus for all future purposes unless otherwise stated, the nickel surface area will be 9.5 m^2/g with crystallite size of 11 nm.

3.4 Strength of Measurement Procedures

Ahead of analysing experiments, the mass spectrometer data for a blank measurement is presented in figure 3.3. The experiment is blank in the sense that no catalyst had been loaded, only the diluting alumina that the catalyst was typically diluted in was loaded into the reactor by the standard procedure. The experiment was performed following all the standard procedures including pumping out the setup twice prior to starting.

In figure 3.3 the data showing the reactor first bypassed with the flows for methanation (10 ml/min CO, 40 ml/min H_2 and 50 ml/min Ar), then the setup was pumped out and filled up with Ar three times, followed by a TPH, stabilising temperature and pressure, and finally sending the methanation flow mix over the alumina is presented. Apart from a small response to starting the temperature ramp, no peaks were evident during TPH nor methanation at 3 bar and 300 °C, and since both m/z = 28 and m/z = 15 return to the same levels in bypass as through the reactor there was no activity and thus the "diluting alumina" would not contribute with CO or CH_4 desorption nor CO conversion during the experiments in itself.

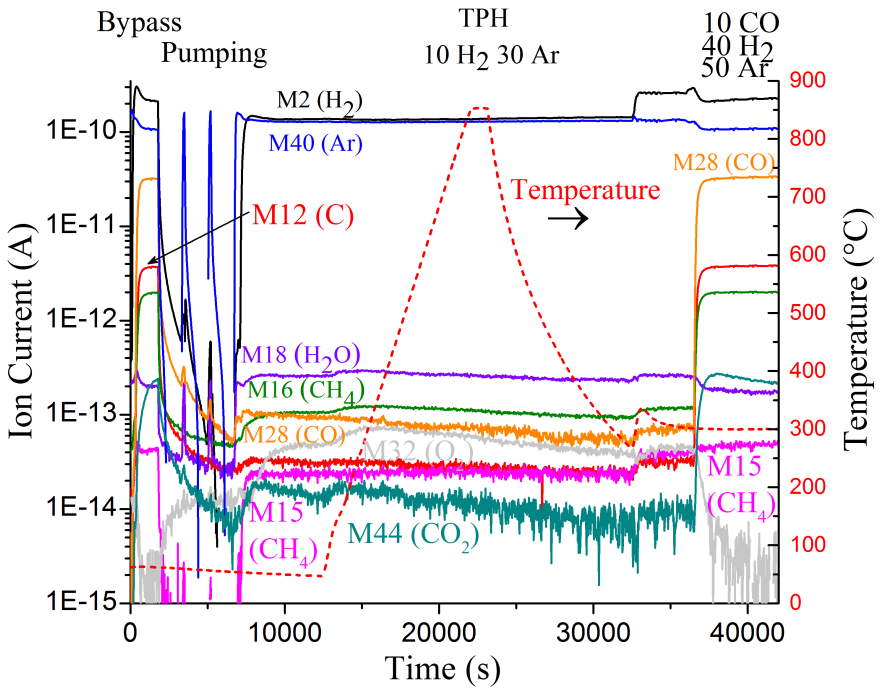

Figure 3.3: A standard experiment of bypass the reactor with methanation flows (10 ml/min CO, 40 ml/min H_2 and 50 ml/min Ar), pumping out the setup, TPH, stabilising pressure and temperature, and ending by methanation on alumina with no nickel catalyst.

Next, the reproducibility was investigated i.e. whether identical experiments yielded identical results. In the figure 3.4 the activity data for three different experiments are presented. Each experiment followed the procedure of loading catalyst, pumping out setup, bypass, pumping out setup, TPH and methanation. The methanation runs shown did not last the same period of time but this is not relevant to prove the point. All three experiments showed the same CO conversion and CH_4 %. Throughout this thesis, CO conversion will be used directly as activity. This is because the low CO conversion primarily produced the desired product: methane. In addition the relatively low conversion of <15 % in combination with the low volumetric percentage of CO in the total flow during methanation (10%) will mean a very small change in molecules from the inlet of the reactor to the outlet of the reactor. Therefore CO conversion is a good measure of the activity.

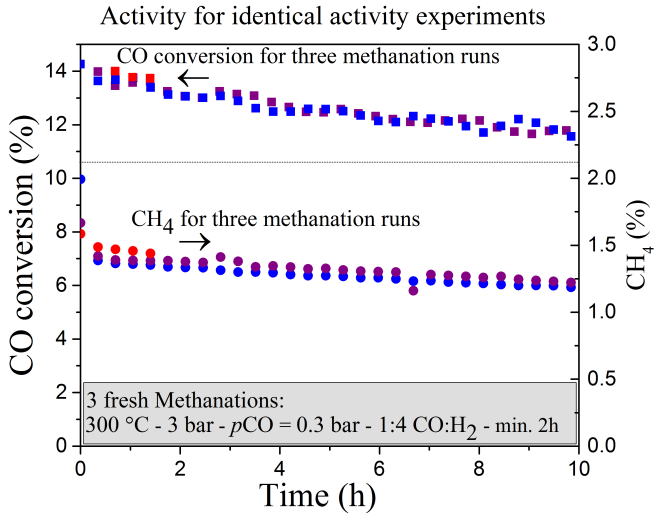

Figure 3.4: CO conversion (left y-axis, squares) and methane % (right y-axis, circles) based on GC injections for three individual methanation experiments of varying duration but otherwise identical conditions

In figure 3.5 the MS methane desorption signals from ten TPHs succeeding one hour methanation measurements are presented. It is clear that the TPH signals were very similar in temperature for the ten measurements. One was slightly shifted in temperature which could be due to an "off" temperature reading e.g. because of a poor placement of the thermocouple in the furnace. The variations in intensity may be due to the shutdown procedure but hardly no variations are seen in peak position. Thus, generally the reproducibility was very good.

In figure 3.4 it was clear that very similar activity can be reached for individual measurements despite reloading fresh catalyst each time. In figure 3.6 the methane percentage for four methanation experiments where the catalyst was reused after having been regenerated by TPH is shown. For three of the four methanation runs, the activity returned to a similar level as the initial, suggesting deactivation through carbon formation rather than sintering. Whereas for the fourth methanation, the methane level is lower which can be explained by the fourth methanation lasting much longer (24 hours), hence some small sintering is plausible. However, most of the activity was returned by the TPH which means the primary cause for deactivation was carbon deposition and not sintering.

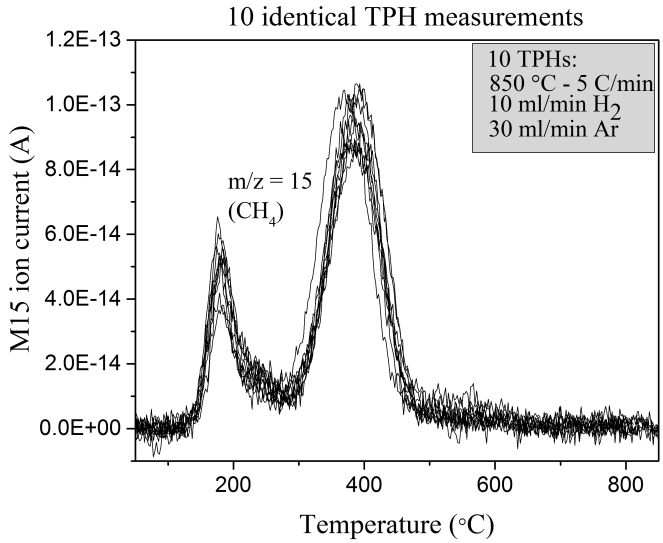

Figure 3.5: The methane signal ($m/z = 15$) during ten TPHs following ten hour methanation experiments.

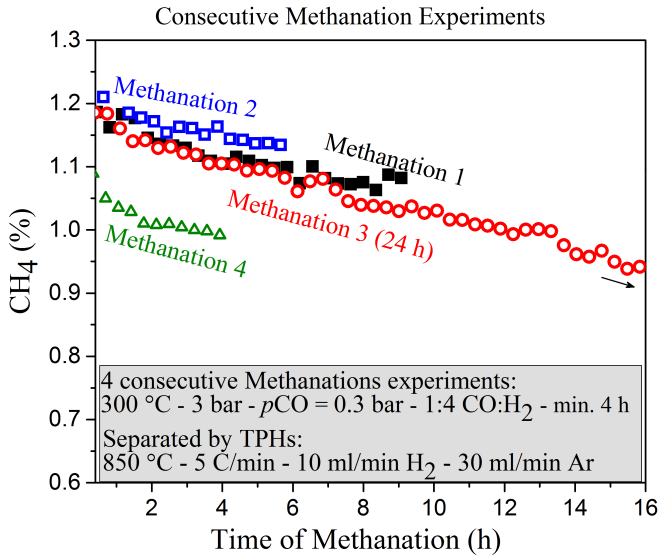

Figure 3.6: Methane % for four consecutive methanation experiments separated by TPHs.

In order to show that no nickel was lost due to nickel carbonyl formation during methanation experiments, tested catalyst samples were separated by magnet from the diluting alumina, dissolved in a mixture of 9 ml HNO_3 (65 wt%) and 3 ml HCl (37 wt%) and finally measured by ICP-MS which was done at DTU Environment.

ICP-MS is a technique for analysing soluble samples. The MS is a quadrupole mass spectrometer as described in section 2.1.3 and the inductively coupled plasma is the ionisation of the liquid analyte by bringing it in contact with an argon plasma. The results in terms of nickel concentration in the ICP-MS sample are plotted for four samples with increasing duration of methanation for increasing sample number. The spread in these results was expected to be quite high as e.g. the separation by magnet from the alumina would not be perfect. More samples having done the same procedure should have been measured to give an estimate of reproducibility and error. However, sample 1 has seen 8 hours of methanation while sample 4 has seen 150 hours and the levels are very similar so loss of nickel by nickel carbonyl formation was deemed unlikely.

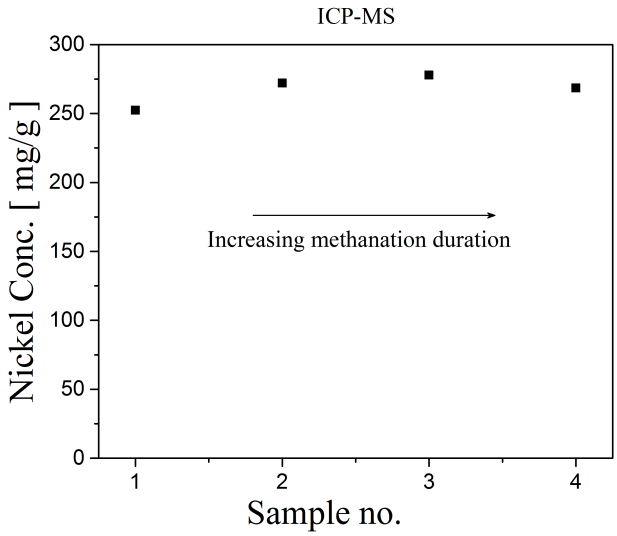

Figure 3.7: ICP-MS measurements done at DTU Environment for catalysts tested for methanation.

3.5 Presence of Sulfur?

Sulfur is an impurity that influences the catalyst and its activity e.g. in work by Gierlich et al. more carbon assigned to encapsulating carbon was observed in the presence of sulfur [35] and Wise et al. found that sulfur accelerated the formation of graphite-like carbon from carbidic carbon [64]. Engbæk et al. showed that as little as 0.03 ML sulfur was sufficient to inhibit CO dissociation on the nickel surface [52]. Since in this work focus is *not* the effect of sulfur, it is very important to eliminate any influence of sulfur.
To clean the setup after the assembly, it was heated to $\sim 80\ ^{\circ}C$ in a flow of hydrogen over a weekend and as mentioned in chapter 2 a reduced methanol $Cu/Zn/Al_2O_3$ catalyst was placed before the reactor which was expected to adsorb gas impurities

such as oxygen and sulfur. High purity gasses were used to limit impurities from the gas supply. When the setup was open to air e.g. when inserting a reactor, needle valves ensured that as small a part of the setup as possible was open to atmosphere and before further use the setup was pumped out twice.
Experiments were performed in order to test sulfur influence; reducing the catalyst by TPH, performing methanation, reacting off the deposited carbon at 550 °C and performing another methanation, hereby testing whether the activity was returned. Sulfur is immobile on nickel below 650 °C [78] and thus if the catalyst could be regenerated at 550 °C, sulfur was not the cause of deactivation. Results are presented in figure 3.8 with two four hour methanation experiments separated by a TPH to 550 °C and staying at 550 °C for six hours in figure 3.8a and in figure 3.8b two 24 hour methanation experiments separated by a TPH to 550 °C and staying at 550 °C for eight hours.

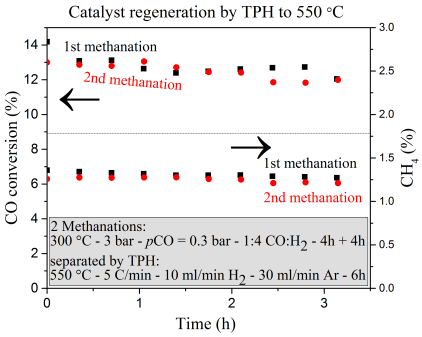

(a) CO conversion (left y-axis) and methane % (right y-axis) for methanation experiments of just under four hours, separated by TPH to 550 °C, and continued hydrogen treatment at this temperature for six hours.

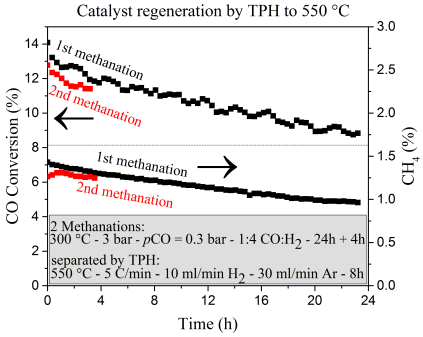

(b) CO conversion (left y-axis) and methane % (right y-axis) for methanation experiments of 24 hours, separated by TPH to 550 °C, and continued hydrogen treatment at this temperature for eight hours.

Figure 3.8: Regeneration by low temperature TPHs as check for sulfur presence.

In figure 3.8a the CO conversion and methane percentage in the exit gas for the two methanation measurements fall on top of each other, so it may be concluded that the activity is returned by the TPH to 550 °C. In figure 3.8b both the level of CO conversion and the measured methane is some 6% lower of the second methanation relative to the first. However, this could be due to some smaller sintering over the long methanation (as also seen in figure 3.6). Thus, these experiments indicate little if any sulfur but do not provide direct proof.
In the attempt to measure sulfur more directly, it attempted to measure sulfur contamination on nickel foils of about 1 cm^2. The nickel foils were cleaned in ultra-pure nitric acid and transferred to the high vacuum chamber where ion scattering spectroscopy (ISS) and x-ray photoelectron spectroscopy (XPS) was available. ISS was performed with 1 keV He^+-ions at a scattering angle of 146.7 ° on both a cleaned

and a cleaned & activity setup treated sample that had ended by TPH. As neither of these samples showed sulfur, the quantity was below the detection limit meaning less than 1 atomic percent [79]. The high temperature conditions experienced by the setup-treated sample could have pulled out impurities from the bulk of the nickel foil. If that was the case, they had been cleaned off by the TPH by which the treatment in the activity setup was ended. A clean foil placed in front of the catalyst bed experienced TPH succeeded by 60 hour methanation at 300 °C and 3 bar, and it was then transferred to the ISS and XPS chamber. In figure 3.9 selected ISS spectra for the clean foil and the methanation foil are presented.

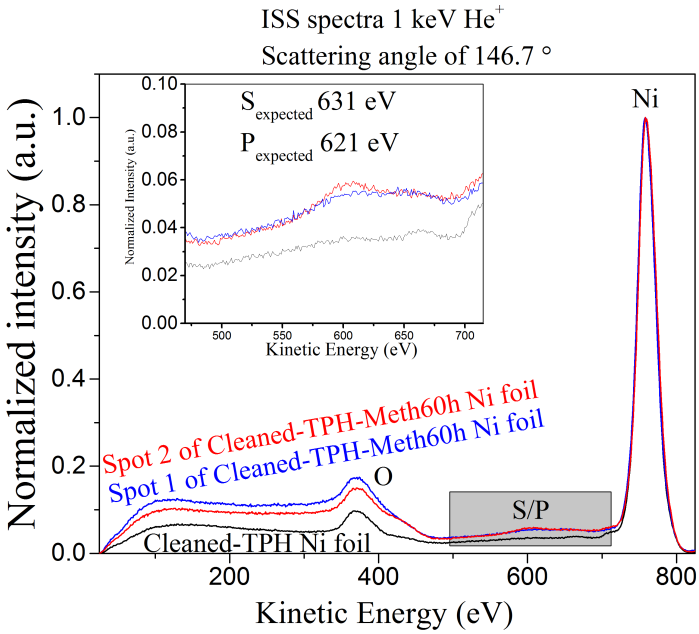

Figure 3.9: Ex-situ ISS spectra of two nickel foils of ∼1 cm^2. The black curve is a clean foil that had seen TPH-conditions. The blue and red are two different spots on the order of 0.5 µm × 0.5 µm on the same foil that had seen TPH and methanation conditions for 60 hours in the activity setup. The inset figure is the area highlighted by the grey area of 470 - 715 eV.

Nickel and oxygen, which were expected since the nickel foils had been exposed to air, are evident on both the clean foil and the methanation foil. Different areas of the methanation foil were measured aiming the beam at an area of ∼ 0.5 µm × 0.5 µm. The red and blue spectra were measured at different areas of the methanation nickel foil and the area of the red curve was by far where the highest intensity for the peak at ∼600 eV was measured. Based on equation 2.5, scattering angle of 146.7 °, and incident energy of 1 keV, sulfur was expected at maximum 631 eV and is thus a likely candidate. Phosphorus would be expected at maximum 621 eV so sulfur and phosphorus are not easily distinguishable, whereas aluminium at

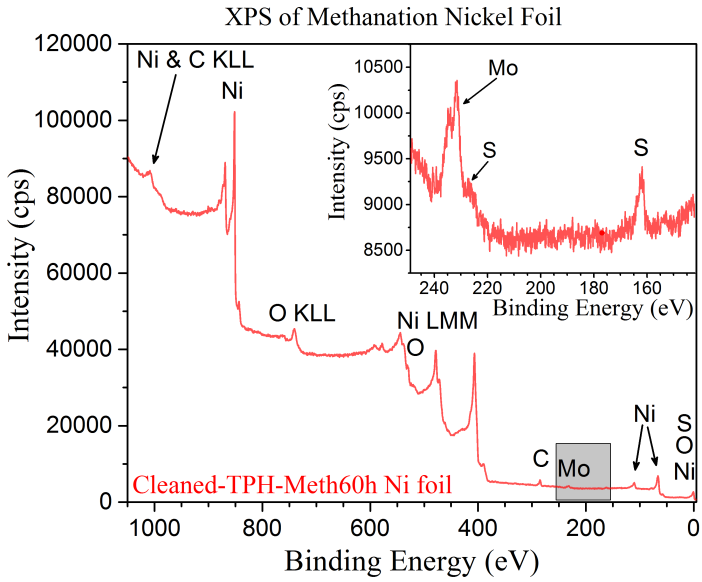

Figure 3.10: Ex-situ XPS spectrum with MgK_α radiation of the nickel foil which had seen TPH and methanation conditions for 60 hours in the activity setup. The inset is higher resolution measurements of the area of 142 - 249 eV. The observed sulfur was quantified to less than 0.1 monolayer.

578 eV and chlorine at 660 eV were rejected as the source of the peak at ∼600 eV. Decreasing the measuring spot size did not significantly change the measured ratio between the intense nickel peak at ∼770 eV and the ∼600 eV peak.
ISS is a very surface sensitive technique but XPS spectra are more readily analysed and elements quantified including determining whether the ISS peak at ∼600 eV was sulfur or phosphorus. In figure 3.10 a survey XPS spectrum and a more detailed inset are presented. Measuring carbon, oxygen and nickel is expected for a nickel foil exposed to air and compares well to the ISS spectra. Since the sample holder is made of molybdenum, it is not unreasonable to observe Mo peaks either.

Similarly to the ISS spectra small traces of sulfur is distinguishable. A rough Ni-to-S ratio analysis similar to the analysis of Alstrup et al. [80] yielded less than 10 atomic % sulfur on the surface i.e. less than 0.1 monolayer. By a saturation coverage of 0.5 monolayer [77], it is clear that the foil was not saturated and thus, it can be assumed that all available sulfur was adsorbed. Consequently, as the catalyst under investigation in the work to follow has a nickel surface area of about 1000 times that of the nickel foil, it can be concluded that if any influence of sulfur, it will be extremely small.

3.6 Conclusion on The Experimental Procedure

In this chapter it has been concluded that the influence of sulfur, if any, is negligible, the alumina used to dilute the catalyst during activity testing towards methanation is not active, identical experiments yield near-identical results, catalysts can be regenerated by TPH suggesting deactivation through carbon formation rather than sintering, and nickel carbonyl formation was unlikely. Thus, the basis for the data discussion of the following chapters has been established.

4

Activity Studies and the Cause of Deactivation

The technical foundation was presented in chapter 2 and in chapter 3 the experimental procedure was established. There was no activity without catalyst, no loss of nickel during methanation, negligible sulfur influence, and deactivation was caused by carbon rather than sintering as the activity was returned. In this chapter the data of the "standard experiments" is presented i.e. data based on methanation conditions of 300 °C, total pressure of 3 bar with partial pressure of CO of 0.3 bar and CO-to-H_2 ratio of 1-to-4. Effect of pressure, temperature, and larger nickel particles are discussed later in chapter 6.

4.1 Methanation Experiments

The experiments were all started by a TPH to reduce the catalyst which as mentioned in section 3.1 is the ramping up of temperature with 5 °C/min to 850 °C at ambient pressure in 10 ml/min H_2 and 30 ml/min Ar and after having been at 850 °C for 15 minutes, cooling down in the same flow of hydrogen and argon. As well as reducing the catalyst, the TPH also cleaned off any contaminants picked up on the shelf, which would otherwise potentially block the surface or desorb later when the catalyst was heated up, which could confuse the results. Having cooled down some hundred degrees, the flow was changed to 40 ml/min H_2 and 60 ml/min Ar in which the pressure was step-wise increased to 3 bar, and meanwhile the temperature was reaching 300 °C. Once both temperature and pressure were stable, methanation was initiated by reducing the Ar flow to 50 ml/min and setting a CO flow of 10 ml/min. By GC data, the CO conversion was calculated and along with the hydrocarbon production plotted in figure 4.1 as a function of time from a 60 hour methanation with GC injections every 21 minutes. Each experiment was started by bypassing the reactor with the methanation flow and the measured CO for this injection was used to calculate the conversion. The activity data in figure 4.1 is a random selection out of the various methanation experiments and represent all methanation experiments at 3 bar and 300 °C in the VHP setup.

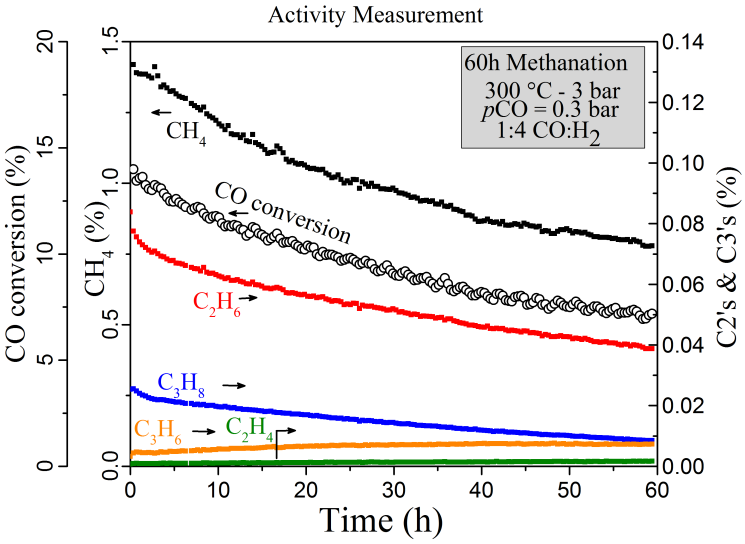

Figure 4.1: CO conversion and the main hydrocarbons in the exit gas plotted versus time during a 60 hour methanation at 3 bar and 300 °C with 1:4 ratio of CO to H_2 and partial pressure of CO = 0.3 bar.

In figure 4.1 the methane percentage in the reactor exit gas is plotted on the left y-axis whilst ethane, ethene, propane, and propene are plotted on the right y-axis, as these quantities are more than one order of magnitude lower. On the second left y-axis the CO conversion is plotted. Deactivation is clear as both CO conversion and the methane signal is decreasing over time. The alkanes (ethane and propane) decrease with similar rates whereas the alkenes (ethene and propene) increase very slightly over TOS. So as the catalyst deactivated, the balance of the partially hydrogenated hydrocarbons and fully hydrogenated hydrocarbons changed. Possibly the sites where C-C bonds are formed were less deactivated compared to hydrogenation sites. Possibly the formed carbon resulted in lower local hydrogen coverage. The results are not entirely unlike the decreased selectivity towards methane in methanation when activity is decreased due to sulfur poisoning on nickel catalysts found by Dalla Betta et al. [81]. Similar behaviour of a higher ratio of alkenes to alkanes due to carbon deactivated cobalt catalyst has also been observed by Lee et al. [82].

The methanation measurement was ended by relieving the pressure at 300 °C and immediately hereafter, the flow was stopped, the furnace turned off and the gas lines including the reactor were pumped out three consecutive times separated by filling up in Ar to about 800 mbar. When the temperature at the catalyst bed was lower than 100 °C, the TPH flow (10 ml/min H_2 and 30 ml/min Ar) was set and kept for one and a half hours in order to stabilise the background levels of the mass spectrometer. Then the temperature was ramped up with 5 °C/min to 850

°C from by now significantly lower than 100 °C. The carbon built up on the catalyst surface was hereby reacted off by hydrogen and both GC and MS confirmed that only methane was formed. The results of TPHs following methanation measurements of various duration is presented in figure 4.2. The MS methane signal (m/z=15) measured every 26 seconds is plotted as a function of the temperature at which it was detected, and a constant linear background level has been subtracted for each curve. All MS data on methane was based on m/z = 15 because although m/z = 16 has the highest intensity for methane, m/z = 16 is also affected by the water signal due to the fragmentation of molecules mentioned in section 2.1.3 on mass spectrometry. Since there was no ammonia, m/z = 15 was purely a methane response and as m/z = 15 is 85% of the intensity of m/z = 16, it was sufficiently intense [69].

McCarty and Wise discussed surface carbon based on its reactivity towards hydrogen [39]. In this light, it is clear three types of carbon are evident from figure 4.2 as there are three distinct peaks; ∼200 °C, ∼400 °C, and ∼500 °C. The amount of 200 °C TPH peak carbon was highly sensitive to the shutdown procedure after methanation and amounts were reduced by the chosen procedure where pressure was relieved in the methanation flows as opposed to a procedure that included a flushing with Ar. In contrast, it was found that the 400 °C and 500 °C TPH peaks were not affected by the shutdown procedure. The large variation in amounts of the 200 °C TPH peak carbon in figure 4.2 is likely due to the effect of the shutdown procedure. It seems that the two higher temperature peaks are related to each other. TPHs succeeding short methanation experiments (less than two hours) have no or virtually no 500 °C TPH peak, while in the TPH curves after the longest methanation experiments the 400 °C TPH peak appears visually more like a shoulder on the 500 °C TPH peak rather than a separate 400 °C TPH peak. The 8 hour and 24 hour curves have both peaks distinctly.

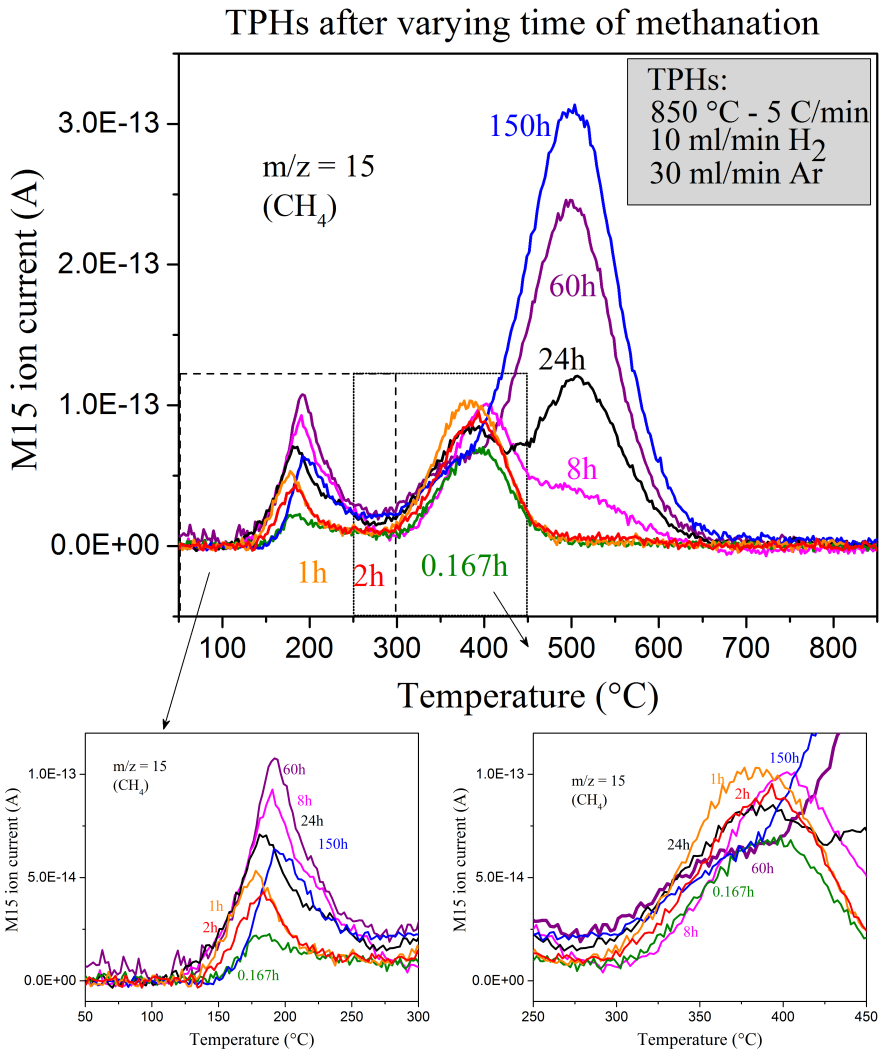

Figure 4.2: Methane signal ($m/z = 15$) during TPH subsequent methanation of various duration as a function of temperature. Flow of 10 ml/min H_2 and 30 ml/min Ar and ramping with 5 °C/min. An individually determined constant background level has been subtracted from each graph.

Integrating the methane signal as a function of time yields the total amount of carbon reacted off in the TPH, making a comparison between the different TPH curves and amount of carbon deposited during methanation easier. Based on the MS signal of a known methane quantity, the temperature and the total flow of TPH, the integrated area may be converted to a number of methane molecules. The nickel surface was estimated by the total Ni surface area per gram of catalyst (adjusting for larger particles than fresh catalyst as explained in chapter 3) times the weight

of catalyst times the Ni sites/atoms per area when assuming only Ni(111) surface planes:

$$\mathrm{Ni} = \mathrm{SA_{Ni}} \cdot \mathrm{w_{cat}} \cdot \frac{1}{\frac{\sqrt{3}}{2}\mathrm{d_{NN}^2}} = 9.5 \cdot 0.0125 \cdot \frac{1}{\frac{\sqrt{3}}{2}(2.49 \times 10^{-10})^2} \tag{4.1}$$

where $\mathrm{SA_{Ni}}$ is the nickel surface area of the catalyst per gram catalyst, $\mathrm{w_{cat}}$ is weight of catalyst in the experiment and $\mathrm{d_{NN}}$ is distance between nickel atoms. Dividing the result ("Ni") which is the number of atoms or an estimation of sites by Avogadro's number, yields the nickel surface atoms in the experiment in moles and can thus be related to methane molecules reacted off in TPH to yield the ratio of carbon atoms to the nickel surface atoms; $\mathrm{C/Ni_{surf}}$. In this way the carbon-to-nickel ratio resulting from methanation may be estimated for each experiment in figure 4.2. The result has been plotted in figure 4.3, colour-coded to match the respective curves in figure 4.2.

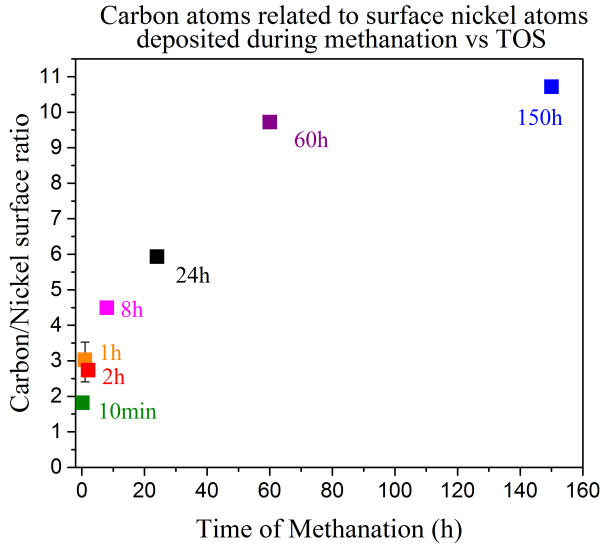

Figure 4.3: The total deposited carbon-to-nickel surface ratio as a function of time on stream.

Not surprisingly, it may be observed that the longer the methanation, the more carbon was reacted off during the subsequent TPH. It seems that carbon is built up on the surface immediately and rather fast which was also clear from the short methanation experiments in figure 4.2 where even after 10 minutes of methanation a significant methane desorption was evident. However, the carbon deposition slowed down after a while as the trend in figure 4.3 is levelling out. A total ratio of 11 carbon atoms to the nickel surface atoms is a relatively large number since it is equivalent to an average of more than five graphene layers as a graphene overlayer on the nickel 111 surface, Ni(111), has a ratio of 2C/Ni [54].

4.2 Carbon and Deactivation

Thus far, it has been established that the catalyst deactivated during methanation due to carbon formation and that carbon was increasingly deposited on the catalyst. So it follows to combine these results.
The activity for each GC injection is defined as the CO conversion as mentioned above and therefore the activity loss in percentage over the duration of the methanation is defined as:

$$\text{Act Loss}[\%] = \frac{\text{Act}_{\text{ini}} - \text{Act}_{\text{end}}}{\text{Act}_{\text{ini}}} \times 100 \tag{4.2}$$

where Act_{ini} is initial conversion once relatively stable (in practice the data of the second GC injection), Act_{end} is the CO conversion at the end (i.e. the data point of the last GC injection), and Act Loss [%] is activity loss in percent.
By analysing from the 2nd injection the exact timing of starting the GC measurement versus when the methanation flows are introduced is not as crucial as it would have been if the initial activity was the focus. Dalla Betta el al. [81] also split up activity data in "initial" (the first 1000 seconds) and "steady state". Here the 2nd GC injection means that the starting point is at least 20 minutes into the methanation. Thus some carbon has already been formed which is neglected meaning that zero is not truly zero. However, this shift in "zero" is expected to be the same for all measurements thus only a constant shift on the x-axis for all points.
The $\text{C/Ni}_{\text{surf}}$ is plotted against the activity loss during the respective methanation experiments in figure 4.4. As well as plotting the results from the figure 4.2 and 4.3 (still as full squares), data from similar experiments have been added as follows:

- The error on x-axis of the 1 hour point was defined as 2 × the standard deviation of the $\text{C/Ni}_{\text{surf}}$ from the ten identical experiments in figure 3.5 in chapter 3 and activity data error is the 2 × the standard deviation of 4 points: the 1 hour activity loss in 2, 24, 60 and 150 hour methanation experiments.
- Activity and carbon data for two 2 hour experiments have been plotted (the full square is for the curve in figure 4.2) and the error which is the same for

both is two times the standard deviation of activity loss of those two and the activity loss after two hours for the 60- and 150 hours methanation.

- The eight hour data point has the error defined as two times the standard deviation based on activity loss during the 8, 24, 60 and 150 methanation experiments.
- The 24 hour error is two times the standard deviation based on only **three** measurements: 24, 60 and 150 methanation experiments.
- Data from two 60 hours methanation have been plotted.
- The 150 hour activity point is an extrapolation based on activity loss during 105 hours as GC malfunctioned (MS confirmed range).

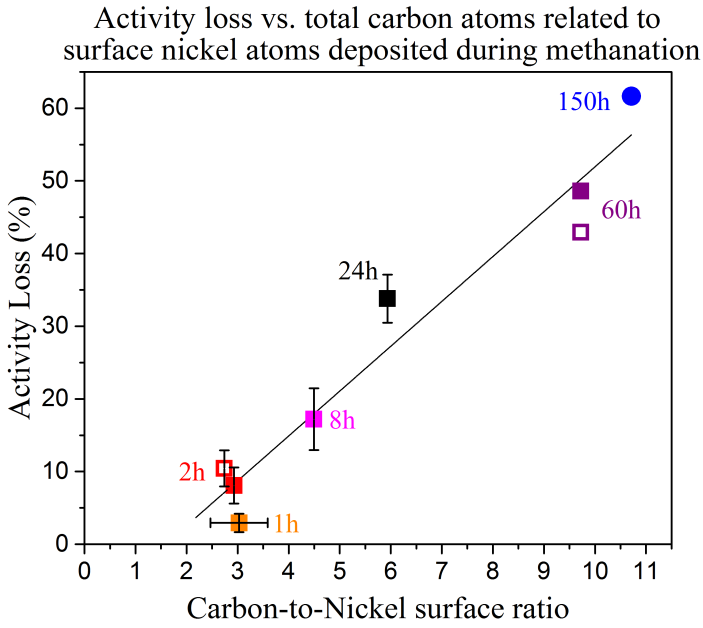

Figure 4.4: The total deposited carbon-to-nickel surface ratio as a function of the activity loss during the methanation experiments.

Summarising, the error on the activity is generally two times the standard deviation of four data points, full squares are results from experiments in figures 4.2 and 4.3, and the error on C/Ni_{surf} is calculated from the ten identical one hour experiments in figure 3.5. Care must be exercised when analysing the error bars since the same measurements have been used multiple times and if one measurements was "off", it is expected to be "off" also earlier or later in the measurement. On the other hand, there is no reason why a 24 hour methanation experiment could not just as well tell the activity loss for an eight hour methanation experiment. No 0.167 hours (10 minutes) data was added as the interval between GC injections lasted 21 minutes. Data could have been provided by the MS but as all other

activity had been based on GC data and as 10 minutes was too short for a reliable "steady state" deactivation measurement, the point was omitted.

It reasons, that the activity loss during methanation and carbon deposited on the surface during this methanation are directly related. An increased carbon deposition resulting in larger deactivation with longer time on stream is expected [42]. However, to the best of our knowledge no results have been reported that showed the correlation to be linear for methanation on nickel.
It is seen in figure 4.4 that as large a coverage as almost eleven carbons to a nickel surface atom (equivalent to an average of five graphene layers as mentioned) was not sufficient to completely deactivate the catalyst, as almost half the activity during methanation was left even at this coverage. As discussed in the introduction, from literature it is clear that the active sites for methanation; the nickel steps could equally be the nucleation sites for graphite formation. As almost 50% of the activity remains despite these large amounts of carbon that have been deposited, all active sites have not been covered. This points to a carbon growth that may nucleate on the Ni step sites but that grows away from these and is not selectively covering the steps. Thus, results already tentatively point towards patchy (cyclo)polymeric carbon as has been suggested to cause deactivation on Co during FTS [63].

4.3 Fitting of the TPH Peaks

In order to discuss the different peaks, each curve in figure 4.2 was analysed by a Gaussian multiple peak fit in the software OriginPro 2015 by applying the function "Gauss" as a first order approximation. Due to the non-perfect Gaussian shape of the 200 °C peak, this was fitted as two peaks. No constraints were necessary to achieve similar fits with four peaks for all graphs and in general the fits matched the curves very well.

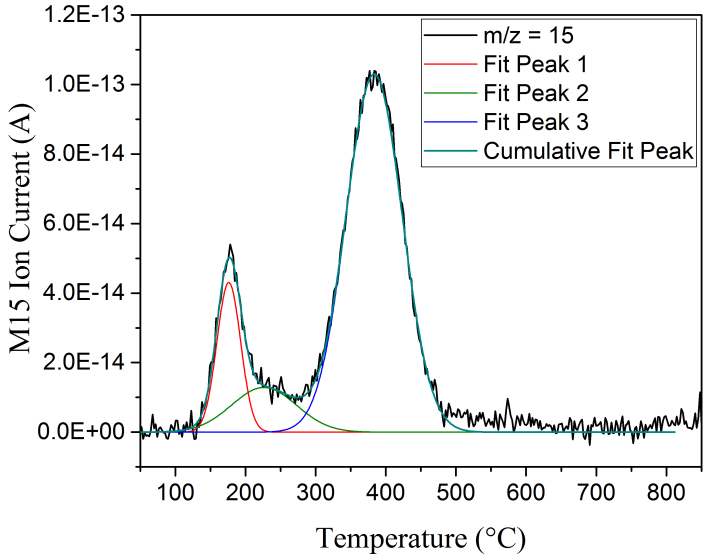

(a) The multiple Gaussian peak fit for one hour curve (the red curve) in figure 4.2 is presented. The raw data with the background level subtracted is a solid black line, the four peaks are plotted in different colours and the resulting fit is plotted in dark cyan.

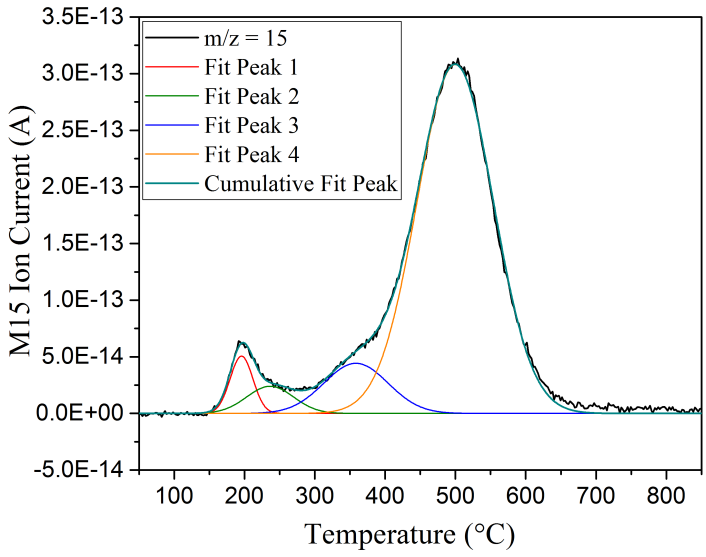

(b) The multiple Gaussian peak fit for 150 hour curve (the blue curve) in figure 4.2 is presented. The raw data with the background level subtracted is a solid black line, the four peaks are plotted in different colours and the resulting fit is plotted in dark cyan

Figure 4.5: Examples of how the curves in figure 4.2 were analysed by multiple Gaussian peak fits with the OriginPro "Gauss" function.

In figure 4.5 the Gaussian fit result is presented for the one hour methanation (figure 4.5a) and the 150 hour methanation (figure 4.5b).
From figure 4.2 the peak positions seemed essentially fixed so naturally the peak fit centres should be equally fixed as well, so these are plotted against the methanation duration in figure 4.6a. Thus, vertically the four peaks for each methanation experiment are plotted and horizontally the peak maxima of the four peaks are plotted as a function of methanation duration. It is clear that the centres of the Gaussian peaks generally are reasonably stable (horizontal straight lines) as was also expected based on the results in figure 4.2. For peak 1 (∼185 °C) and peak 2 (∼215 °C) short methanation experiments yield slightly lower peak temperatures compared to longer methanations which was already clear in figure 4.2. The 400 °C TPH peak shifts down in temperature (roughly 30 °C) with increasing duration of methanation experiments. So as the 500 °C TPH peak grows, the 400 °C not only decreases in intensity in figure 4.2, the peak maximum also shifts. For the short methanation run (2 hours), the ∼500 °C peak is very high in temperature but as there is very little of this TPH peak, this variation is likely due to a low signal-to-noise ratio and thus a high uncertainty in the position of the peak maximum. In figure 4.6b the FWHM of each peak fit based on time is plotted. As each TPH are identically ramped, they can be readily compared to each other. The FWHM of peaks 185 °C and 500 °C are very stable while the FWHM of peak fit 215 °C and 400 °C seem to react oppositely to increasing duration of methanation; 215 °C peak FWHM decreases whilst 400 °C FWHM increases.

Since four peaks of carbon have been identified and the deactivation during methanation was linearly related to the amount of carbon, it follows to examine whether all carbon types are equally deactivating. In addition by gaining insight into the relation of the various TPH peak carbon species to the methanation activity, it may be possible to establish that since the shutdown procedure primarily affected the low temperature carbon, it is of minimal concern.

Thus, in figure 4.7 peak fit areas have been converted to C/Ni_{surf} in the same fashion as mentioned earlier in this chapter and plotted as a function of methanation duration. In addition, the activity loss of the 150 hour methanation as a function of time is also plotted on the right y-axis.
It is immediately apparent in figure 4.7, that only the TPH peak intensity of 500 °C increased significantly with TOS while the 400 °C TPH peak decreased with TOS, supporting the interdependence discussed earlier. The shape of the activity loss curve and 500 °C TPH peak carbon atoms to nickel surface atoms ratio are remarkably similar, which is a strong indication of a close relation.
In figure 4.8 activity loss of the methanation experiments was plotted as a function of the carbon-to-nickel surface ratio of the 500 °C peak fit. It is obvious that the activity loss during methanation is linearly related to the quantity of the carbon species related to the 500 °C TPH peak. Thus, not only is the relation of the activity loss and total carbon as plotted in figure 4.4 linear but the 500 °C species give rise to this correlation and must give rise to the long term deactivation.

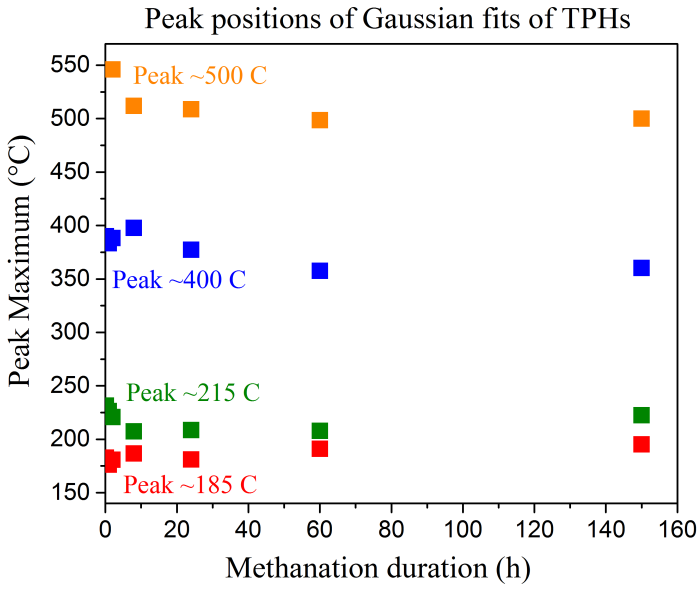

(a) The centres for the four peaks involved in the Gaussian multiple peak fits of the TPH curves of figure 4.2.

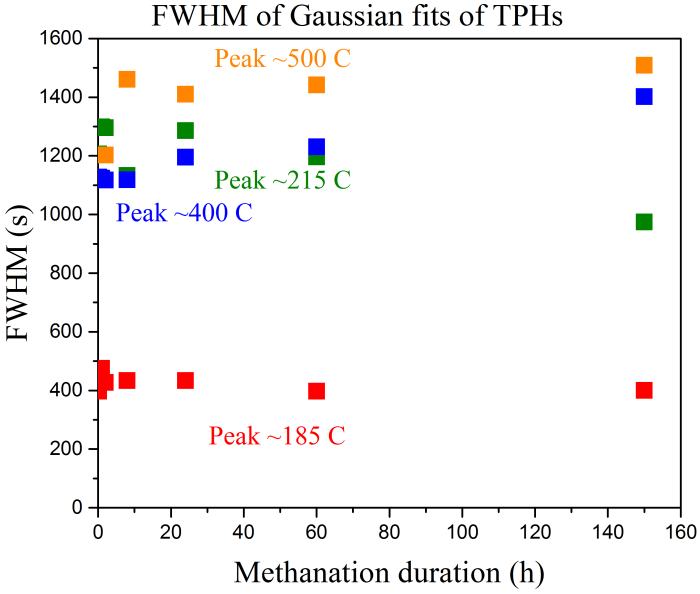

(b) The FWHM based on time under the Gaussian peaks used to fit the TPHs results in figure 4.2.

Figure 4.6: Analysis of the Gaussian peak fits by the peak maxima and FWHM for the TPHs in figure 4.2.

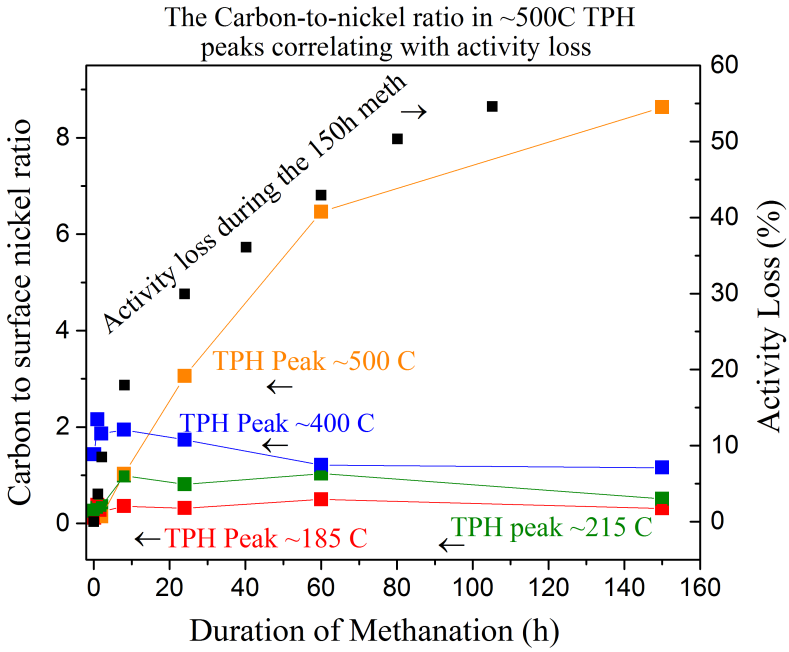

Figure 4.7: The carbon-to-nickel surface ratio for the TPH peaks as well as the activity loss during the 150 hour methanation experiment.

The linear regression does not go through origo. However, this behaviour in combination with the interdependence observed earlier for the 400 °C TPH peak and the 500 °C TPH peak suggest that the 400 °C TPH carbon species were also deactivating. It seems, the two carbon species were similar in structure and location on the nickel surface, and the 400 °C TPH peak carbon was likely a precursor for the species of the 500 °TPH peak. Considering the reported growth mechanisms of carbon species [55,63], the 400 °C TPH peak carbon acting as a precursor for the 500 °C TPH peak carbon is likely.

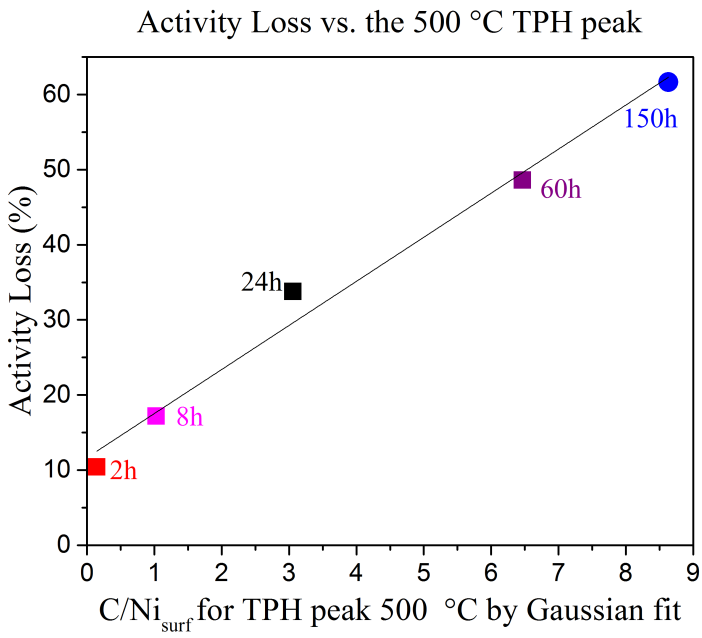

Figure 4.8: The area under the 500 °C peak (Gaussian peak 4) versus the activity loss during methanation with the colour-coding from figure 4.2.

4.4 Conclusion on Activity Measurements

In this chapter it has been established through thorough analysis of the TPH curves succeeding methanation, that the seemingly three types of carbon deposited during methanation at 300 °C and 3 bar, could be four types as a good Gaussian fit is achieved by four peaks. The two high temperature TPH peaks (400 °C and 500 °C) are interdependent and the main cause of long-term deactivation is the 500 °C TPH peak. In chapter 5 these carbon types are discussed and characterised and in chapter 6 the effect of temperature, pressure, and particle size on deactivation and carbon types are investigated.

5 Analysis of the Carbon Species

Previously in chapter 4 deactivation during methanation at 300 °C and 3 bar was studied and correlated to the amount of carbon removed after the methanation by TPH. It was observed that multiple types of carbon species were involved but that primarily species reacted off during TPH at 500 °C were deactivating after extended methanation times. The 400 °C and 500 °C TPH peak carbon types seemed interdependent and likely the 400 °C was also deactivating. The 200 °C feature needed to be fitted by two peaks implying two carbon species. In this chapter the data, to elucidate what these carbon species are, is presented and discussed. It includes CO or CH_4 surface probing measurements, XRD, STEM with EDS, and Ar TPDs succeeding the methanation measurements.

5.1 Surface Probing Measurements

To gain insight into the amount of carbon and possibly especially the carbon of the low temperature (∼200 °C) TPH peak from the TPH's succeeding methanation in figure 4.2, it was attempted to produce a monolayer of carbide on the catalyst. The intention was that by forming a carbide layer and reacting it off with hydrogen in similar fashion as done after methanation measurements, it would elucidate whether the low temperature species in methanation TPHs in figure 4.2 were carbidic. Inspired by work of I. Alstrup [83] and C. Klink et al. [84], the nickel surface was exposed to methane or carbon monoxide at 226 °C (500 K) and ambient pressure to form a saturation layer of carbidic carbon. As in the surface science approach, the idea was to expose the catalyst to just sufficient amounts to create the saturated surface layer of Ni_2C-structure equivalent to 0.45 ML carbon on Ni(111) [84]. Different concentrations and durations of the exposure were tested. Most of the adsorption measurements were done with methane but it was clear that essentially the same results were produced if the measurements were performed with carbon monoxide.

As in chapter 4 the diluted catalyst was reduced by a TPH. But in order to minimise any residual hydrogen adsorbing on the surface during the cooling down after the TPH, the procedure was changed so that the setup was pumped out immediately after having been at 850 °C for 15 minutes. The lines were pumped out three times interspersed by a flow of argon. As the temperature at the catalyst bed approached the adsorption experiment temperature of 226 °C, a stable flow of Ar of 95 ml/min was set. Once the temperature and MS signals were stable, the flow of Ar was adjusted and either the appropriate flow of CO or CH_4 was started to achieve a total flow of 100 ml/min. The measurements were ended by terminating the CO or CH_4 flow but continuing the Ar flow for another ten minutes at 226 °C. This was done to minimise loss of carbon as seen in figure 3.2 and thus achieve a saturation layer. Thereafter the setup was pumped out and cooled down analogously to the previous procedure for methanation. Once the temperature had decreased to about 50 °C, a TPH was initiated. The methane desorption during the TPHs are presented for experiments with both 5 % and 100 % methane and for 10 minutes, 2 hours, and 10 hours in figure 5.1. Despite the change of format/figure appearance of figure 5.1, it is not different from previous TPH graphs except the curves are separated on the z-axis to better expose the features without them overlapping. The carbon being reacted off after the methane exposure generated two features for all TPH curves, as seen in figure 5.1. The main desorption peak at ∼200 °C and a broad feature at ∼425 °C. These peak temperatures match the results found by McCarty and Wise who assigned carbon reacted off by TPH below 600 K (327 °C) to carbide and carbon above to polymeric carbon [39]. In accordance with their conclusions, it appears the curves in figure 5.1 show evidence of the surface carbide layer that was expected and a smaller amount of polymerised carbon. Two and ten hours of 5% methane exposure (the red and blue curve) yield very similar results whereas ten minutes of neither five percent nor 100 % (green curve in the front and dark cyan curve at the back) seem sufficient to reach a similar level. Thus, ten minutes were deemed insufficient time to create a full saturation layer of carbide. Two and ten hours of 100 % methane (pink and dark cyan curves) are shifted to higher TPH peak temperature as compared to the other results.

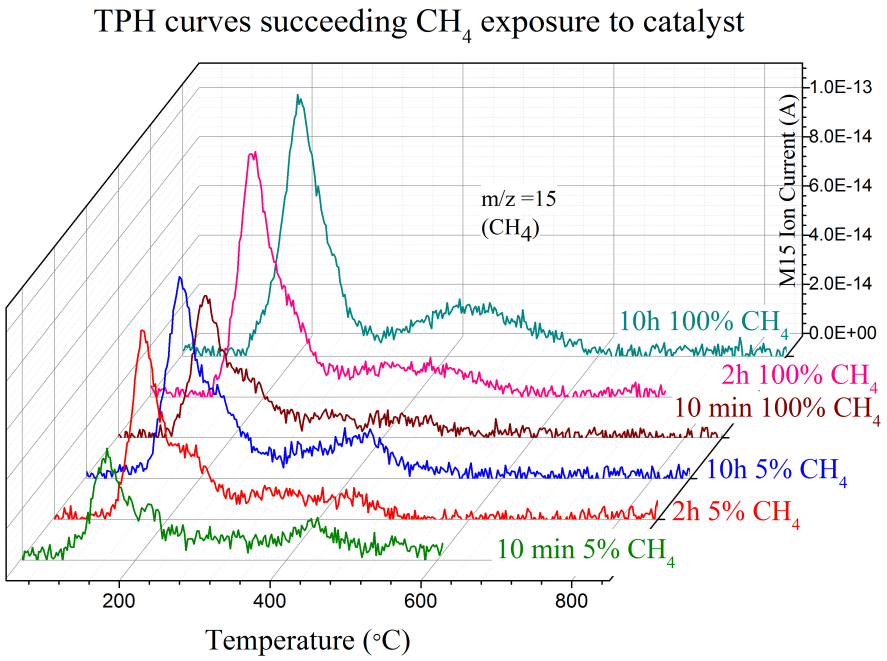

Figure 5.1: TPH curves with 10 ml/min H_2 and 30 ml/min Ar ramped up to 850 °C by 5 °C/min succeeding CH_4 adsorption measurements at 226 °C and ambient pressure with total flow of 100 ml/min with 5% or 100 % CH_4 adjusted by Ar.

Similar to the results by Gauss fitting of TPH curves after methanation (figure 4.2 and 4.5), the 200 °C desorption peak was likely two peaks. Therefore, the shift to higher temperature for the two and ten hours of 100 % methane may originate from different hydrogenation kinetics due to some dependence on either the larger amounts of the second peak or larger amounts of the 425 °C feature. As mentioned, adsorption of CO was also tested and in figure 5.2 the methane desorption during TPH after two hour 5 % CO in Ar is presented along with the two hour 5 % CH_4 from figure 5.1 i.e. the red curve.

As expected, the agreement between the main adsorption peak at ∼200 °C of 5% CO and 5% CH_4 is very good; peak maximum is at the same temperature and the shape is much alike, but the CO is moderately higher (7% larger peak area), possibly suggesting slightly less than a complete monolayer for the 5% methane experiment. In order to confirm the formation of the carbide saturation layer, the TPH curves based on time were fitted by a Gaussian multiple peak fit in OriginPro 2015 using the "Gauss" function as before in chapter 4 figure 4.5. Similarly to the curves in figure 4.2, the main peak was fitted by two Gaussian peaks and the calculated values for the ratio of carbon to surface nickel for these are presented in table 5.1 along with peak temperature and FWHM in temperature. All fits were

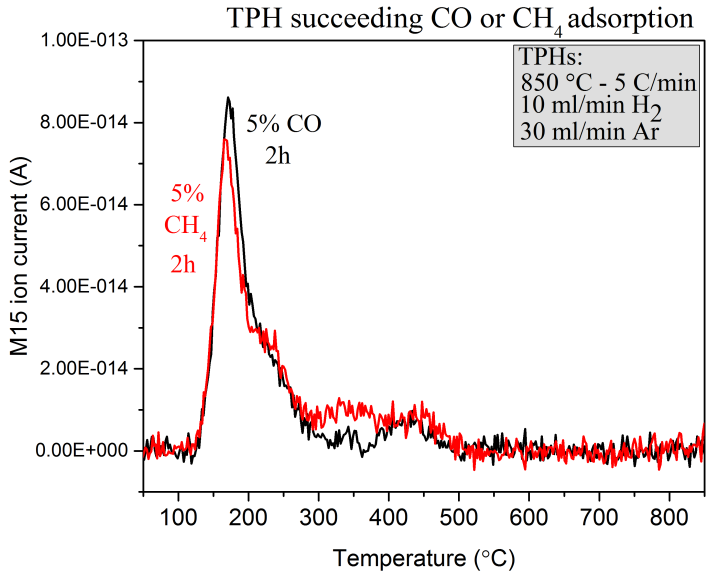

Figure 5.2: TPH curves with 10 ml/min H_2 and 30 ml/min Ar ramped up to 850 °C by 5 °C/min succeeding CO or CH_4 adsorption measurements at 226 °C and ambient pressure with total flow of 100 ml/min with 5% CO or CH_4 adjusted by Ar.

performed without constraints on the fitting parameters for the various curves to limit influencing the results. However, if a fit stood out e.g. in FWHM, it was attempted if an equally good fit could be achieved with a small tweak of that peak.

The ten minute results are outliers compared to the five other measurements. These results simply imply that 10 minutes is not sufficiently long to achieve a monolayer, as already established. This is not unreasonable and the intensity gain in figure 5.1 by extending the exposure to two hours, indicates the same conclusion.

5% CH4		**10 min**	**2 h**	**10 h**
Peak 1	Xc (°C)	163	167	172
	FWHM (°C)	34	34	37
	C/Ni_{surf}	0.24	0.41	0.43
Peak 2	Xc (°C)	195	213	213
	FWHM (°C)	115	39	85
	C/Ni_{surf}	0.47	0.52	0.56
100% CH4		**10 min**	**2 h**	**10 h**
Peak 1	Xc	163	182	203
	FWHM	30	36	34
	C/Ni_{surf}	0.29	0.45	0.45
Peak 2	Xc	203	211	216
	FWHM	73	83	88
	C/Ni_{surf}	0.47	0.74	0.91
5% CO			**2 h**	
Peak 1	Xc		171	
	FWHM		37	
	C/Ni_{surf}		0.49	
Peak 2	Xc		214	
	FWHM		90	
	C/Ni_{surf}		0.50	

Table 5.1: The results of fitting the main carbon desorption peak after exposure to 5%, or 100 % CH_4 or 5% CO. For each peak the peak maximum, X_C, the peak full width half maximum (FWHM) in temperature, and calculated carbon-to-nickel surface ratio, C/Ni_{surf}, are listed. The TPH curves were fitted by three peaks performing Gaussian multiple peak fit in OriginPro 2015 by the "Gauss" function.

Based on the remaining five fits, it can be concluded that independent of time and active gas, a quite sharp (FWHM $\sim$ 35 °C) carbon feature at 180 $\pm$ 20 °C of 0.41-0.49 C/Ni_{surf} is formed associated with a saturation layer of surface carbide. This is in excellent agreement with the expected 0.45 ML carbon on Ni(111) [84]. However, also a second feature is formed at roughly 205 $\pm$ 10 °C which is not as constant in amount; the carbon to surface nickel atom ratio increases with greater amount and time of exposure from $\sim$0.5 to $\sim$ 0.9.
The results resemble the findings from earlier in chapter 4 where the low temperature peak also needed to be fitted with two Gaussian peaks; one with peak maximum at $\sim$185 °C and at $\sim$ 215 °C. McCarty et al. also found as well as forming a surface carbide also a second type of carbon was formed which they assigned to bulk carbide [39]. The nature of two TPH fit peaks within the asymmetric peak around 200 °C is investigated further by XRD in section 5.2.

5.2 Carbon Studied by X-Ray Diffraction

X-ray diffraction (XRD) is as discussed previously in section 2.2.1 a non-surface and an average characterisation technique, so it was not expected to observe the monolayer of surface carbide. However, both bulk carbide and carbon dissolved into the nickel may be detected. A rule of thumb says that mixed phases may be measured if each phase is at least roughly 2% of the sample [85] i.e. the nickel carbide phase must make up around 2% of the nickel phases. On the other hand, had carbon dissolved into the nickel particles, it was expected that the nickel lattice constant would be larger than that of reduced nickel and thus, equally measurable. As mentioned, McCarty et al. suggested based on the two low temperature TPH peak findings near 200 °C that as well as forming carbidic surface carbon also bulk carbide was formed. On the contrary, multiple groups have claimed to detect dissolved or interstitially bound carbon in nickel [86–89] as opposed to bulk carbide. Thus, we wanted to investigate whether the second type of carbon species was carbon dissolved into the nickel or bulk nickel carbide. However, for XRD to finalise this discussion, the second TPH peak carbon must amount to at least 2% of the sample. If not, it is still possible to measure an expanded nickel crystal, the sign of dissolved carbon, but not bulk carbide and thus it is hard to completely reject any possibility of bulk carbide being present.
Consequently the 0.52 C/Ni_{surf} for the second peak of 5% CH_4 for 2 hours and the 0.50 C/Ni_{surf} or the second peak of 5% CO for 2 hours must be converted into a ratio of carbon-to-all-nickel not carbon-to-surface-nickel. This requires the number of carbon atoms and the total number of nickel atoms. The carbon atoms were calculated simply by multiplying 0.5 with the number of nickel surface atoms calculated in chapter 4 equation 4.1. The total nickel atoms were calculated by the weight of catalyst (w_{cat}) times the weight percentage of nickel in the catalyst (Ni/cat) times Avogadro's number divided by the molar weight (M_{Ni}). Subsequently it was straight forward to find the ratio of carbon to nickel and convert into percentage.

$$\begin{aligned} \text{Carbon atoms} &= 0.5 \times 2.563 \cdot 10^{18} = 1.282 \cdot 10^{18} \\ \text{Nickel atoms} &= \frac{w_{cat} \times Ni_{cat} \times 6.022 \cdot 10^{23}}{M_{Ni}} = 2.821 \cdot 10^{19} \\ \text{Carbon-to-nickel\%} &= 4.5\% \end{aligned} \tag{5.1}$$

So the carbon under investigation amounts to roughly 4.5 % of the nickel on an atom basis but since nickel is no more than 25 wt% ($\sim$ 10 at%) of the catalyst, 4.5 % of carbon is not sufficient to fulfil the 2% requirement. Therefore analysing the XRD patterns and not measuring bulk carbide is not proof that this phase does not exist in small domains. However, an increased lattice parameter will justify suggesting dissolved carbon as this will still be a distinct fingerprint of a slightly bigger crystal lattice rather than a new crystal structure. Combining the two equations (2.1) and (2.2), it is clear that an increased lattice constant (a) will result in a shift in peak position (θ), theoretically enabling measuring dissolved carbon.

The XRD measurements were done ex-situ i.e. samples were prepared in the activity setup and transferred to the XRD setup at ambient conditions. Each sample was extracted from the reactor by a push/flow of Ar and separated from the "diluting alumina" by a magnet, as the nickel catalyst is magnetic and the alumina is not. Only the catalyst part was measured in the XRD by placing the powder in the middle of a silicon zero background plate, which gives no distinct peaks on its own. The data collection was done with a 0.002°step size in 2θ. Due to the different preparation steps, the amount of sample ending up in the XRD was not exactly the same for the different samples. In figure 5.3 the untreated patterns of four samples are presented: a TPH reduced sample (in black), a sample treated in 5% methane for two hours at 226 °C (in red), a sample treated in 5% carbon monoxide for two hours at 226 °C (in blue), and a sample treated in 5% carbon monoxide for two hours at 226 °C and then regenerated by TPH (in green). Apart from the samples prepared as mentioned, the untreated, off-the-shelf catalyst support was included. In addition, a reference pattern for nickel by Rouquette et al. [90] and a reference pattern for nickel carbide by Huba et al. [91] was plotted underneath.

The peaks in figure 5.3 not owing to the alumina are clearly nickel as judged by the alumina pattern and the nickel reference pattern. There is no evidence of nickel carbide since multiple diffraction peaks are not detected e.g. the second most intense at $\sim 42^\circ$ and nor the fourth most intense at $\sim 58^\circ$. Also no nickel oxide was detected which since the nickel nanoparticles were only expected to be oxidised on the surface was also not expected.

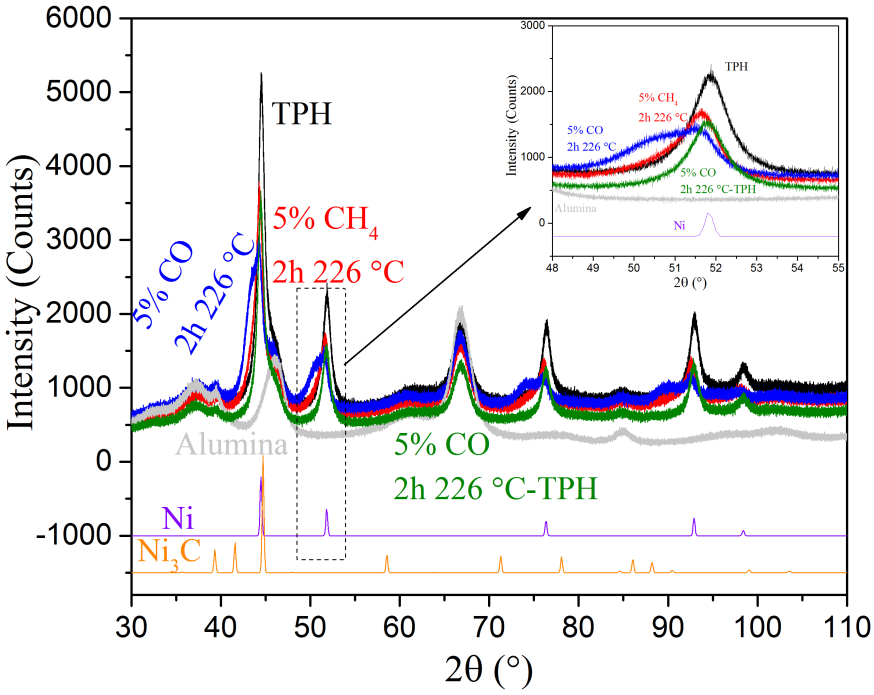

*Figure 5.3: XRD patterns by copper radiation of the catalyst support in grey, a TPH reduced sample in **black**, a sample treated in 5% methane for two hours at 226 °C in **red**, a sample treated in 5% carbon monoxide for two hours at 226 °C in **blue**, and a sample treated in first 5% carbon monoxide for two hours at 226 °C and then regenerated by TPH in **green**. In **purple** the reference pattern of nickel by Rouquette et al. [90] from the ICSD and in **orange** the reference pattern of nickel carbide by Huba et al. [91] from ICSD.*

Immediately apparent in the patterns in figure 5.3 is that compared to the TPH-sample peaks, all the nickel peaks of the 2 hour 5% CO and 5% CH_4 exposed samples are shifted to lower angles. The shift to lower angle indicates a larger lattice constant and can as explained therefore provide evidence for dissolved carbon. As a consequence the shift may serve as part of the explanation of why the intense TPH peak of CO/CH_4 surface probing measurements in figure 5.2 required more than one peak for fitting; one for surface carbide and the second for dissolved carbon.

Difference in intensities in the XRD patterns in figure 5.3 may originate from the fact that the amount of sample in each measurement was different and is therefore not discussed. Besides the visible shift in nickel peak positions, the 5% CO sample also has a clear shoulder at lower angles of each nickel peak. It could possibly be a nickel-aluminium-carbon phase [92] according to a quick search of the ICSD database available in the XRD software, HighScore Plus. Interestingly, a TPH removes the shoulder and shifts the nickel diffraction peaks essentially back to the

position of the TPH-reduced sample as seen from the green pattern in figure 5.3. The patterns in figure 5.3 were fitted in the HighScore Plus software with individual but very similar backgrounds. The Pseudo-Voigt function was used with identical Gaussian and Lorentzian coefficients for all fits and no instrumental parameters were included in the fitting. This was a simple analysis but it was expected to suffice. In figure 5.4 the resulting fit along with the raw pattern are plotted for both the 5% CH_4 measurements (figure 5.4a) and 5% CO (figure 5.4b).

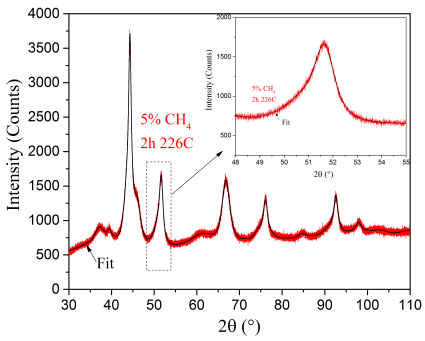

(a) XRD pattern of a catalyst treated in 5% methane for two hours at 226 °C and the fit.

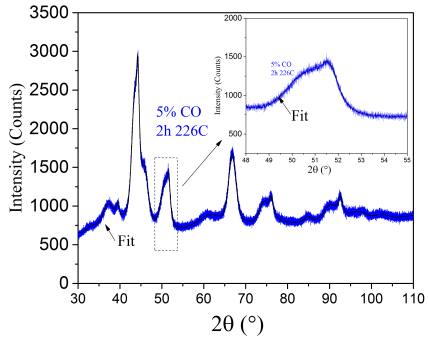

(b) XRD pattern of a catalyst treated in 5% carbon monoxide for two hours at 226 °C and the fit.

Figure 5.4: XRD patterns and fit for samples exposed to CH_4 and CO.

Based on multiple measurements on a silicon standard, a systematic error of 0.036° in 2θ was observed, and the entire pattern for all samples were corrected accordingly. Listed values of angles have equally been adjusted by this offset. In table 5.2 extracted nickel peaks based on the profile fits for the four catalyst samples in figure 5.3 are presented along with the calculated lattice spacings using equation (2.1), lattice constants using equation (2.2) and the relative increase in lattice constant with respect to the sample that had only experienced TPH to 850 °C.

Sample	Peak Position	hkl	d (Å)	a (Å)	Δa %
TPH	44.564 °	111	2.032	3.519	0
5% CH_4	44.342 °	111	2.041	3.535	0.475
5% CO	44.260 °	111	2.045	3.542	0.652
5% CO-TPH	44.488 °	111	2.035	3.524	0.162
TPH	51.848 °	200	1.762	3.524	0
5% CH_4	51.662 °	200	1.768	3.536	0.400
5% CO	51.538 °	200	1.772	3.544	0.625
5% CO-TPH	51.818 °	200	1.763	3.526	0.119
TPH	76.446 °	220	1.245	3.521	0
5% CH_4	76.116 °	220	1.250	3.534	0.367
5% CO	76.022 °	220	1.251	3.538	0.473
5% CO-TPH	76.384 °	220	1.246	3.524	0.069
TPH	92.982 °	311	1.062	3.523	0
5% CH_4	92.596 °	311	1.066	3.534	0.321
5% CO	92.544 °	311	1.066	3.535	0.365
5% CO-TPH	92.930 °	311	1.063	3.524	0.043

Table 5.2: Based on the Pseudo-Voigt fitting of the XRD pattern in figure 5.3, the lattice spacing, d, is calculated through equation 2.2 for the peaks of Ni(111), Ni(200), Ni(220), and Ni(311) for all three samples. The lattice spacing is converted (through equation 2.1) to the lattice constant, a, by which the relative increase (Δa) to TPH sample for the 2h 5% CH_4, 2h 5% CO and 2h 5% CO followed by TPH samples is calculated.

The calculated values for increase in lattice constant with respect to the TPH value confirm what was visible in figure 5.3; nickel peaks are shifted to lower angles for the samples exposed to CH_4 and CO and the CO-TPH, although still shifted, is shifted significantly less. Ergo, it has been determined that the nickel lattice parameter is bigger for the 2 hour 5% CO exposed sample and the 2 hour 5% CH_4 sample than for the sample that has been reduced by TPH consistent with carbon dissolved into the nickel lattice. Equally, it seems the TPH after the 5% CO exposure pulls the dissolved carbon out. The slight shift still visible may suggest that some dissolved carbon is still in the nickel lattice or it may be related to the uncertainty of the measurements.
As mentioned, presence of dissolved carbon could explain why the intense TPH peaks in figure 5.2 and 5.1 were fitted by two peaks. Since the low temperature TPH peak at ∼200 °C in figure 4.2 in chapter 4 was fitted by two peaks in a similar way as for the CH_4 and CO TPH curves, it reasons to analyse samples from methanation experiments by XRD as well.

The methanation samples were prepared in the activity setup, transferred to the XRD and the data was treated the same way including the adjustment due to the systematic error in 2θ of 0.036°. Results for a TPH-reduced sample, a sample having experienced the standard methanation conditions for one hour, a sample having experienced the standard methanation conditions for 58 hours, and a sample that after a long methanation of 150 hours had been treated by a TPH are listed in table 5.3.

Sample	**Peak Position**	**hkl**	**d (Å)**	**a (Å)**	**Δa %**
TPH	44.528 °	111	2.033	3.521	0
1h Meth	44.408 °	111	2.038	3.531	0.257
58h Meth	44.286 °	111	2.044	3.540	0.519
150h Meth-TPH	44.532 °	111	2.033	3.521	0.068
TPH	51.848 °	200	1.762	3.524	0
1h Meth	51.728 °	200	1.766	3.532	0.216
58h Meth	51.571 °	200	1.771	3.542	0.498
150h Meth-TPH	51.864 °	200	1.761	3.523	0.036
TPH	76.410 °	220	1.245	3.523	0
1h Meth	76.236 °	220	1.248	3.530	0.193
58h Meth	76.084 °	220	1.250	3.536	0.363
150h Meth-TPH	76.426 °	220	1.245	3.522	0.022
TPH	92.946 °	311	1.062	3.524	0
1h Meth	92.734 °	311	1.064	3.530	0.176
58h Meth	92.596 °	311	1.066	3.534	0.291
150h Meth-TPH	92.952 °	311	1.062	3.523	0.025

Table 5.3: Based on the Pseudo-Voigt fitting of the XRD patterns for TPH-reduced sample, 1 h methanation sample, 58 hour methanation sample, and a sample of 150 hour methanation succeeded by TPH, the lattice spacing, d, is calculated through equation 2.2 for the peaks of Ni111, Ni200, Ni220, and Ni311 for all three samples. The lattice spacing is converted (through equation 2.1) to the lattice constant, a, by which the relative lattice constant increase (Δa) to TPH sample for methanation samples is calculated.

In table 5.2 and 5.3, it is clear that the lattice constant is increased for all four samples that had been exposed to either CO, CH_4, or methanation conditions which therefore could be expected to contain carbon. As mentioned, no nickel oxide was observed and the increased nickel lattice constant cannot be explained by nickel oxide. The lattice parameter of nickel oxide is either significantly larger [93] or smaller [94] depending on the specific crystal structure. Thus, the expansion can be explained by carbon dissolving into the nickel particles. However, dissolved

carbon would affect all planes in the nickel and therefore that the lattice expansion decreased with increasing diffraction angle in both table 5.2 and 5.3 is peculiar and suggests that the simple data analysis was too simple.
Thus, full profile data analysis was attempted. Using the TOPAS software out-of-house, a Rietveld analysis by the fundamental parameter method was performed on all seven samples discussed so far in this section on XRD. The XRD pattern, the resulting fit and the difference curve for the 2 hour 5% CH_4 analysed in TOPAS are shown in figure 5.5. The residual curve in figure 5.5 reveals an overall good fit.

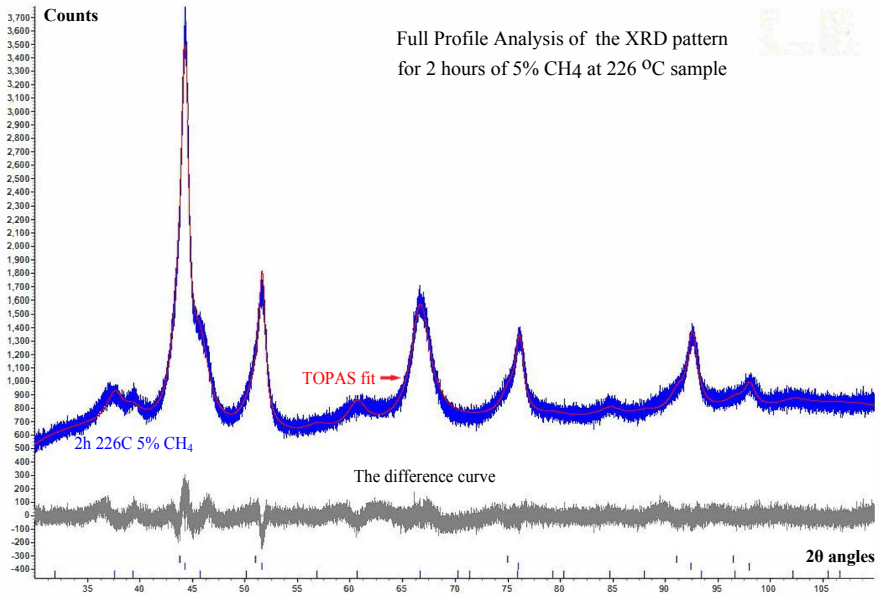

Figure 5.5: TOPAS analysis of the 2 hour 5% CH_4 at 266 °C treated sample XRD pattern, the resulting fit and the difference curve.

As the full profile is fitted, all angles are taken into account in the result so only one lattice constant and one crystallite size for a specific crystal structure is extracted. The results for all the samples mentioned so far are listed in table 5.4.

Sample	a1 (Å)	L1 (nm)	a2 (Å)	L2 (nm)	Δa %
TPH	3.527	11	•	•	0
5% CH_4	3.536	14	3.580	7	0.255
5% CO	3.531	14	3.590	6	0.113
1h Meth	3.531	10	•	•	0.113
58h Meth	3.535	13	3.570	8	0.198
150h Meth-TPH	3.527	12	•	•	0
5%CO-TPH	3.527	11	•	•	0
1h Meth [alt]	3.525	14	3.541	8	-0.057

Table 5.4: Results of a Rietveld analysis by the fundamental parameter method in TOPAS on the measured XRD pattern for the samples of table 5.2 and 5.3. The lattice constant and crystallite size for phase 1 and if fitted with a second phase also the lattice constant and crystallite size for phase 2 are listed as well as the relative to the TPH increase in lattice constant for phase 1 (Δa) in percentage. The 1h Meth [alt] is an alternative fit for the 1 hour methanation sample, the difference being whether or not the second nickel phase is fitted.

The full profile analysis confirms results found by the simple peak analysis; the nickel lattice constant was larger for the samples that could be expected to contain carbon due to their respective treatment. Based on all three tables of results (5.2, 5.3 and 5.4), the samples where the carbon was removed by TPH could still contain some carbon but could equally well be a measure of the uncertainty of these analyses.

Full profile analysis revealed a second nickel-related phase. This phase has the FCC crystal structure of nickel but could appear to contain some aluminium. The second phase was required to yield a good fit for the samples that might contain carbon but the lattice constant for the regular nickel phase was still enlarged. The 1 hour methanation was a special case which could be fitted reasonably well both with and without phase 2, suggesting very little of phase 2. However, based on the consistency of the other results, it seems phase 2 is necessary as otherwise the crystallite size of phase 1 is too small (smaller than the TPH sample which physically makes little sense) but the results listed for phase 2 for the 1 hour methanation do also not appear consistent as the lattice constant of phase 2 is very small and the crystallite size of phase 1 quite big (bigger than the 58 hour methanation sample). Also, it is surprising how little the nickel lattice parameter is increased for the 5% CO as compared to the 5% CH_4 since by naked eye the peak position appeared more similar. It appears that further refinement is necessary. It might yield a good result to fix the second nickel phase to a lattice constant of 3.58 Å. Since the two nickel phases are similar, their overlap affects the fitting which may be solved by fixing one of the phases. Further analysis is expected to be published (see article 2 abstract appended to this thesis). It is simply noted here that the

presence of the second phase and its overlap with the first nickel phase may be the root of the inconsistencies. Another source for error is the instrument description that is incorporated in the Rietveld fit and may not have been sufficiently accurate.

XRD has thus justified that the surface carbide peak in the TPH after CO or CH_4 exposure as well as methanation conditions can be fitted by two low temperature peaks similar to the findings by McCarty et al. [39]. However, based on our XRD data the second peak is assigned to dissolved carbon as opposed to bulk nickel carbide. Though in opposition to McCarty et al. [39], it is by no means unheard of for neither CO exposure nor methanation conditions. Kuijpers et al. [95] studied the chemical nature of carbon deposited during CO disproportion at 275 °C. By measuring the magnetisation of nickel which is substantially decreased by CO exposure even for a nickel surface covered by hydrogen, it was concluded that carbon must migrate into the nickel (as filamentous carbon or whisker carbon was not expected to substantially affect the magnetisation). It was found that CH_4 did not give rise to dissolution of carbon. However, Martin et al. [86] adsorbing alkanes at low temperature also found that carbon may dissolve into the bulk at elevated temperatures and Ludlow et al. [88] reported that their results from nickel crystallite thermometry during CO methanation agreed with previous reported findings of interstitially dissolved carbon. Mirodatos et al. [41] found that during CO disproportion bulk nickel carbide was formed due to carbon dissolution into nickel whereas during exposure to a stream of both CO and H_2 the carbide was restricted to the surface. More recently Znak et al. [89] in a similar fashion as we have attempted, found by XRD analysis that the nickel lattice parameter of potassium promoted nickel alumina catalyst increased owing to dissolved carbon during CO methanation. Although not all these results are in complete agreement and clearly more studies are needed to better understand the mechanism of dissolution of carbon during CO disproportion and methanation, it is clear that other groups have found carbon to dissolve into nickel. Some groups [41,95] suggest that the dissolved carbon is not the cause of deactivation but rather high temperature carbon types are which is in good agreement with our results in chapter 4. Furthermore, it was also reported that the process is reversible [41,86,87] and that large amounts of dissolved carbon may be found when graphite nucleation is limited [95]. As we see that the nickel lattice constant is decreased to almost the original value by a TPH after CO exposure and methanation, we equally suggest that the process is reversible. Furthermore, we cannot exclude that the relatively low percentage of dissolved carbon could be related to having graphite nucleation happening if the higher temperature TPH peaks are graphite-like. However, this is contrast to the cyclopolymerisation mechanism favoured so far. Further discussion must follow.

5.3 Desorption Measurements

The combination of surface probing CO/CH_4 experiments and analysing relevant samples by XRD yielded an understanding of the low temperature carbon species from the TPHs in figure 4.2 but the 400 °C and 500 °C TPH peak carbon species remain unexplored. It was established in chapter 4 that the 500 °C TPH peak carbon species was the primary cause for deactivation during long methanation experiments. However, about half the activity remained after 100 hours of methanation despite close to eight carbon atoms per surface nickel atom in this peak. The non-complete deactivation by what is equivalent to an average of almost 4 layers of graphene alludes to that the carbon could be more disordered than graphene and not uniformly deposited on the nickel step sites. In order to discuss whether the carbon was hydrogenated, the experimental procedure was changed from performing TPH after methanation to performing Ar TPD i.e. heating up the catalyst in Ar after reaction. If the carbon formed during methanation contained hydrogen, it would be expected that during the temperature increase, the species would decompose and hydrogen could be detected by the mass spectrometer.
The experimental procedure from chapter 4 was maintained. Thus, the catalyst was diluted and reduced by TPH, building up pressure as well as stabilising temperature was done in H_2 and Ar and methanation was initialised by introducing CO at three bar and 300 °C. Methanation was ended by relieving pressure at 300 °C and once at ambient pressure, flows were stopped, the reactor and setup pumped down and the furnace set to cool. Once the setup had been pumped out three times interspersed by Ar and temperature was below 100 °C, an Ar flow of 40 ml/min was set. Temperature was ramped to 850 °C by 5 °C/min after 1.5 hours. The results of these Ar TPDs are presented in figure 5.6. Hydrogen signals (the $m/z = 2$ ion current) during Ar TPDs succeeding methanation of 2, 24 and 80 hours were plotted as a function of temperature.
As detection of CO and CO_2 desorption could point to oxygenates [96] built up on the surface during methanation, detection of CO and CO_2 was equally relevant. Thus, alongside the hydrogen signals from the three TPD measurements, the CO ($m/z = 28$) and CO_2 ($m/z = 44$) TPD signals after the 80 hour experiment are also plotted. The 80 hour signals were similar in shape but slightly more intense than the same masses for both the 24 hour and the 2 hour experiment except that for the 2 hour only a small CO_2 signal was detected and no CO. Since the detected CO and CO_2 quantities were low, the decomposition of oxygenated species could not fully explain the large hydrogen signals. Equally, the water signal showed no features and was lower than the hydrogen signal, thus, the hydrogen signal also did not stem from water cracking in the mass spectrometer.
In order to determine the $m/z = 2$ background level under relevant conditions, the exact same procedure as the 2 hour, 24 hour and 80 hour experiments of loading catalyst, reduction by TPH, increasing the pressure to 3 bar and stabilising temperature in 40 ml/min H_2 and 60 Ar ml/min was followed but *no CO flow* was started, instead the H_2/Ar mix was continued at the 3 bar and 300 °C as a "methanation without CO". The experiments were ended the same way as for

the standard procedure; relieving pressure at 300 °C, stopping H_2 and Ar flows, pumping out and performing Ar TPD. Both a 2 hour and a 24 hour "methanation without CO" or equivalently H_2/Ar treatment at 300 °C and 3 bar were done but as the m/z = 2 was essentially the same, only m/z = 2 background for the 24 hour treatment is plotted in figure 5.6; named "24h no CO". This may not be the "correct" background as the conditions during methanation would be significantly different to a "methanation without CO", especially since no water was produced when no CO was converted. However, this type of background provided information as to the hydrogen adsorption on the catalyst as well as the alumina that happened due to the procedure.

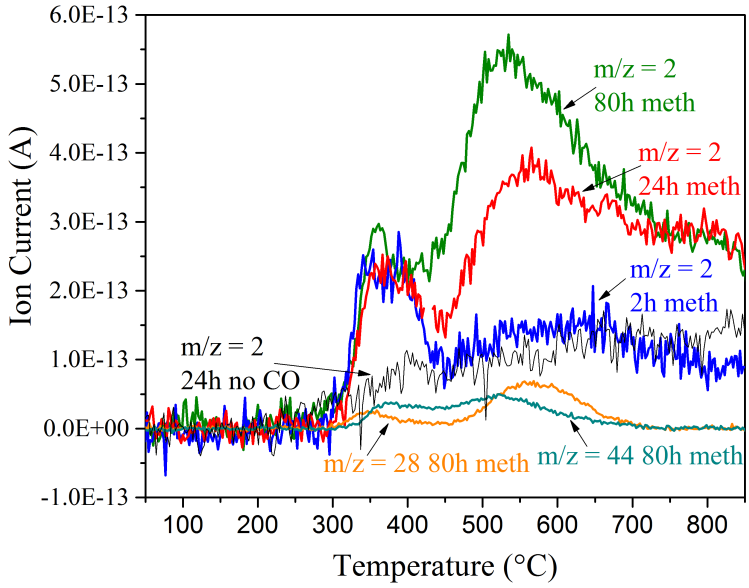

Figure 5.6: In blue, red, and green the hydrogen (m/z = 2) signal during Ar TPDs after 2, 24, and 80 hours of methanation respectively is plotted as a function of temperature. Also included are the CO (m/z = 28) and the CO_2 (m/z = 44) TPD signals after the 80 hour methanation. As an attempted background the hydrogen signal during an Ar TPD following a H_2/Ar treatment similar to methanation i.e. hydrogen on the surface without carbon.

It is clear that the m/z = 2 signals during the Ar TPDs show two desorption temperature regions; <450 °C and >450 °C. The low temperature region between 300 - 450 °C is significantly sharper and very similar for all three Ar TPDs following methanation for 2 hours, 24 hours and 80 hours. This sharp feature is not seen for the background based on "24h no CO". The second region from 450 °C only rose above the background based on "24h no CO" for the 24 hour and 80 hour methanation experiments. It is interesting how well this fits with the results in figure 4.2 in section 4 where most TPH curves had a very similar methane desorption peak at ∼400 °C and only long methanation measurements showed the ∼500 °C peak. All in all, the results so far point to that the carbon on the surface is to some extent hydrogenated.
A quantification of the hydrogen released during the Ar TPDs and its relation to the methane desorption in TPHs could possibly yield the hydrogen-to-carbon ratio of the carbon formed during methanation. However, it is required that all or at least by far most of the hydrogen in the Ar TPDs in figure 5.6 come from carbon on the surface to easily make sense of the results.
For the calculations the background level ("24h no CO") was subtracted from the 24 hour methanation m/z=2 signal after having been matched by linear interpolation. The resulting curve was integrated yielding the full hydrogen amount. This curve was fitted by Gaussian fits in analogy to the TPH analyses in section 4. Hereby the area under the first feature roughly below 450 °C in figure 5.6 and the area under the broad feature above 450 °C in figure 5.6 were determined. The values were normalised by the ratio in the MS detection of hydrogen and methane when flowing equal molar quantities (M2/M15 = 1.36). Due to the Gaussian peak fitting of the TPH peaks of figure 4.2 a similar analysis had already been performed for the carbon related signal. These results are combined in table 5.5 where the area by integration of the full curves of both the TPH and the Ar TPD after 24 hour methanation ("total"), and the area of respective fits of relevant features are listed.

The ratio of hydrogen-to-carbon for the full temperature range was found to be as high as five which exceeds the ratio for methane. Therefore, other species than the surface carbon must provide some hydrogen, possibly explaining the large broad hydrogen desorption feature above 450 °C which gave a ratio as high as H/C = 8. However, the ratio is so large that hydrocarbons cannot explain it although dehydrogenation of stable olefinic, aromatic and graphene-like local configurations, molecules and thin films is found in the temperature range of 325-625 °C [55,97–104] which match both the temperature of our TPHs and TPDs. However, none of the H_2 desorption features observed is likely related to that of well-structured graphene sheets which according to results by Zhao et al. display a high-temperature H_2 desorption peak at ∼600 K (∼327 °C) [97], significantly lower than the ∼650 (∼377 °C) peak we observe, and this is despite a drastically faster temperature ramping rate, 180 K/min by Zhao et al. [97] compared to our 5 K/min. As mentioned, the detection of CO and CO_2 suggest some oxygenated carbon species which can also release hydrogen under thermal decomposition [96,105].

	M15 (C)		$M2_{norm}$ (H)	H/C
Total	3.43E-10	Total	9.02E-10	5
∼400 °C peak	9.90E-11	<450 °C peak	1.03E-10	2
∼500 °C peak	1.74E-10	>450 °C peak	7.16E-10	8

Table 5.5: Values to determine hydrogen-to-carbon ratio of carbon species on the surface after methanation. The carbon values (M15) (after background subtraction) are the area of 24 hour TPH curve ("total"), the area of the fit of the peak ∼400 °C and the area of the fit of the peak ∼500 °C. The hydrogen values (M2) (after background subtraction and normalisation to the relative MS detection sensitivity) are the area of the full TPD curve ("total"), the area of the fit of the peak <450 °C and the area of the fit of the broad peak >450 °C. In the fifth column the ratio of H/C is calculated i.e. the ratio of the mass spectrometer signals times two as M2 is the measuring of H_2.

However, as the amounts of CO and CO_2 were so low, it was not sufficient to explain the large H/C ratio. In addition, the lack of methane desorption at ∼227 - 327 °C in the TPHs in figure 4.2 which is the expected region for oxygenates on nickel alumina [105], also suggested that very few oxygenates were adsorbed during the methanation measurements. Thus, it seems the bulk of this hydrogen above 450 °C must originate from other sources than the surface carbon. As water is formed from OH-species [63], OH-groups on the alumina formed during the methanation could oxidise both carbon and the nickel leading to H_2 release during the TPD.
The H/C = 2 found for the 400 °C TPH peak although still a large ratio seems more reasonable especially considering the above discussion on some contribution from oxygenates and/or OH-species. Also the lack of a 500 °C peak for the two hour methanation in the TPH (figure 4.2) and no broad feature above 450 °C is consistent with the 400 °C TPH species being hydrogenated and giving rise to the M2 peak at 300 - 450 °C.
Thus, it appears that the carbon at 400 °C could be hydrogenated which is consistent with carbon formation based on CH* coupling to form C_2H_2 and eventually more graphene-like carbon as found by Yang et al. [55] and the similar cyclopolymerisation mechanism during Fischer-Tropsch proposed by the group of Weststrate and Niemantsverdriet [62,63]. Equally it is in line and well-aligned with the interdependence of the 400 °C and 500 °C peaks of the TPHs in figure 4.2, signifying a transformation of hydrogen-containing carbon species becoming more purely carbon.

5.4 Visualisation by Electron Microscopy

In the attempt to see the structured carbon expected to at least in part make up the two high temperature TPH peaks, a catalyst having performed methanation for almost 60 hours was analysed in a TEM. The TEM was the FEI Titan E-Cell 80-300ST TEM which is a 300 kV monochromated FEG equipped with a CESCOR C_s spherical aberration corrector for the objective lens at DTU CEN, building 314. High energy electrons have wavelengths in the picometer range, theoretically giving atomic resolution. In TEM a parallel beam of electrons is directed at the sample where they might be scattered and the transmitted electrons are detected. Heavier or thicker elements will scatter electrons more than lighter or thinner and these may be cut off by the aperture, giving rise to mass-thickness contrast [106] which means for this work that nickel and alumina should be distinguishable but also that light elements such as carbon should be detectable. Helveg et al. have e.g. recorded the growth carbon nanotubes from nickel nanoparticles in HRTEM [107]. The preparation was simple in the attempt to not disrupt the carbon on the surface so the lacey carbon grid was dropped into the vial of catalyst sample and after the vial had been shaken, the grid was extracted and inserted into the microscope. Initially, it was determined that beam effects could be observed depending on the electron dose and therefore the dose was kept below the observed threshold of beam effects. Typical dose was 1000 e/nm^2/s.
In figure 5.7 an overview-like image is presented where nickel particles can be distinguished from alumina by the mass-thickness contrast although one must be careful to not confuse thicker layers such as overlapping alumina with nickel. As expected, the nickel particles seem fairly well dispersed.

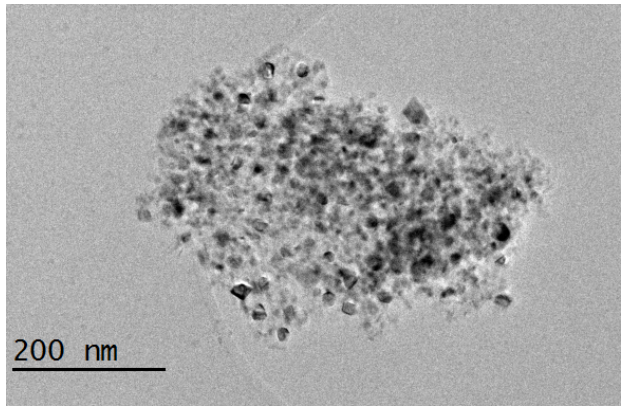

Figure 5.7: Low magnification image of 60 hour methanation sample.

In figure 5.8 a high resolution image of the same sample is presented. A ∼20 nm nickel particle is seen which appeared to have a different contrast on the edge as compared to the bulk of the particle.

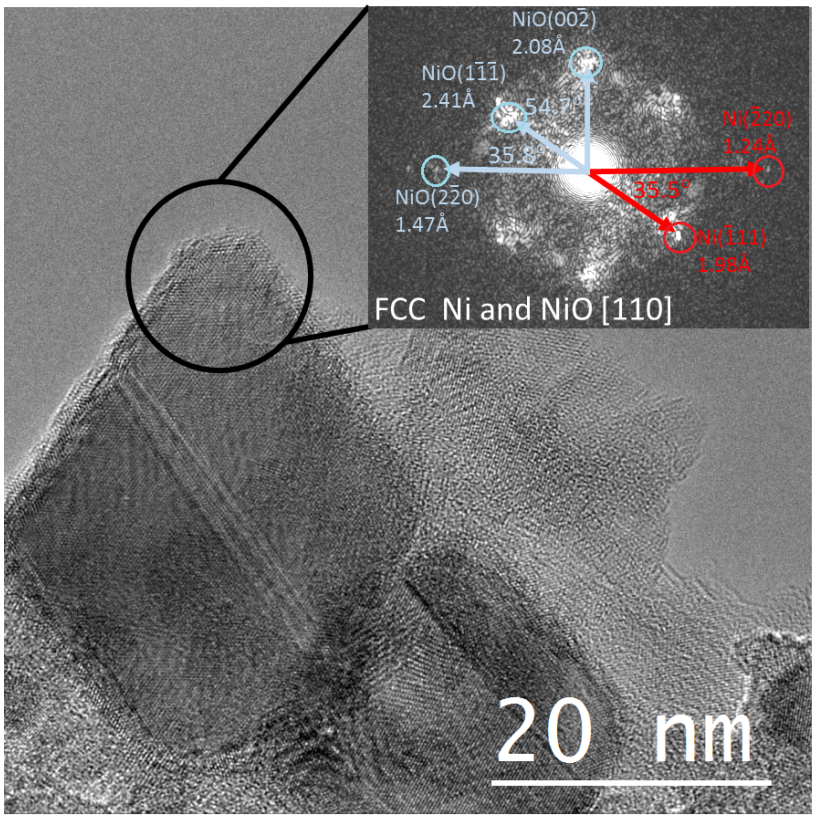

Figure 5.8: High resolution image of the 60 hour methanation sample and the inset shows the fast fourier transformation.

In a crystalline sample the electron wave will be scattered according to the crystal structure which gives rise to a phase contrast as illustrated in image 5.9. By performing fast fourier transformation (FFT) diffractograms are formed. The information in such diffractograms resembles that of the reciprocal space which enables analysis of crystal structure. The high resolution transmission electron microscope (HRTEM) image of a nickel particle along with the diffractogram produced by FFT are shown in figure 5.8 and the figure inset. It is seen that the nickel planes ($\bar{1}\,1\,1$) and ($\bar{2}\,2\,0$) and the nickel oxide planes ($1\,\bar{1}\,\bar{1}$) and ($\bar{2}\,2\,0$) lie on the same axis suggesting the oxide is growing epitaxially on the nickel. According to structural information by Rouquette et al. [90] the Ni(111) lattice parameter is 2.0367 Å and the lattice parameter of Ni(220) is 1.2472 with an 35.2 °angle between these planes. This is well matched by the planes measured in the high resolution image where the Ni($\bar{1}\,1\,1$) gives 1.98 Å and Ni($\bar{2}\,2\,0$) gives 1.24 Å, meaning an error of less than 3% compared to the database values provided by Rouquette et al. [90]. The angle of 35.2 °between the Ni(111) and the Ni(220) listed by Rouquette et al. [90] also matches the measured value in the diffractogram of 35.5 °. A similar

good agreement is seen for nickel oxide where according to Sasaki et al. [93] for NiO(111) the lattice parameter is 2.4122 Å, 2.0890 Å for NiO(002), and 1.4771 Å for NiO(220) and in HRTEM the values were found to be 2.41 Å for NiO($1\,\bar{1}\,\bar{1}$), 2.08 Å for NiO($0\,0\,\bar{2}$), and 1.47 Å for NiO($2\,\bar{2}\,0$). Angles in the image were 54.7 °between NiO($0\,0\,\bar{2}$) and NiO($1\,\bar{1}\,\bar{1}$) and 35.8 °between NiO($1\,\bar{1}\,\bar{1}$) and NiO($2\,\bar{2}\,0$) matching the database values of 54.7 °between NiO(0 0 2) and NiO(1 1 1) and 25.2 °between NiO(1 1 1) and NiO(2 2 0) well. No fringes that matched graphene or other well-defined carbon structures were observed, nor did the mass-thickness contrast resolve any carbon structures.

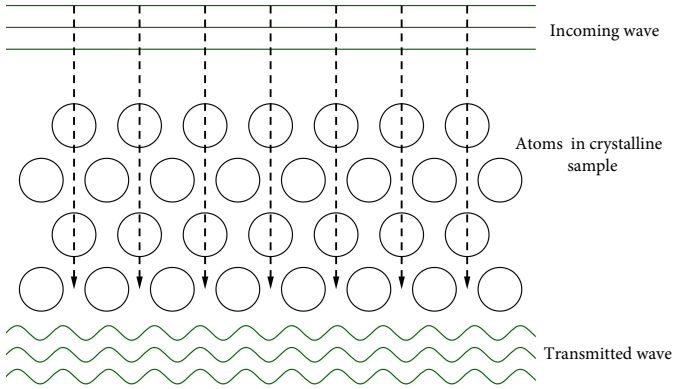

Figure 5.9: Illustration of phase contrast by crystalline sample.

It seems the lighter edge on the nanoparticle was due to the nickel being oxidised, most likely an effect of handling, storage and transportation etc. in between the methanation experiment and the TEM. However, as carbon in amounts of up to equivalent to four layers of graphene was expected on the surface, it is surprising no carbonaceous species were observed. Although we expected to observe structured carbon species, Moeller et al. [108] suggest that unless filamentous carbon is formed, it is difficult to observe the carbon by TEM. Moodley et al. [60] showed elemental mapping evidence of carbon situated across both cobalt particles and the alumina support but did not observed graphitic carbon in conventional HRTEM. Tan et al. [59] though observed layered carbon with a spacing matching graphite although the carbon was not sufficiently ordered to be graphite and they also observed amorphous carbon. So although carbon should be observable, it may not be as straight forward as expected.

As no carbon structures were observed in the TEM, the same 60 hour methanation sample was analysed at Aarhus University, Interdisciplinary Nanoscience Center, Inano by STEM EDS. The equipment is a FEI Talos FEG equipped with 4 EDS detectors giving supreme elemental sensitivity. In STEM the electron beam is focused and scanned across the sample surface where the electrons scatter and

are detected based on the scattering angle [106] as seen in image 5.10. In EDS x-rays are generated by the scanned electron beam as the beam excite atoms which upon relaxation emit characteristic x-rays. Therefore EDS is an elemental analysis technique [106].

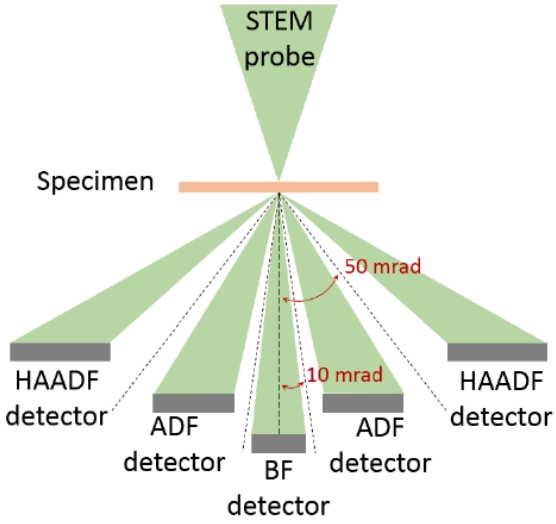

Figure 5.10: Schematics of the electron detection in STEM. Reprinted from [109].

The sample was again dry-deposited but on a SiN/Si grid (20 nm SiN) which had previously been plasma cleaned for two minutes to remove carbon. Nine areas were analysed with 200 kV and a dose of almost 4000 e/Å^{2}s. The beam was on each area for 10 minutes but beam induced carbon formation from residual gasses in the chamber can be rejected as there was no visible difference between an area measured for 10 minutes and only 2.5 minutes.
The STEM EDS data is shown in figure 5.11. In figure 5.11b, 5.11c and 5.11d the nickel and carbon counts are presented with colour coding.

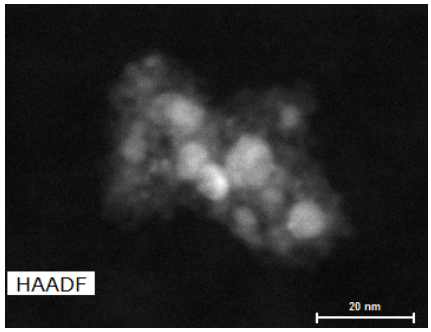

(a) The HAADF image of analysed area.

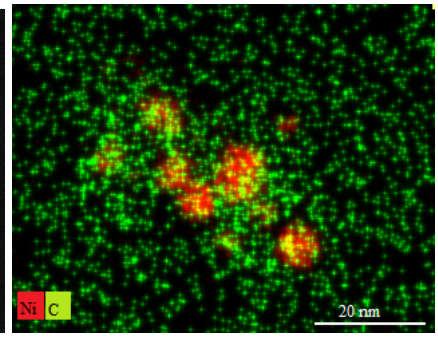

(b) Nickel (red) and carbon (green) in the analysed area by EDS.

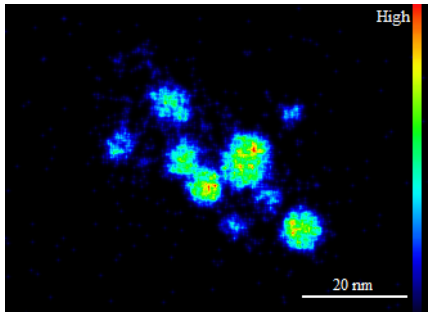

(c) The nickel count by the EDS detectors. The more red the colour the higher the count.

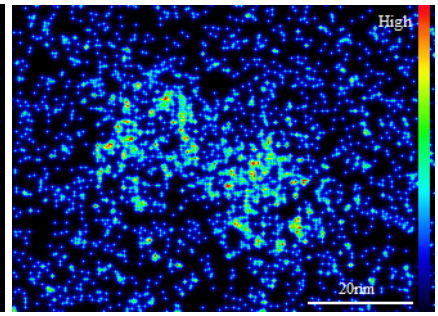

(d) The carbon count by the EDS detectors. The more red the colour the higher the count.

Figure 5.11: Images from HAADF and STEM EDS analysis by 200 keV and 3960 $e/Å^2 s$

For the image in figure 5.11b carbon is green and the intensity green-colour coded and similarly for nickel in red. It is still difficult to distinguish low counts from high counts. However, it is included because it is very intuitive to have the carbon and nickel overlaid on each other. For a better view on the concentration of nickel and carbon, the red-to-blue scale in figure 5.11c and 5.11d provide more information. It is clear that there is carbon all over both on the nickel and alumina, not entirely unlike the mentioned elemental mapping of carbon and cobalt in [60]. Though it appears to be concentrated with higher counts in proximity to the nickel particles. The carbon is not shell-like but rather dispersed possibly concentrated in "lines". It appears the carbon formed during methanation is inhomogeneously covering the nickel particles which may explain why it was hard to observe as well as why a lot of activity remained during long methanation experiments.

5.5 Conclusion on the Carbon Species

In this chapter the carbon deposited during CO methanation at 300 °C and 3 bar was investigated. TPHs succeeding CH_4 and CO exposures gave a similar low temperature methane desorption peak at roughly 200 °C as the TPHs following methanation experiments in the previous chapters. It was found that a combination of two Gaussian peak fits, fitted the curve well. One of these Gaussian matched the expected surface carbide well as its area could be approximated to roughly 0.5 C/Ni_{surf}. By ex-situ XRD analysis, it was clearly determined that the nickel lattice was larger for samples that had either been exposed to CH_4, CO, or methanation which can be explained by carbon dissolved into the nickel. It was therefore concluded that the second Gaussian fit for the TPHs following both CH_4 and CO exposures and methanation was because of the dissolved carbon. As the nickel lattice had decreased in size after regeneration by TPH, it follows the dissolved carbon must indeed be hydrogenated to form methane during TPHs. Ar TPDs indicated that some carbon species formed during methanation might contain hydrogen; the 400 °C TPH peak might be hydrogenated, whereas this could not be concluded for the 500 °C TPH peak. By electron microscopy, based on the non-shell carbon appearance and the rather high activity still maintained by the catalyst during methanation despite almost an average coverage of equivalent to four layers of graphene, it seems the carbon is strongly inhomogeneously distributed over the nickel particle surfaces.

6

Changes to the Methanation Conditions

In this chapter the influence of temperature and nickel particle size on carbon formation is under investigation. As was clear from the literature discussion in chapter 1, experimental conditions such as temperature generally affect carbon deposition. Effects of particle size were not discussed however, as catalysis is a surface process, it is intuitive that the nature of the surface will play into the performance of a catalyst. Indeed catalytic activity and stability is known to be affected by the particle morphology, shape and size [110,111].
The experimental conditions were as close to the original procedure as possible to study only the particular alteration to the methanation experiments. The results are preliminary and included are some first results on the effect of higher total pressure.

6.1 Effect of Temperature on Surface Carbon

So far methanation was performed at 300 °C, which was judged to be a relevant temperature for studying low temperature carbon formation. However, to push the reaction further even lower temperatures are equally interesting and thus, methanation at a temperature close to the 300 °C and significantly lower than the 300 °C were investigated. The catalyst was reduced by TPH, followed by methanation experiments of 270 °C or 225 °C, and carbon deposition was analysed by another TPH. Due to an expected lower initial conversion at lower temperature, six times the amount of catalyst compared to 12.5 mg loaded for 300 °C methanation experiments was loaded for the 225 °C experiments whereas for 270 °C the weight of catalyst was not adjusted. Thereby a similar initial CO conversion of ∼6% for the 270 °C and 225 °C methanation experiments was achieved. Thus, they can easily be compared to each other but the initial conversion was lower than the initial CO conversion of ∼16% for the 300 °C methanation experiments.

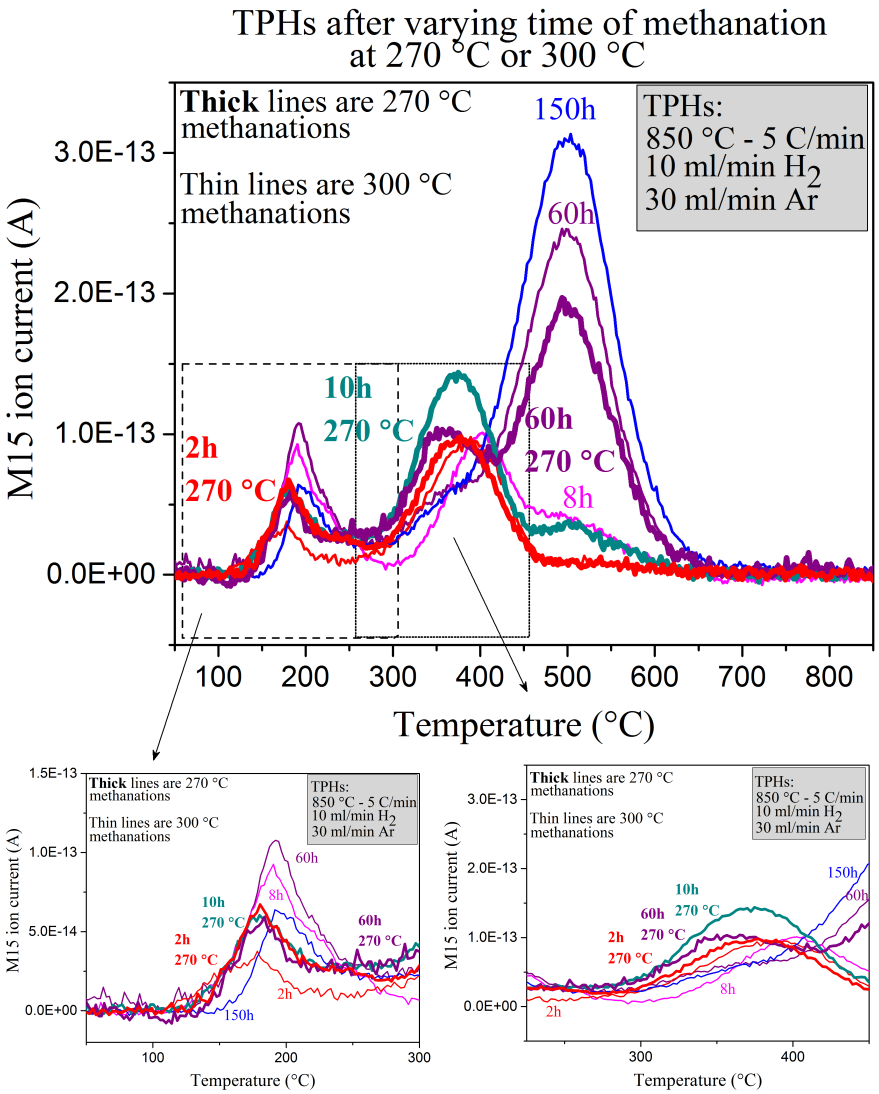

Figure 6.1: TPH curves of similar duration methanation at either 270 °C (thick lines) or 300 °C (thin lines) and 3 bar with 1:4 CO-to-H_2 ratio and pCO = 0.3 bar.

In figure 6.1 the TPH curves that succeeded 270 °C methanation experiments are presented along with the comparable 300 °C curves from figure 4.2.

It is immediately apparent that the carbon species formed during the 270 °C methanation are very similar to the carbon formed during 300 °C methanation, since the same three TPH peaks are observed at near-identical temperatures. The ∼200 °C TPH peaks for all three TPHs following methanation at 270 °C are almost identical in agreement with findings by Mirodatos et al. [41,42] who found that carbon species observed below 250 °C in TPH following methanation at 234 °C were not affected quantitatively by methanation duration. Contrary to their findings, based on the results for the low temperature TPH carbon formed in methanation at 270 °C versus 300 °C, it does not seem the amount increases with decreasing methanation temperature. However, the low temperature peak of TPHs after the 300 °C peak methanation experiments were less identical making the comparison difficult. Also it could seem the 270 °C methanations were less affected by the shutdown procedure after methanation and in combination with the sharper low temperature TPH peaks, it could appear that the balance between carbide and dissolved carbon was different after shutdown compared to methanation at 300 °C. It is not unlikely that less carbon dissolved into the nickel at 270 °C compared to at 300 °C due to slower kinetics as it would also explain why for methanation experiments by Mirodatos et al. at temperatures lower than 250 °C, they claim there is no "interstitially" bound carbon. These samples were due to time limitation not examined by XRD but it certainly seems it could be worthwhile in the attempt to confirm this change in carbide versus dissolved carbon balance.
The methane desorption peaks at ∼400 °C of the TPHs succeeding methanation at 270 °C are broader than the methane desorption peaks of the TPHs succeeding methanation at 300 °C. This could be explained by slightly less homogeneous carbon species. Based on both the 10 and 60 hour of the TPHs following methanation at 270 °C, it equally seems that significantly more of this ∼400 °C TPH peak carbon species was present than for similar methanation duration at 300 °C. The 400 °C TPH peak after 60 hours methanation at 300 °C appeared visually as a shoulder whereas for the 270 °C it is visually a distinct peak. In combination, it appears the transformation from the ∼400 °C TPH peak carbon species to the ∼500 °C carbon species was slower at 270 °C. This is also seen from a lower ∼500 °C TPH peak after 60 hours of methanation at 270 °C.

In figure 6.2 TPH curves for methanation at 225 °C for 2, 10 and 60 hours are plotted along with some of the TPH curves following 300 °C methanation measurements.

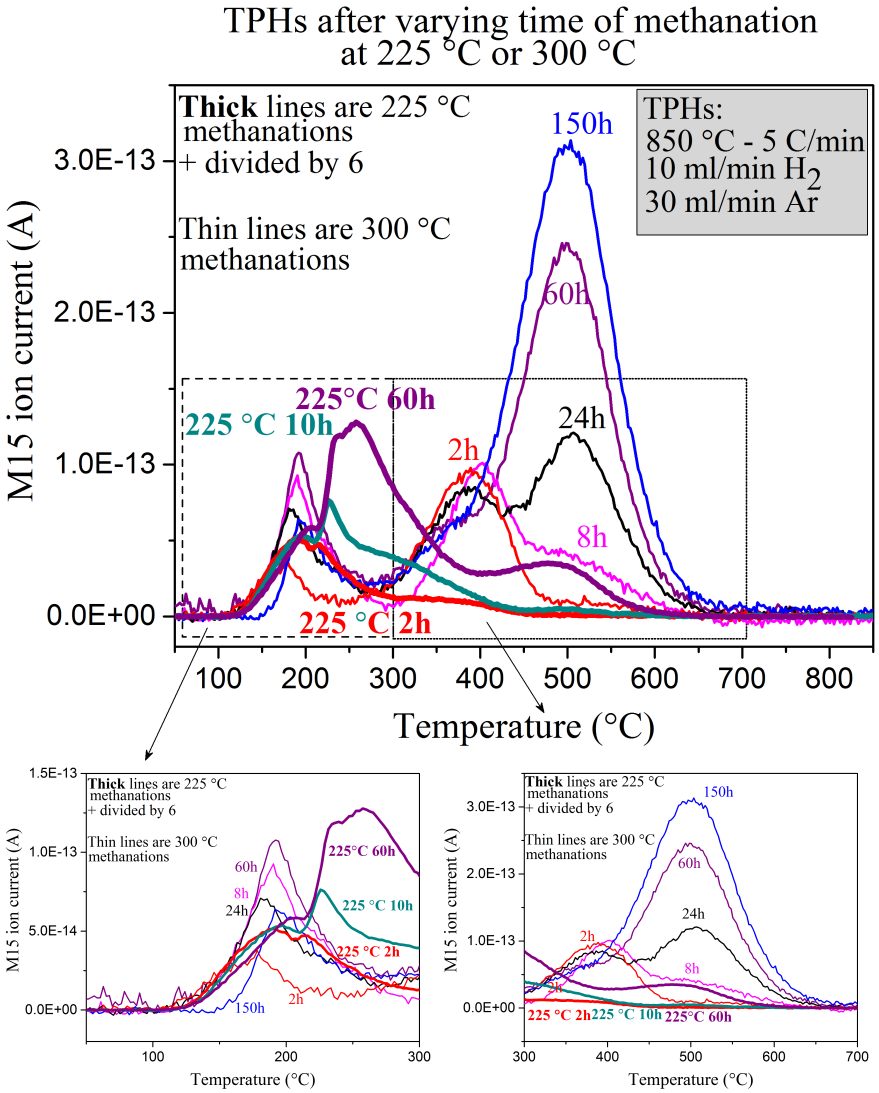

Figure 6.2: TPH curves of similar duration methanation at either 225 °C (thick lines) or 300 °C (thin lines) and 3 bar with 1:4 CO-to-H_2 ratio and pCO = 0.3 bar. The TPH curves after 225 °C methanation has been divided by 6 as a normalisation to catalyst amount and thus also surface area.

The difference in the TPH curves after methanation at 225 °C compared to both the TPHs after 270 °C and 300 °C methanation is striking and clearly different carbon species may be formed. The most striking feature is that at least one new peak has appeared. For the TPHs following methanation at 300 °C, there was no methane desorption between ∼ 250 °C and 300 °C, whereas in this temperature region the strongest desorption peak is observed for TPHs following methanation at 225 °C. Incidentally, as discussed earlier, this is the temperature region where oxygenates may be hydrogenated. Thus, it seems significantly more oxygenates are adsorbed during methanation at 225 °C. This is in good agreement with TPH curves after methanation at 234 °C by Mirodatos et al. [42] who concluded that the intermediate TPH peak carbon must be formate. However, the shape (a combination of broad peaks and spike-like peaks) suggests more carbon types than one. It seems the low temperature peak assigned to carbide and dissolved carbon and the new intermediate peak overlap and it is difficult to conclude that no other carbon types may be present. It is also very clear, that very little methane desorbed at 400 °C and the growth rate of the 500 °C TPH carbon species is much slower at 225 °C methanation than at 270 °C and 300 °C methanation. Thus, the 400 °C and 500 °C TPH peak carbon species have significantly slower formation kinetics during methanation at 225 °C. All in all, it seems carbon species formed during methanation at 225 °C was very different to methanation at 270 °C and 300 °C.

In analogy to the data analysis in chapter 4 and the results in figure 4.3, the carbon atoms-to-nickel surface atoms ratio was calculated based on the TPH curves and plotted as a function of TOS in figure 6.3. Lines have been added as guides-to-the-eye only to assist the reader but employing no mathematical functions nor fitting. The total carbon-to-nickel ratio as a function of time is, as expected based on TPHs in figure 6.1 and figure 6.2, lower at 225 °C compared to 270°C and 300 °C methanation conditions. The trend of the carbon-to-nickel surface versus TOS for 270 °C methanation appears similar to the 300 °C methanation. For the TPH following 225 °C methanation more data points would be required to discuss the trend, but it is clear that carbon is formed significantly slower during methanation at 225 °C compared to both methanation at 270 °C and 300 °C. So although 270 °C and 225 °C experiments had similar initial CO conversion, significantly less carbon versus time was built up on the surface for the 225 °C methanation. Thus, it is interesting to discuss the activity loss.

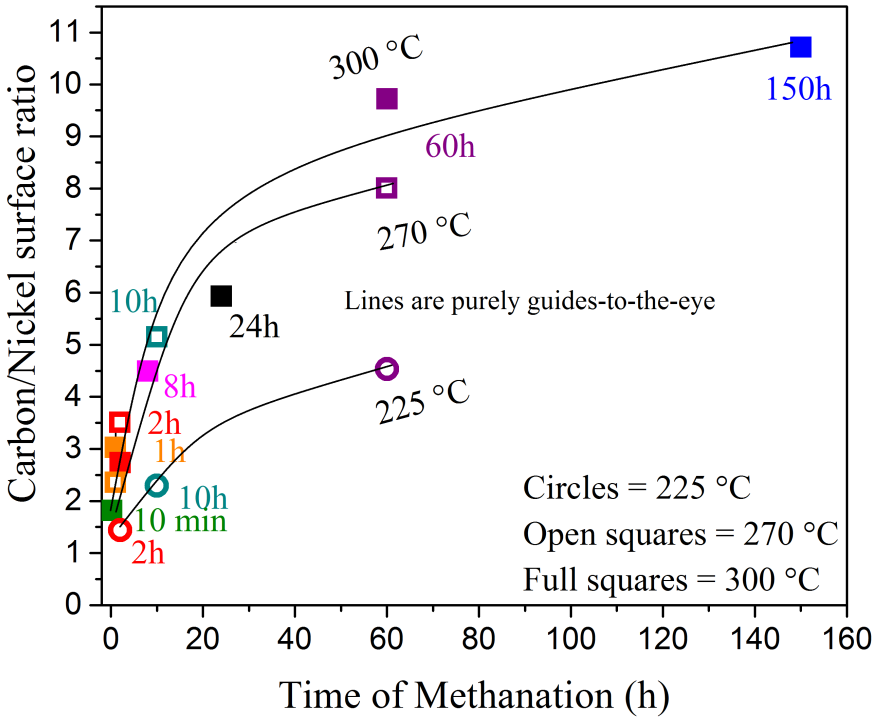

Figure 6.3: The total deposited carbon-to-nickel surface ratio as a function of time on stream for 300 °C (solid squares), 270 °C (open squares), and 225 °C (open circles) methanation. Lines have been drawn to guide the eye. Carbon values for 225 °C have been divided by six because six times as much catalyst was loaded for these experiments compared to the 12.5 mg catalyst loaded in the 270 °C and 300 °C methanation experiments.

In figure 6.4 instead of relating the carbon-to-nickel surface ratio to duration of methanation, the C/Ni_{surf} is related to the activity loss during the respective methanation.

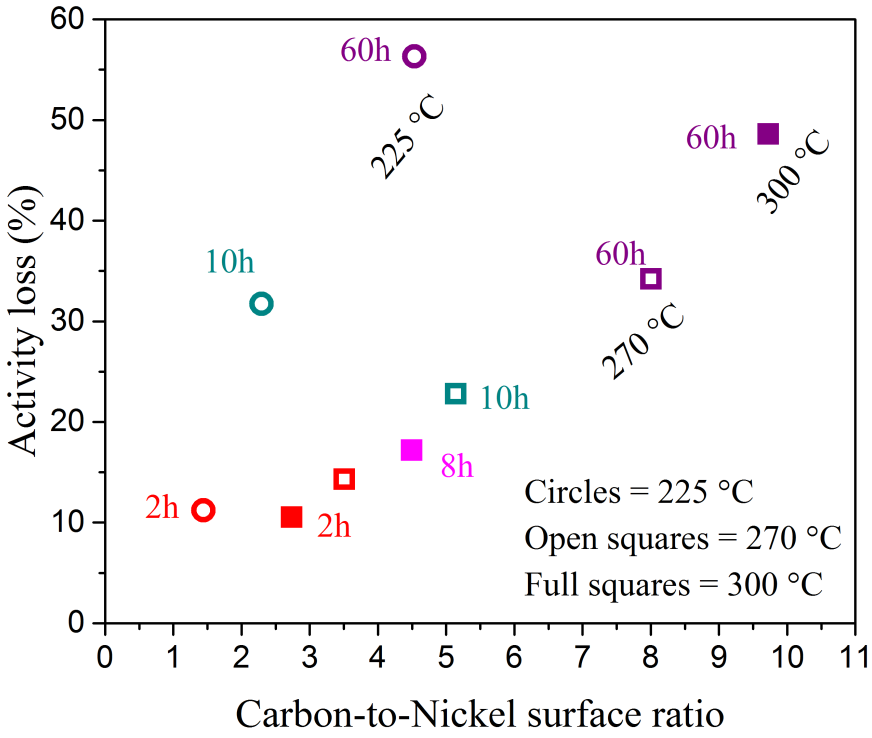

Figure 6.4: The activity loss during methanation and the total deposited carbon-to-nickel surface ratio for 300 °C (solid squares), 270 °C (open squares), and 225 °C (open circles) methanation. Carbon values for 225 °C have been divided by six because six times as much catalyst was loaded for these experiments.

Again, the 270 °C and 300 °C methanation carbon types appear to be similar as activity lost as a function of the C/Ni_{surf} fall on the same linear relation i.e. similar amounts of carbon result in similar activity loss. The results of 270 °C methanation are nicely consistent with conclusions about the deactivating carbon species so far. After 60 hour methanation at 270 °C less deactivation was evident compared to after 60 hour methanation at the 300 °C and showed less of the 500 °C TPH peak as seen by a combination of figure 6.1, 6.3, and 6.4. It is interesting how the 225 °C methanations contain less carbon at similar methanation duration compared to 270 °C and 300 °C methanation but are still significantly more deactivated. Based on the new peaks at ~250 °C and 300 °C, it could appear that more oxygenates were adsorbed at methanation at 225 °C as compared to methanation at 300 °C which could suggest oxygenates also contribute to the deactivation. Contrary to these findings, Kistamurthy et al [96] found that the cobalt catalyst did not deactivate for Fischer-Tropsch synthesis due to oxygenates. Thus, something else might be at play than oxygenates in the 225 °C methanation experiments such as new types of deactivating hydrocarbon species with TPH peaks in this region. This matches that the TPH peaks in figure 6.2 for methanation at 225 °C could look like they

are more than one peak. It is clear though that the carbon types are very different compared to 270 °C and 300 °C methanation. It would be interesting to analyse a 60 hour methanation at 225 °C sample by e.g. electron microscopy. All the above data point to the 270 °C methanation being a similar system to that of the 300 °C methanation, whereas the 225 °C methanation is significantly different with new surface carbon species.

6.2 Effect of Ni Particle Size and Pressure on Surface Carbon

The catalyst has been the same for all types of measurements in the previous experiments. A couple of experiments were done with an aged catalyst with reportedly 40 nm nickel particle size (as opposed to the roughly 11 nm nickel particles so far) in order to judge any dependence on particle size for the carbon species. The experimental procedure was identical to the other methanation experiments except since lower activity was expected almost three times the amount of catalyst was loaded.
In figure 6.5 the TPH curves from figure 4.2 have been plotted together with TPHs succeeding 2 and 8 hour methanation with the aged catalyst.

The most noticeable difference is the carbide and dissolved carbon peak (∼200 °C) which is significantly less intense. It could be explained by a significantly smaller total nickel surface area due to the larger nickel particles. However, only a factor of four lower nickel surface area per gram catalyst was expected using the same approximation as in chapter 3. Considering three times more of aged catalyst was loaded, the carbide and dissolved carbon peaks were therefore still surprisingly low when comparing to TPHs after methanation at 270 °C and 300 °C for the standard catalyst. The 400 °C and 500 °C TPH peaks are broader and less intense for the catalyst with larger particles but these TPH peaks seem to belong to the same carbon species as their peak maxima have not shifted. Thus, particle size does not seem to have a big influence the specific carbon types but rather quantity of the carbon species and the balance between the different species. Gao et al. [112] reported that less carbon was formed during methanation on nickel catalysts with particle size of 10–20 nm as opposed to both nickel α-alumina catalysts with particle size of 5-10 nm and 20-35 nm.
Virtually no characterisation apart from size analysis however, was included and therefore it is difficult to relate their results to this work. At a glance it does not appear that their findings match the results in this work well as significantly less carbon was not deposited on the 11 nm nickel particle catalyst as opposed to the 40 nm nickel particle catalyst. The experimental conditions were different which may affect the results but equally support effects cannot be excluded, e.g. Barrientos et al. [113] reported large differences in both carbon deposition and sintering on α- and γ-alumina as well as silica and titania. For two γ-alumina catalysts Barrientos et al. reported that larger nickel particles (14 nm versus 10 nm) resulted in

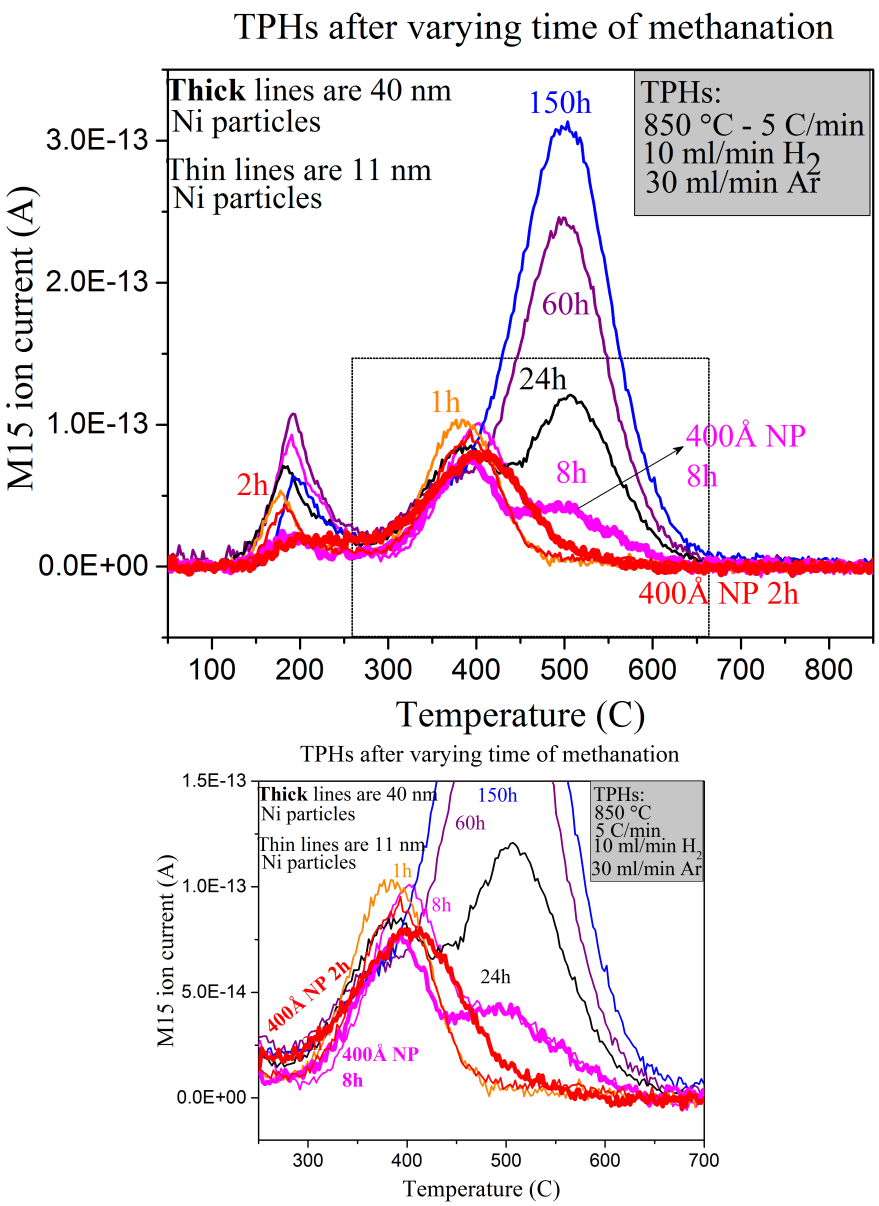

Figure 6.5: Methane signal ($m/z = 15$) during TPH subsequent methanation of various duration as a function of temperature for both ∼11 nm nanoparticles (thin lines) and 40 nm particles (thick lines). Flow of 10 ml/min H_2 and 30 ml/min Ar and ramping with 5 °C/min. An individually determined constant background level has been subtracted from each graph.

more surface carbon during methanation. However, as the high temperature peak at 500 °C peak in figure 6.5 remained unchanged and no new peaks appeared,

this does not appear to be in play during our methanation experiments. Since the 2 hour for 400 Å TPH curve is broader at the 400 °C peak it could rather be a sign of a slightly faster transformation from 400 °C carbon to 500 °C carbon especially considering that the 8 hour TPH curves for 40 nm versus 11 nm show a smaller and narrower 400 °C peak but similar 500 °C peak. It could appear that larger particles lead to more of the structured carbon at 500 °C which is in good agreement with polymerisation of carbon taking place on terrace sites [56]. In the pursuit of understanding the particle size effect in FTS, Den Breejen et al. [111] found that on cobalt particles terrace sites show lower turnover frequency because of slower hydrogenation of CH* and/or poorer CO dissociation. However, in that study the size effect was mostly observed for Co particles below 6 nm.
It seems that small particles are preferable in order to limit carbon formation as less high temperature carbon may be formed and thus less deactivation may be expected.

Preliminary results on the effect of total pressure are presented in the following. In figure 6.6 TPH curves are shown following methanation experiments at 300 °C and total pressure of 3 bar (pCO = 0.3 bar), 6 bar (pCO = 0.6 bar), and 12 bar (pCO = 1.2 bar) for the standard catalyst.
In figure 6.7 TPH curves are shown following methanation experiments at 300 °C and total pressure of 3 bar or higher for either the standard catalyst of ∼11 nm or an aged catalyst with 40 nm nickel particles.
In figure 6.6 all methane desorption curves are from experiments done with an average particle size of 11 nm but with methanation at either 3, 6 or 12 bar. It seems total pressure or higher partial pressure of CO primarily accelerated the formation of the 500 °C carbon.

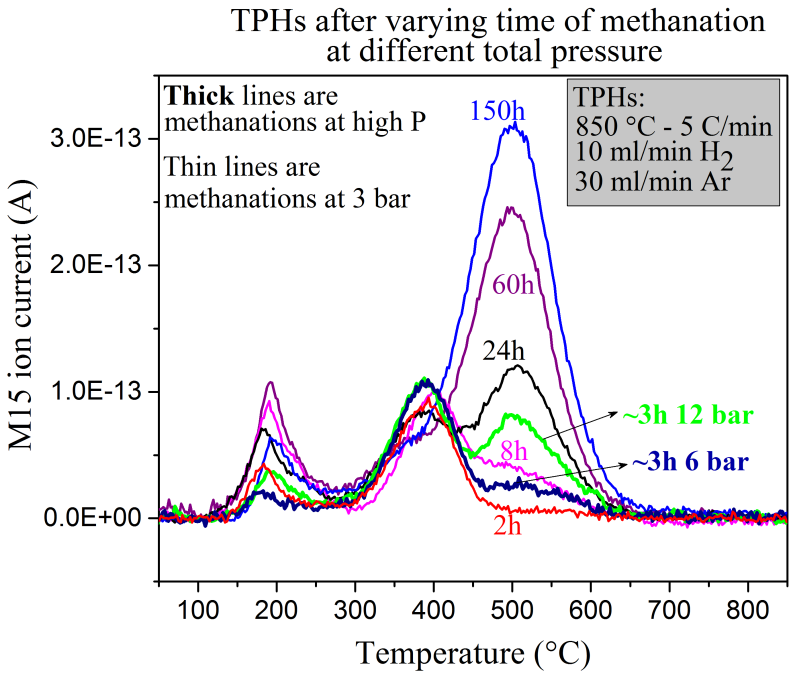

Figure 6.6: Methane signal (m/z = 15) during TPH subsequent methanation at 300 °C and 3 bar (thin lines) or elevated pressure (thick lines) with 1:4 CO-to-H_2 ratio.

A similar conclusion can be drawn from the curves in figure 6.7 where the two TPH curves after 8 hour methanation performed on the catalyst of 40 nm nickel particles at 3 bar and 8 bar respectively and the ∼500 °C peak is greatly intensified. It also appeared that higher pressure reduced the 200 °C TPH peak as seen from figure 6.6 and figure 6.7 which could be due to the shutdown procedure. It took longer to reduce the pressure to atmosphere from higher pressure and thus, the 200 °C TPH peak was reduced. However, it is clear that the higher temperature peaks were not affected as the 400 °C TPH peaks were very similar no matter the pressure during methanation, whereas the formation of 500 °C TPH peak carbon was accelerated. Mirodatos et al. [41,42] similarly concluded that the low temperature carbon species were not affected by increased total pressure and they reported that only the high temperature species were CO pressure dependent.

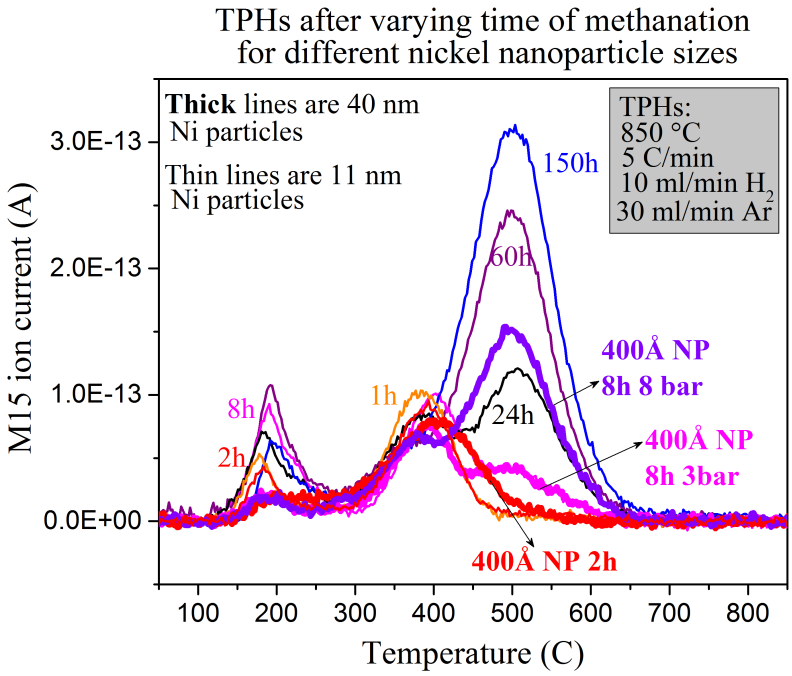

Figure 6.7: TPH curves after methanation at 300 ° C and 3 bar with 11 nm particles (thin lines) or either 3 or 8 bar for 40 nm particles (thick lines).

In combination with the short methanation runs at 300 °C in figure 4.2 which had no 500 °C, it can be concluded that the shutdown procedure does not affect the high temperature TPH peaks strengthening conclusions on the 400 °C and 500 °C TPH carbon made in this work.

6.3 Conclusions on Methanation Conditions

Carbon formed during methanation at 270 °C and 300 °C was very similar both in effect on activity and chemistry as judged by peak shapes and peak positions in TPHs. On the other hand TPH following methanation at 225 °C showed new peaks and the catalyst deactivated faster. Increasing the nickel particle size from ∼11 nm to ∼ 40 nm effected primarily the low temperature carbon whereas a high total pressure accelerated the formation of the 500 °C TPH peak carbon.

7

Nitrogen Adsorption Experiments

Steps have been established to be the most active sites for methanation [53], and it has been reported that graphite nucleation occurs at the steps [54]. Therefore, it would it highly interesting to probe these step sites of the nickel catalyst. Ammonia has been found to deactivate cobalt catalysts in Fischer Tropsch synthesis [114] and Kizilkaya et al. [114] found that the deactivation by ammonia was most likely through adsorption of NH_x species through a study on Co(0001). Kizilkaya studied the difference between a flat cobalt surface, Co(0001), and a stepped cobalt surface, Co(211) and found that NH_3 decomposed on the step sites which were then blocked by NH_2[115]. It was therefore decided to attempt ammonia adsorption at temperatures sufficiently high to decompose NH_3 but at temperatures lower than N_2 desorption which according to measurements by Chorkendorff et al.[116] meant staying below 427 °C. The temperature at which ammonia decomposition is achieved depends on the catalyst's activity towards ammonia decomposition. Simonsen et al. [117] started tests of ammonia decomposition on nickel catalysts from 400 °C but already had significant activity at this temperature depending experimental conditions such as metal weight percent, support etc.
Various experiments of exposing the catalyst to ammonia varying concentration and temperature were attempted without much success. Due to lack of time and prioritising measurements, the attempts were abandoned before good results were achieved.

8 Conclusion and Outlook

8.1 Conclusion

The work was carried out on a nickel alumina catalyst and the deactivating carbon formed during low temperature CO methanation was studied. Much time and effort were initially spent building up the setup and establishing good experimental procedures. As it has been well established that sulfur affects the deactivation behaviour and carbon formation, it was necessary to establish that experiments were unaffected by sulfur. By a combination of activity measurements on the nickel catalyst and surface adsorption measurements on nickel foils analysed by ISS and XPS, it was confirmed that the influence of sulfur in the experiments was negligible. Equally, catalyst deactivation through carbon formation was studied as opposed to through sintering as confirmed by regeneration of the catalyst with temperature programmed hydrogenation (TPH). The catalyst was deactivated during methanation at 300 °C and at 3 bar (pCO = 0.3 bar & H_2/CO = 4) due to carbon formation. In fact, the carbon amount building up on the nickel catalyst was increasing with time on stream and linearly related to the deactivation. Carbon formation involved different carbon species building up on the catalyst distinguished by different peak temperatures during TPH as has been reported by other groups as well. Four different carbon species were evident by Gaussian peak fitting of TPHs curves yielding four methane desorption peaks: ∼185 °C, ∼215 °C, ∼400 °C, and ∼500 °C. It was clear that the formation kinetics of these different carbon species were different as they built up with varying time scales; the carbon of the ∼185 °C, ∼215 °C, and ∼400 °C TPH peaks appearing immediately and the ∼500 °C species appearing only after a few hours of methanation. Other groups have also reported multiple carbon species with different formation kinetics and effects on activity. However, the linearity of the deactivation with carbon quantity was a novel discovery and it was determined by relating peak fitting with activity loss to essentially stem from the 500 °C TPH peak carbon species which were the main deactivating species at long methanation runs. A clear interdependence between the 400 °C TPH peak carbon species and 500 °C TPH peak carbon species

was evident through the TPH peak shape and intensity changes happening with methanation duration. Equally, the deactivation through the 500 °C TPH peak carbon species seemed to be initiated by the 400 °C TPH peak carbon species. It follows that the 400 °C TPH peak carbon species were most likely a precursor of the 500 °C TPH peak carbon species and the two carbon types were like closely related in structure.

In the attempt to discuss the extent of hydrogenation of the carbon species, Ar TPDs were performed. This method of determining the hydrogenation of the carbon was neither based on nor inspired by reported results and also proved not to be straightforward to analyse. The amount of hydrogen exceeded what could reasonably be expected for the surface carbon. However, by relation of the carbon in the 400 °C TPH peak and the sharp hydrogen desorption peak during Ar TPDs, it was suggested that this medium temperature carbon could be hydrogenated. Based on the carbon growth theories on both nickel and cobalt, it is not unreasonable that some of the species are hydrogenated. The 400 °C TPH peak carbon was likely a hydrogenated precursor to the more well-structured species desorbing at 500 °C in the TPHs. Although the 500 °C TPH peak carbon was the main cause for deactivation at longer methanation durations, a remarkably high activity remained after hundred hours of methanation despite carbon amounts equivalent to as much as an average of four graphene monolayers. This suggested that carbon was neither selectively deposited nor uniformly covering the nickel step sites. Thus, both characterisation and activity data pointed towards conversion of hydrogenated defect cyclic polymerised species to defect graphite-like carbon in good agreement with findings in literature. The carbon species reacted off at 185 °C and 215 °C in TPHs following methanation experiments were determined to be surface carbide and dissolved carbon in nickel. This was based on XRD measurements that for CH_4 and CO adsorption measurement samples as well as methanation experiment samples showed a shift in nickel lattice parameter.

Unexpectedly no carbon structures were observed in transmission electron microscopy (TEM), possibly due to such a non-uniform and highly inhomogeneous carbon deposition. By scanning transmission electron microscopy (STEM) energy-dispersive spectroscopy (EDS) carbon was tentatively suggested to be concentrated at the nickel particles but analysis also suggested inhomogeneous carbon deposition over the nickel particle surfaces.

Through the published literature, it was clear that experimental conditions are hugely important for the carbon formation. It was found here that lowering the temperature of methanation had only a small effect in the carbon species for a 30 degree lowering to 270 °C whereas performing methanation at 225 °C significantly changed the carbon type distribution according to TPH results that followed these methanation measurements. However, performing methanation at higher pressure but keeping other conditions similar to the original, showed similar carbon species but an acceleration in the formation of the 500 °C TPH peak carbon species. Nickel particle size seemed to affect primarily the balance and quantities of carbide and dissolved carbon species.

8.2 Outlook

As much time was spent building up the setup and establishing experimental procedures, the results were produced primarily towards the end of this Ph.D. project. Thus, a solid foundation for more experiments has been established. The work amounted to further knowledge into carbon species types, alluded to an inhomogeneous coverage of the catalyst surface and contributed to the experimental conditions dependence discussion. Especially three things remain to properly end the discussion of the results produced in this Ph.D. As the carbon responsible for the high temperature TPH peaks amounted to relatively large amounts and it is expected to be quite well-structured, it should be possible to visualise it e.g. in HRTEM. High pressure STM in combination with TPH could also provide excellent insights into the structured carbon species. The analysis on what was assigned as dissolved carbon seemed to be possible to refine further both through a more detailed and thorough full profile analysis as well as performing in-situ XRD measurements. Also it would be highly interesting to attempt to react off the three lowest TPH peak carbon species formed during methanation and thus, have the catalyst covered by only the 500 °C TPH carbon species and see no or little regained activity afterwards. Ultimately, naturally the goal must be to gain sufficient knowledge to design catalysts and experimental conditions that inhibit the deactivating carbon. A transformation of carbon species into more deactivating carbon species was observed, and it seems this process may be slowed down by optimum low temperature. Although it was seen that the deactivating carbon forms in patches and leave active sites free for methanation, it seems industry will not lower the process temperature as of yet.

Bibliography

[1] P. Sabatier and J. B. Senderens, "Nouvelles synthèses du méthane," *C. R. Hebd. Seances Acad. Sci.*, vol. 134, pp. 514–516, 1902.

[2] K. Pedersen, A. Skov, and J. R. Rostrup-Nielsen, "Catalytic Aspects of High Temperature Methanation," *Prepr Pap Am Chem, Div Fuel Chem*, vol. 25, no. 2, pp. 89–100, 1980.

[3] T. Wind, H. Falsig, J. Sehested, P. G. Moses, and T. T. M. Nguyen, "Comparison of Mechanistic Understanding and Experiments for CO Methanation over Nickel," *J. Catal.*, vol. 342, pp. 105–116, 2016.

[4] R. Chang, *General Chemistry - The Essential Concepts*. New York: McGraw-Hill, 5th ed., 2008.

[5] "http://spaceflight.esa.int/impress/text/education/Catalysis/index.html."

[6] I. Chorkendorff and J. W. Niemantsverdriet, *Concepts of Modern Catalysis and Kinetics*. Weinheim: Wiley-VCH Verlag GmbH & Co. KGaA, 2nd ed., 2003.

[7] T. Bligaard, J. K. Nørskov, S. Dahl, J. Matthiesen, C. H. Christensen, and J. Sehested, "The Brønsted-Evans-Polanyi Relation and the Volcano Curve in Heterogeneous Catalysis," *J. Catal.*, vol. 224, no. 1, pp. 206–217, 2004.

[8] M. A. Vannice, "The Catalytic Synthesis of Hydrocarbons from H2/CO Mixtures over the Group VIII Metals I. The Specific Activities and Product Distributions of Supported Metals," *J. Catal.*, vol. 37, pp. 449–461, 1975.

[9] S. B. Vendelbo, M. Johansson, J. H. Nielsen, and I. Chorkendorff, "Is the Methanation Reaction over Ru Single Crystals Structure Dependent?," *Phys. Chem. Chem. Phys.*, vol. 13, no. 10, pp. 4486–4493, 2011.

[10] G. W. Bridger and C. Woodward, "Formulation and Operation of Methanation Catalysts," *Am. Chem. Soc., Div. Fuel Chem.*, vol. 19, no. 3, pp. 105–116, 1974.

[11] I. Alstrup, "On the Kinetics of CO Methanation on Nickel Surfaces," *J. Catal.*, vol. 151, pp. 216–255, 1995.

[12] "Http://blog.topsoe.com/worlds-largest-sng-plant-goes-stream-china-catalysts-and-process-technology-haldor-topsoe,"

[13] J. Kopyscinski, T. J. Schildhauer, and S. M. A. Biollaz, "Production of Synthetic Natural Gas (SNG) from Coal and Dry Biomass – A Technology Review from 1950 to 2009," *Fuel*, vol. 89, no. 8, pp. 1763–1783, 2010.

[14] J. Gao, Q. Liu, F. Gu, B. Liu, Z. Zhong, and F. Su, "Recent Advances in Methanation Catalysts for the Production of Synthetic Natural Gas," *RSC Adv.*, vol. 5, no. 29, pp. 22759–22776, 2015.

[15] R. Felder and R. Dones, "Evaluation of Ecological Impacts of Synthetic Natural Gas from Wood Used in Current Heating and Car Systems," *Biomass and Bioenergy*, vol. 31, pp. 403–415, jun 2007.

[16] Http://www.bp.com/, "Statistical Review 2016."

[17] S. Ma, Y. Tan, and Y. Han, "Methanation of Syngas over Coral Reef-like Ni/Al2O3 Catalysts," *J. Nat. Gas Chem.*, vol. 20, no. 4, pp. 435–440, 2011.

[18] Http://www.fueleconomy.gov/feg/bifueltech.shtml, "Fuel Economy."

[19] Http://www.afdc.energy.gov/vehicles/natural_gas.html, "Natural Gas Vehicles."

[20] P. Kazempoor and R. J. Braun, "Hydrogen and Synthetic Fuel Production Using High Temperature Solid Oxide Electrolysis Cells (SOECs)," *Int. J. Hydrog. Energy*, vol. 40, no. 9, pp. 3599–3612, 2015.

[21] M. Götz, J. Lefebvre, F. Mörs, A. McDaniel Koch, F. Graf, S. Bajohr, R. Reimert, and T. Kolb, "Renewable Power-to-Gas: A Technological and Economic Review," *Renew. Energy*, vol. 85, pp. 1371–1390, 2016.

[22] NREL, "A Comparison of Hydrogen and Propane Fuels," *DOE/GO-102009-2813*, 2009.

[23] M. A. A. Aziz, A. A. Jalil, S. Triwahyono, and A. Ahmad, "CO2 Methanation over Heterogeneous Catalysts: Recent Progress and Future Prospects," *Green Chem.*, vol. 17, no. 5, pp. 2647–2663, 2015.

[24] R. Winkler-Goldstein and A. Rastetter, "Power to gas: The Final Breakthrough for the Hydrogen Economy?," *Green*, vol. 3, no. 1, pp. 69–78, 2013.

[25] C. Park, R. Sedundo, V. Knazkins, and P. Korbakorba, "Feasibility Analysis of the Power-to-Gas Concept in the Future Swiss Power System," in *CIRED Work. 2016*, no. June, pp. 1–5, 2016.

[26] "Power to Gas - Http://www.europeanpowertogas.com/about/power-to-gas."

[27] P. F. Tropschuh and E. Pham, "Audi Future Energies: Balancing Business and Environmental Concerns," in *Sustain. Automot. Technol. 2013* (J. Wellnitz, A. Subic, and R. Trufin, eds.), Lecture Notes in Mobility, pp. 185–190, Springer International Publishing, 2014.

[28] J. B. Hansen, M. Holstebroe, U. M. B. Jensen, J. Rass-Hansen, and T. Heiredal-Clausen, "SOEC Enabled Biogas Upgrading," *12th Eur. SOFC SOE Forum 2016*, no. July, pp. 1–10, 2016.

[29] Y. Hori, K. Kikuchi, and S. Suzuki, "Production of CO and CH4 in Electrochemical Reduction of CO2 at Metal Electrodes in Aqueous Hydrogencarbonate Solution," *Chem. Lett.*, pp. 1695–1698, 1985.

[30] M. Gattrell, N. Gupta, and A. Co, "A review of the Aqueous Electrochemical Reduction of CO2 to Hydrocarbons at Copper," *J. Electroanal. Chem.*, vol. 594, no. 1, pp. 1–19, 2006.

[31] K. P. Kuhl, E. Cave, D. N. Abram, and T. F. Jaramillo, "New Insights into the Electrochemical Reduction of Carbon Dioxide on Metallic Copper Surfaces," *Energy Environ. Sci.*, vol. 5, no. 5, pp. 7050–7059, 2012.

[32] C. H. Bartholomew, R. B. Pannell, and R. W. Fowler, "Sintering of Alumina-Supported Nickel and Nickel Bimetallic Methanation Catalysts in H2/H2O Atmospheres," *J. Catal.*, vol. 79, no. 1, pp. 34–46, 1983.

[33] J. R. Rostrup-Nielsen, K. Pedersen, and J. Sehested, "High Temperature Methanation Sintering and Structure Sensitivity," *Appl. Catal., A*, vol. 330, pp. 134–138, oct 2007.

[34] T. T. M. Nguyen, L. Wissing, and M. Skjøth-Rasmussen, "High Temperature Methanation: Catalyst Considerations," *Catal. Today*, vol. 215, pp. 233–238, 2013.

[35] H. H. Gierlich, M. Fremery, A. Skov, and J. R. Rostrup-Nielsen, "Deactivation Phenomena of a Ni-based Catalyst for High Temperature Methanation," *Stud. Surf. Sci. Catal.*, vol. 6, pp. 459–469, 1980.

[36] C. H. Bartholomew, "Carbon Deposition in Steam Reforming and Methanation," *Catal. Rev. - Sci. Eng.*, vol. 24, pp. 67–112, jan 1982.

[37] C. H. Bartholomew, "Mechanisms of Catalyst Deactivation," *Appl. Catal. A Gen.*, vol. 212, pp. 17–60, apr 2001.

[38] M. D. Argyle and C. H. Bartholomew, "Heterogeneous Catalyst Deactivation and Regeneration: A Review," *Catalysts*, vol. 5, no. 1, pp. 145–269, 2015.

[39] J. G. McCarty and H. Wise, "Hydrogenation of Surface Carbon on Alumina-Supported Nickel," *J. Catal.*, vol. 57, pp. 406–416, may 1979.

[40] P. K. Agrawal, W. D. Fitzharris, and J. R. Katzer, "Sulfur Poisoning and Carbon Deactivation of Alumina-supported Ni, Co, Fe, and Ru Catalysts in CO Hydrogenation," *Catal. Deactiv.*, pp. 179–200, 1980.

[41] C. Mirodatos, J. A. Dalmon, and G. A. Martin, "Nature and Role of Carbon Species During CO and CO-H2 Reactions over Ni/SiO2 Catalysts," *Catal. Energy Scene*, pp. 505–512, 1984.

[42] C. Mirodatos, H. Praliaud, and M. Primet, "Deactivation of Nickel-based Catalysts during CO Methanation and Disproportionation," *J. Catal.*, vol. 107, pp. 275–287, oct 1987.

[43] R. E. Hayes, W. J. Thomas, and K. E. Hayes, "A Study of the Nickel-Catalyzed Methanation Reaction," *J. Catal.*, vol. 92, pp. 312–326, 1985.

[44] R. E. Hayes and K. J. Ward, "The Nature of Surface Carbon on y-Alumina Supported Nickel Catalysts During CO-Disproportionation in the Presence and Absence of Hydrogen," *Appl. Catal.*, vol. 20, pp. 123–131, 1986.

[45] E. J. Erekson and C. H. Bartholomew, "Sulfur Poisoning of Nickel Methanation Catalysts II. Effects of H2S Concentration, CO and H2O Partial Pressures and Temperature on Deactivation Rates," *Appl. Catal.*, vol. 5, pp. 323–336, 1983.

[46] C. H. Bartholomew, G. D. Weatherbee, and G. A. Jarvi, "Effects of Carbon Deposits on the Specific Activity of Nickel and Nickel Bimetallic Catalysts," *Chem. Eng. Commun.*, vol. 5, pp. 125–134, 1980.

[47] R. M. Bowman and C. H. Bartholomew, "Deactivation by Carbon on Ru/Al2O3 during CO Hydrogenation," *Appl. Catal.*, vol. 7, pp. 179–187, 1983.

[48] J. R. Rostrup-Nielsen and J. Sehested, "Whisker Carbon Revisited," in *Catal. Deactiv. 2001 Proc. 9th Int. Symp.* (G. W. R. J.J. Spivey and B. H. Davis, eds.), vol. 139 of *Studies in Surface Science and Catalysis*, pp. 1–12, Elsevier, 2001.

[49] J. Sehested, "Four Challenges for Nickel Steam-Reforming Catalysts," *Catal. Today*, vol. 111, no. 1-2, pp. 103–110, 2006.

[50] T. E. Madey, D. W. Goodman, and R. D. Kelley, "Abstract: Surface Science and Catalysis: The Catalytic Methanation Reaction," *J. Vac. Sci. Technol.*, vol. 16, no. 2, pp. 433–434, 1978.

[51] R. D. Kelley and D. W. Goodman, "Catalytic Methanation over Single Crystal Nickel and Ruthenium: Reaction Kinetics on Different Crystal Planes and the Correlation of Surface Carbide Concentration with Reaction Rate," *Surf. Sci. Lett.*, vol. 123, pp. 743–749, 1982.

[52] J. Engbæk, O. Lytken, J. H. Nielsen, and I. Chorkendorff, "CO Dissociation on Ni: The Effect of Steps and of Nickel Carbonyl," *Surf. Sci.*, vol. 602, pp. 733–743, feb 2008.

[53] M. P. Andersson, F. Abild-Pedersen, I. Remediakis, T. Bligaard, G. Jones, J. Engbæk, O. Lytken, S. Horch, J. H. Nielsen, J. Sehested, J. R. Rostrup-Nielsen, J. K. Nørskov, and I. Chorkendorff, "Structure Sensitivity of the Methanation Reaction: H2-Induced CO Dissociation on Nickel Surfaces," *J. Catal.*, vol. 255, pp. 6–19, apr 2008.

[54] H. S. Bengaard, J. K. Nørskov, J. Sehested, B. S. Clausen, L. P. Nielsen, A. M. Molenbroek, M. Carlo, and J. R. Rostrup-Nielsen, "Steam Reforming and Graphite Formation on Ni Catalysts," *J. Catal.*, vol. 209, pp. 365–384, jul 2002.

[55] Q. Y. Yang, K. J. Maynard, A. D. Johnson, and S. T. Ceyer, "The Structure and Chemistry of CH3 and CH Radicals Adsorbed on Ni(111)," *J. Chem. Phys.*, vol. 102, no. 19, pp. 7734–7749, 1995.

[56] C. J. Weststrate, A. C. Kazalkaya, E. T. R. Rossen, M. W. G. M. Verhoeven, I. M. Ciobîca, A. M. Saib, and J. W. Niemantsverdriet, "Atomic and Polymeric Carbon on Co(0001): Surface Reconstruction, Graphene Formation, and Catalyst Poisoning," *J. Phys. Chem. C*, vol. 116, no. 21, pp. 11575–11583, 2012.

[57] A. M. Saib, D. J. Moodley, I. M. Ciobîca, M. M. Hauman, B. H. Sigwebela, C. J. Weststrate, J. W. Niemantsverdriet, and J. Van De Loosdrecht, "Fundamental Understanding of Deactivation and Regeneration of Cobalt Fischer-Tropsch Synthesis Catalysts," *Catal. Today*, vol. 154, no. 3-4, pp. 271–282, 2010.

[58] F. Steinbach, J. Kiss, and R. Krall, "Identification and Stability of CH3, CH2, and CH Species on Co and Ni Surfaces, a Pes Investigation," *Surf. Sci.*, vol. 157, no. 2-3, pp. 401–412, 1985.

[59] K. Fei Tan, J. Xu, J. Chang, A. Borgna, M. Saeys, K. F. Tan, J. Xu, J. Chang, A. Borgna, M. Saeys, K. Fei Tan, J. Xu, J. Chang, A. Borgna, M. Saeys, K. F. Tan, J. Xu, J. Chang, A. Borgna, and M. Saeys, "Carbon Deposition on Co Catalysts during Fischer-Tropsch Synthesis: A Computational and Experimental Study," *J. Catal.*, vol. 274, pp. 121–129, sep 2010.

[60] D. J. Moodley, J. van de Loosdrecht, A. M. Saib, M. J. Overett, A. K. Datye, and J. W. Niemantsverdriet, "Carbon Deposition as a Deactivation Mechanism of Cobalt-Based Fischer-Tropsch Synthesis Catalysts under Realistic Conditions," *Appl. Catal. A Gen.*, vol. 354, no. 1-2, pp. 102–110, 2009.

[61] K. Keyvanloo, M. J. Fisher, W. C. Hecker, R. J. Lancee, G. Jacobs, and C. H. Bartholomew, "Kinetics of Deactivation by Carbon of a Cobalt Fischer–Tropsch Catalyst: Effects of CO and H2 Partial Pressures," *J. Catal.*, vol. 327, pp. 33–47, jul 2015.

[62] C. J. Weststrate, I. M. Ciobîca, A. M. Saib, D. J. Moodley, and J. W. Niemantsverdriet, "Fundamental Issues on Practical Fischer-Tropsch Catalysts: How Surface Science Can Help," *Catal. Today*, vol. 228, pp. 106–112, 2014.

[63] C. J. Weststrate, P. van Helden, and J. W. Niemantsverdriet, "Reflections on the Fischer-Tropsch Synthesis: Mechanistic Issues from a Surface Science Perspective," *Catal. Today*, vol. 275, pp. 100–110, 2016.

[64] P. W. Wentrcek, J. G. McCarty, C. M. Ablow, and H. Wise, "Deactivation of Alumina-Supported Nickel and Ruthenium Catalysts by Sulfur Compounds," *J. Catal.*, vol. 61, no. 1, pp. 232–241, 1980.

[65] C. H. Bartholomew, G. D. Weatherbee, and G. A. Jarvi, "Sulfur Poisoning of Nickel Methanation Catalysts I. In situ Deactivation of H2S of Nickel and Nickel Bimetallics," *J. Catal.*, vol. 60, pp. 257–269, 1979.

[66] B. Legras, V. V. Ordomsky, C. Dujardin, M. Virginie, and A. Y. Khodakov, "Impact and Detailed Action of Sulfur in Syngas on Methane Synthesis on Ni/γ-Al2O3 Catalyst," *ACS Catal.*, vol. 4, pp. 2785–2791, aug 2014.

[67] B. Kasemo, "Quartz Tube Orifice Leaks for Local, Fast-Response Gas Sampling to Mass Spectrometers," *Rev. Sci. Instrum.*, vol. 50, no. 12, pp. 1602–1604, 1979.

[68] C. G. Hill, *An Introduction to Chemical Engineering Kinetics and Reactor Design*. John Wiley & Sons, Inc., 1977.

[69] Pfeiffer Vacuum GmbH, *Mass spectrometer catalog*. Pfeiffer Vacuum GmbH, pk 0085 pe ed., 2005.

[70] Pfeiffer Vacuum GmbH, "https://www.pfeiffer-vacuum.com/en/know-how/mass-spectrometers-and-residual-gas-analysis/quadrupole-mass-spectrometers-qms/."

[71] NIST, "http://webbook.nist.gov/chemistry/."

[72] "https://en.wikipedia.org/wiki/Gas_chromatography."

[73] D. A. Skoog, J. F. Holler, and S. R. Crouch, *Principles of Instrumental Analysis*. David Harris, sixth ed., 2007.

[74] L. Gerward, *X-Ray Analytical Methods*. 2001.

[75] I. Chorkendorff, "Surface Physics / Chemistry," 2010.

[76] H. H. Brongersma, T. Grehl, E. R. Schofield, R. A. P. Smith, and H. R. J. ter Veen, "Analysis of the Outer Surface of Platinum-Gold Catalysts by Low-Energy Ion Scattering," *Platin. Met. Rev.*, vol. 54, no. 2, pp. 81–87, 2010.

[77] J. R. Rostrup-Nielsen, *Steam Reforming Catalysts : an Investigation of Catalysts for Tubular Steam Reforming of Hydrocarbons*. Teknisk Forlag, 1975.

[78] T. S. Christensen and J. R. Rostrup-Nielsen, "Catalyst Deactivation in Adiabatic Prereforming: Experimental Methods and Models for Prediction of Performance," in *Deactiv. Test. Hydrocarb. Catal.* (P. O'Connor, T. Takatsuka, and G. L. Woolery, eds.), ch. 13, pp. 186–200, American Chemical Society, acs sympos ed., 1996.

[79] A. G. Shard, "Detection Limits in XPS for More than 6000 Binary Systems Using Al and Mg Kα X-rays," *Surf. Interface Anal.*, vol. 46, no. 3, pp. 175–185, 2014.

[80] I. Alstrup, I. Chorkendorff, and S. Ullmann, "Dissociative Chemisorption of CH4 on Ni(100) with Preadsorbed Oxygen," *Surf. Sci.*, vol. 234, pp. 79–86, 1990.

[81] R. A. Dalla Betta, A. G. Piken, and M. Shelef, "Heterogeneous Methanation: Steady-State Rate of CO Hydrogenation on Supported Ruthenium, Nickel and Rhenium," *J. Catal.*, vol. 40, pp. 173–183, nov 1975.

[82] D.-K. Lee, J.-H. Lee, and S.-K. Ihm, "Effect of Carbon Deposits on Carbon Monoxide Hydrogenation over Alumina-Supported Cobalt Catalyst," *Appl. Catal.*, vol. 36, pp. 199–207, 1988.

[83] I. Alstrup, I. Chorkendorff, and S. Ullmann, "Interaction of Hydrogen with Carbidic Carbon on Ni(100)," *Surf. Sci.*, vol. 293, pp. 133–144, 1993.

[84] C. Klink, I. Stensgaard, F. Besenbacher, and E. Lægsgaard, "Carbidic Carbon on Ni(110): an STM Study," *Surf. Sci.*, vol. 360, no. 1-3, pp. 171–179, 1996.

[85] A. A. Bunaciu, E. G. Udriştioiu, and H. Y. Aboul-Enein, "X-Ray Diffraction: Instrumentation and Applications," *Crit. Rev. Anal. Chem.*, vol. 45, pp. 289–299, oct 2015.

[86] G.-A. Martin and B. Imelik, "Adsorption of Hydrocarbons and Various Gases on Ni-SiO2 Catalysts Studied by High Field Magnetic Methods," *Surf. Sci.*, vol. 42, no. 1, pp. 157–172, 1974.

[87] G. A. Martin, M. Primet, and J. A. Dalmon, "Reactions of CO and CO2 on Ni/SiO2 above 373 K as Studied by Infrared Spectroscopic and Magnetic Methods," *J. Catal.*, vol. 53, pp. 321–220, 1978.

[88] D. K. Ludlow and T. S. Cale, "Nickel Crystallite Thermometry during Methanation," *J. Catal.*, vol. 90, pp. 40–48, nov 1984.

[89] L. Znak, Z. Kaszkur, and J. Zieliński, "Evolution of Metal Phase in the Course of CO Hydrogenation on Potassium Promoted Ni/Al2O3 Catalyst," *Catal. Lett.*, vol. 136, no. 1-2, pp. 92–95, 2010.

[90] J. Rouquette, J. Haines, G. Fraysse, A. Al-Zein, V. Bornand, M. Pintard, P. Papet, S. Hull, and F. a. Gorelli, "High-Pressure Structural and Vibrational Study of PbZr0.40Ti0.60O3.," *Inorg. Chem.*, vol. 47, no. 21, pp. 9898–9904, 2008.

[91] Z. Huba and E. Carpenter, "Monitoring the Formation of Carbide Crystal Phases during the Thermal Decomposition of 3d Transition Metal Dicarboxylate Complexes," *Dalt. Trans.*, vol. 43, no. 32, pp. 12236–12242, 2014.

[92] S. Rosen and P. G. Sprang, "Ternary Carbide Phases Formed by Scandium-Group Elements with Aluminum and Carbon," in *Adv. X-Ray Anal.*, pp. 91–102, Boston, MA: Springer US, 1965.

[93] S. Sasaki, K. Fujino, and Y. Takéuchi, "X-Ray Determination of Electron-density Distributions in Oxides, MgO, MnO, CoO, and NiO, and Atomic Scattering Factors of their Constituent Atoms," *Proc. Japan Acad. Ser. B Phys. Biol. Sci.*, vol. 55, no. 2, pp. 43–48, 1979.

[94] E. Konysheva, E. Suard, and J. T. S. Irvine, "Effect of Oxygen Non Stoichiometry and Oxidation State of Transition Elements on High-Temperature Phase Transition in A-Site Deficient La 0.95 Ni 0.6 Fe 0.4 O 3-d Perovskite," *Chem. Mater.*, vol. 21, no. 21, pp. 5307–5318, 2009.

[95] E. G. M. Kuijpers, A. J. H. M. Kock, M. W. C. M. A. Nieuwesteeg, and J. W. Geus, "Disproportionation of CO on Ni/SiO2: Kinetics and Nature of the Deposited Carbon," *J. Catal.*, vol. 95, pp. 13–20, 1985.

[96] D. Kistamurthy, A. M. Saib, D. J. Moodley, H. Preston, I. M. Ciobîca, W. J. van Rensburg, J. W. Niemantsverdriet, and C. J. Weststrate, "The Role of Carboxylic Acid in Cobalt Fischer-Tropsch Synthesis Catalyst Deactivation," *Catal. Today*, vol. 275, pp. 127–134, 2016.

[97] W. Zhao, J. Gebhardt, F. Späth, K. Gotterbarm, C. Gleichweit, H.-P. Steinrück, A. Görling, and C. Papp, "Reversible Hydrogenation of Graphene on Ni(111)-Synthesis of Graphone," *Chem. Eur. J.*, vol. 21, no. 8, pp. 3347–3358, 2015.

[98] L. L. Patera, F. Bianchini, G. Troiano, C. Dri, C. Cepek, M. Peressi, C. Africh, and G. Comelli, "Temperature-Driven Changes of the Graphene Edge Structure on Ni(111): Substrate vs Hydrogen Passivation," *Nano Lett.*, vol. 15, no. 1, pp. 56–62, 2015.

[99] D. Curcio, L. Omiciuolo, M. Pozzo, P. Lacovig, S. Lizzit, N. Jabeen, L. Petaccia, D. Alfè, and A. Baraldi, "Molecular Lifting, Twisting, and Curling during Metal-Assisted Polycyclic Hydrocarbon Dehydrogenation," *J. Am. Chem. Soc.*, vol. 138, no. 10, pp. 3395–3402, 2016.

[100] K. T. Rim, M. Siaj, S. Xiao, M. Myers, V. D. Carpentier, L. Liu, C. Su, M. L. Steigerwald, M. S. Hybertsen, P. H. McBreen, G. W. Flynn, and C. Nuckolls, "Forming Aromatic Hemispheres on Transition-Metal Surfaces," *Angew. Chem. Int. Ed.*, vol. 46, no. 41, pp. 7891–7895, 2007.

[101] S. Günther, S. Dänhardt, and M. Ehrensperger, "A High-Temperature Scanning Tunneling Microscopy Study of the Ordering Transition of an Amorphous Carbon Layer into Graphene on Ru (0001)," *ACS Nano*, vol. 7, no. 1, pp. 154–164, 2012.

[102] J. G. Buijnsters, R. Gago, A. Redondo-Cubero, and I. Jiménez, "Hydrogen Stability in Hydrogenated Amorphous Carbon Films with Polymer-like and Diamond-like Structure," *J. Appl. Phys.*, vol. 112, no. 9, 2012.

[103] S. Peter, M. Günther, and F. Richter, "A Comparative Analysis of a-C:H Films Deposited from Five Hydrocarbons by Thermal Desorption Spectroscopy," *Vacuum*, vol. 86, no. 6, pp. 667–671, 2012.

[104] T. Zecho, A. Güttler, and J. Küppers, "A TDS Study of D Adsorption on Terraces and Terrace Edges of Graphite (0 0 0 1) Surfaces," *Carbon N. Y.*, vol. 42, no. 3, pp. 609–617, 2004.

[105] B. Chen and J. L. Falconer, "Hydrogenation of Organic Oxygenates on Ni/Al2O3 and Ni/SiO2 Catalysts," *J. Catal.*, vol. 147, pp. 72–81, 1994.

[106] D. Brandon and W. D. Kaplan, *Microstructural Characterization of Materials*. 2nd ed., 2008.

[107] S. Helveg, C. López-Cartes, J. Sehested, P. L. Hansen, B. S. Clausen, J. R. Rostrup-Nielsen, F. Abild-Pedersen, and J. K. Nørskov, "Atomic-Scale Imaging of Carbon Nanofibre Growth," *Nature*, vol. 427, pp. 426–429, jan 2004.

[108] A. D. Moeller and C. H. Bartholomew, "Deactivation by Carbon of Nickel, Nickel-Ruthenium, and Nickel-Molybdenum Methanation Catalysts," *Ind. Eng. Chem. Pro. Res. Dev.*, vol. 21, pp. 390–397, sep 1982.

[109] D. Deiana, *Atomic-Level Electron Microscopy of Metal and Alloy Electrocatalysts*. Ph.d. thesis, 2014.

[110] P. Munnik, M. E. Z. Velthoen, P. E. de Jongh, K. P. de Jong, and C. J. Gommes, "Nanoparticle growth in supported nickel catalysts during methanation reaction–larger is better.," *Angew. Chem. Int. Ed. Engl.*, vol. 53, pp. 9493–7, sep 2014.

[111] J. P. den Breejen, P. B. Radstake, G. L. Bezemer, J. H. Bitter, V. Frøseth, A. Holmen, and K. P. de Jong, "On the Origin of the Cobalt Particle Size Effects in Fischer-Tropsch Catalysis," *J. Am. Chem. Soc.*, vol. 131, pp. 7197–7203, may 2009.

[112] J. Gao, C. Jia, M. Zhang, F. Gu, G. Xu, and F. Su, "Effect of nickel nanoparticle size in Ni/α-Al2O3 on CO methanation reaction for the production of synthetic natural gas," *Catal. Sci. Technol.*, vol. 3, no. 8, p. 2009, 2013.

[113] J. Barrientos, M. Lualdi, M. Boutonnet, and S. Järås, "Deactivation of supported nickel catalysts during CO methanation," *Appl. Catal. A Gen.*, vol. 486, pp. 143–149, sep 2014.

[114] A. C. Kizilkaya, J. W. Niemantsverdriet, and C. J. Weststrate, "Ammonia Adsorption and Decomposition on Co(0001) in Relation to Fischer-Tropsch Synthesis," *J. Phys. Chem. C*, vol. 120, no. 7, pp. 3834–3845, 2016.

[115] A. C. Kizilkaya, *Effect of adsorbate interactions on catalytic reactivity : Elementary surface reactions on rhodium and cobalt.* Ph.d. thesis, 2014.

[116] I. Chorkendorff, J. N. Russell, and J. T. Yates, "Surface reaction pathways of methylamine on the Ni(111) surface," *J. Chem. Phys.*, vol. 86, no. 8, p. 4692, 1987.

[117] S. B. Simonsen, D. Chakraborty, I. Chorkendorff, and S. Dahl, "Alloyed Ni-Fe nanoparticles as catalysts for NH3 decomposition," *Appl. Catal. A Gen.*, vol. 447-448, pp. 22–31, 2012.

Paper 1

Published online in the Journal of Physical Chemistry C:
14th of July 2017
DOI: 10.1021/acs.jpcc.7b03754

THE JOURNAL OF PHYSICAL CHEMISTRY C

Article

pubs.acs.org/JPCC

Deactivating Carbon Formation on a Ni/Al_2O_3 Catalyst under Methanation Conditions

Sine E. Olesen,[†] Klas J. Andersson,[‡] Christian Danvad Damsgaard,[⊥,†] and Ib Chorkendorff*[,†]

[†]Department of Physics, Technical University of Denmark, Building 312, 2800 Kgs. Lyngby, Denmark

[‡]Haldor Topsoe A/S, Haldor Topsøes Alle 1, 2800 Kgs. Lyngby, Denmark

[⊥]Center for Electron Nanoscopy (CEN), Technical University of Denmark, Building 307 & 314, 2800 Kgs. Lyngby, Denmark

Supporting Information

ABSTRACT: The carbon formation causing deactivation during CO methanation was studied for a Ni/Al_2O_3 catalyst. Sulfur-free methanation at low temperature (573 K) for various lengths of time was followed by temperature-programmed hydrogenation (TPH) providing information on carbon types involved in the deactivation of the catalyst. Three main carbon hydrogenation peaks were evident from TPHs following methanation: ~460, ~650, and ~775 K. It is suggested that the ~460 K TPH peak was composed of two peaks: a surface carbide peak at 445−460 K, and a peak due to carbon dissolved into the nickel at 485 K based on CO and CH_4 adsorption measurements and XRD analysis. The 650 and 775 K temperature peaks are assigned to polymerized carbon structures and the ~775 K peak was found to be the primary cause of deactivation as judged by a linear correlation between its amount and the degree of catalyst deactivation. The longer the duration of the methanation test, the more carbon was built up on the Ni surfaces and the highest observed amount was quantified to be as much as eight carbon atoms per Ni surface atom (8 C/Ni_{surf}), which would roughly correspond to an average coverage of four monolayers of graphene. From H_2 desorption measurements after reaction the 650 K TPH peak carbon structure is proposed to be partially hydrogenated, possibly resembling polycyclic aromatic-like carbon. The 775 K peak carbon species are likely more graphene-like. Results indicate that although carbon deposition nucleation may be initiated at the most active methanation sites, i.e., the Ni step sites, subsequent growth takes place over Ni terrace sites. A strongly inhomogeneous carbon growth distribution over the Ni nanoparticle surfaces could also account for our findings. Similar to suggestions regarding catalyst deactivation in Fischer−Tropsch synthesis, a surface CH* coupling mechanism is likely taking place, and our results suggest these polymeric hydrocarbon species become more ordered, aromatic, and eventually graphene-like over time.

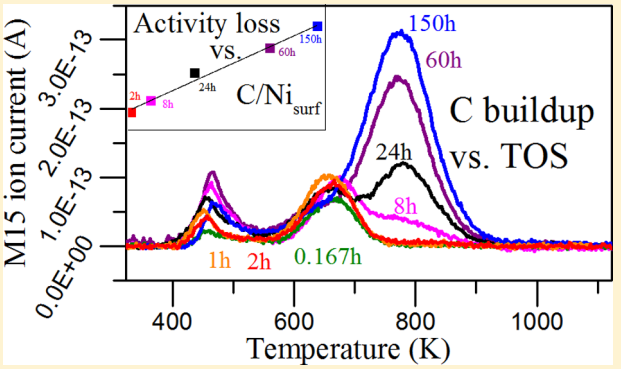

INTRODUCTION

For many years, the methanation reaction has been employed in industry to clean up the hydrogen stream in ammonia synthesis.[1] However, in recent years the interest in the reaction has increased for its applicability in the energy sector. As synthetic natural gas, methane can enter the existing energy infrastructure and be produced through coal, of which reserves are much larger than oil, or more renewably through biomass.[1−3] In the future with intermittent energy sources and plenty of electrolysis hydrogen, the methanation reaction may also be interesting for conversion of hydrogen into synthetic natural gas for the existing infrastructure instead of storing the produced hydrogen[4] since it has a 3.3 higher energy density per volume.[5]

Nickel-based catalysts are preferred in industry[6] and typical deactivation processes are nickel sintering at higher temperatures[6−9] and carbon deposition at lower temperatures.[6,9−11] Whereas Ni sintering and formation of the particular whisker-type carbon are well-studied phenomena,[8,12] much less is known regarding the structure and nature of deactivating carbon formed during low temperature CO methanation. Carbon types on and in Ni which are easily hydrogenated below 573 K, i.e., surface carbide, dissolved carbon, and bulk carbide, have been found not to be deactivating[13,14] beyond the formation of an equilibrium surface carbide coverage.[15] Deactivation has, however, been related to two adsorbed carbon types[13] hydrogenating in the 573−873 K range, with peak hydrogenation rates at about 673 and 773 K, respectively, in temperature-programmed hydrogenation (TPH) spectra.[13,14,16] These deactivating carbon types formed in low-temperature CO methanation differ drastically from the whisker-type carbon formed from CO dissociation at temperatures at and above 573 K in the absence of hydrogen[17,18] and

Received: April 21, 2017
Revised: June 5, 2017
Published: June 14, 2017

DOI: 10.1021/acs.jpcc.7b03754
J. Phys. Chem. C XXXX, XXX, XXX−XXX

in high-temperature CO methanation[18−20] and are not of a wholly graphitic nature.[17]

As Wise et al.[21] reported that sulfur accelerates the conversion of carbidic carbon to graphitic-like carbon and Gierlich et al.[10] found more carbon formed on the catalyst during their pilot scale tests when sulfur was present, it is essential to perform experiments free of sulfur in order to gain more fundamental knowledge on carbon formation during methanation. Therefore, establishing that experiments are sulfur-free is paramount.

McCarty and Wise[22] studied carbon deposited by CO or C_2H_4 on nickel catalysts by its reactivity with hydrogen and named the reactive carbon coming off at low temperature α-carbon and the less reactive β-carbon; α-carbon was assigned to carbidic (atomic) surface carbon and β-carbon to C−C bond polymerized carbon. Bartholomew[11] summarized that carbon formed by CO decomposition below 600 K exists as atomic/carbidic carbon and above 600 K as polymerized carbon. From pilot scale methanation studies, Gierlich et al.[10] suggested that deactivating carbon formation at low temperatures took place through an intermediate of carbidic carbon that polymerized into an encapsulating carbon film covering the active Ni surface but no actual characterization of the type of carbon formed was described. Weststrate et al.[23,24] proposed a chain growth mechanism based on cobalt step site generated surface CH species subsequently diffusing to the terraces where CH−CH coupling takes place, and over time leading to the buildup of condensed structures formed via cyclopolymerization reactions leading to the deactivation of Fischer−Tropsch (FT) activity. This would be in accordance with earlier work by Yang et al.[25] on Ni(111). Studying CH_x species and their stabilities on Ni(111), they found that at elevated temperature (>250 K) CH species dimerize into C_2H_2 which at high local coverages trimerize to benzene. Above 450 K, benzene was found by TPD to partially dehydrogenate and, according to vibrational spectra assignments, subsequently polymerized into large cyclic hydrocarbons.[25]

A number of important questions still remain unanswered regarding the nature of the deactivating carbon formed during low-temperature CO methanation on nickel, for instance with respect to the direct correlation between catalyst deactivation and quantitative surface carbon coverage, as well as whether the deactivating carbon types are hydrogenated structures or not, their morphology, location and distribution over the nickel nanoparticles. We embark on answering some of these questions by testing our nickel catalyst at low temperature and rather harsh conditions. By harsh conditions is meant that we include no mild oxidants such as CO_2 nor H_2O which may limit carbon deposition[11] in our methanation flow. As CO_2 and H_2O can be expected in the feed for the methanation reactor in industry due to the feed gas coming from coal or biomass gasifiers, our conditions are harsher than those in an industrial context; already a low percentage of CO in H_2 at atmospheric pressure and low temperature can result in a significant catalyst deactivation over a few days.[57] Thereby we provoke deactivating carbon formation at low temperature, and building on the prior knowledge, we set out to provide new information on the nature of the deactivating carbon in order to answer these questions.

EXPERIMENTAL SECTION

Experiments were performed using a catalyst which was prepared via a nickel nitrate impregnation route with 22 wt % Ni supported on a γ-alumina carrier. Potential poisons for the methanation reaction, S and K, were measured by ICP-OES to be below 50 ppmw in the fresh catalyst. The fresh catalyst had a total surface area of 160 m^2/g, as measured by BET on a Quantachrome Autosorb-3 instrument, and a pore volume of 450 mL/kg with an average pore diameter of 55 Å, as characterized by Hg porosimetry using a Micromeritics Autopore IV 9520 instrument. The nickel particle size in the fresh catalyst was 8 nm as determined by X-ray diffraction. The Ni surface area was determined by the sulfur capacity method,[26] and found to be 13 $m^2/g \pm 10\%$ (2σ).

For testing the catalyst was diluted to stay below 16% CO conversion in a glass-lined steel plugflow reactor with an inner diameter of 3.87 mm. Catalyst and additional γ-alumina inert material were ground and selected by US mesh 140 and 50 (i.e., sizes between 100 and 300 μm) and for typical experiments 12.5 mg catalyst and 122 mg alumina were weighed off resulting in a bed height of 1.5 cm. Prior to experiments the temperature profile within the reactor was determined so the catalyst bed was placed within the uniform temperature zone of about 5 cm. For experiments high purity gases were led through a reduced $Cu/Zn/Al_2O_3$ methanol catalyst loaded in a cleaning unit to remove potential trace elements such as sulfur and immediately in front of the reactor a commercial carbonyl filter was installed provided by the Pall Corporation.

Ion scattering spectroscopy (ISS)/low energy ion scattering (LEIS) measurements and X-ray photoelectron spectroscopy (XPS) were done to demonstrate sulfur-free conditions on nickel foils exposed to the same test conditions. These characterization techniques were carried out in the same ultrahigh vacuum system provided by Scienta Omicron. XPS was performed using a SPECS XR 50 X-ray gun coupled to Omicron NanoSAM 7 channel energy analyzer while ISS employed an Omicron ISE100 ion gun.

The activity experimental series were started by a TPH to 1123 K with a temperature ramping rate of 5 K/min, followed by methanation at 573 K and 3 bar at $H_2/CO = 4$ in 50% Ar with $p_{CO} = 0.3$ bar, followed by another TPH to 1123 K. X-ray diffraction results showed that the first TPH resulted in Ni crystallite sizes increasing from the starting 8 nm to ∼11 nm but hereafter the crystallite size was stable despite multiple temperature ramps to 1123 K. On the basis of the crystallite size increase, the Ni surface area for a TPH-reduced catalyst was calculated to be about 10 m^2/g. The XRD measurements were performed with a PANalytical X'Pert PRO diffractometer with a Cu anode.

Temperature in the activity setup was measured by a type K thermocouple inside the reactor immediately below the catalyst bed and the pressure was controlled by a Baumann 51000 control valve. TPH was done with 25% H_2 in Ar with a total flow of 40 mL/min equal to a GHSV of ∼20 000/h and with a ramp of 5 K/min. TPHs were ended by cooling down in the H_2/Ar mix unless otherwise stated. Flows during methanation were 10 mL/min CO, 40 mL/min H_2 and 50 mL/min Ar resulting in a GHSV of ∼50 000/h. In between the reducing TPH and methanation, the reactor was cooled in H_2/Ar and pressure was built up in 40 mL/min H_2 and 60 mL/min Ar. When the required pressure of 3 bar was reached, the methanation was started by introducing the CO flow and reducing Ar to 50 mL/min. Methanation experiments were terminated by relieving pressure in methanation flow at reaction temperature (573 or 543 K) and pumping out as well as cooling down once close to ambient pressure. It was

DOI: 10.1021/acs.jpcc.7b03754
J. Phys. Chem. C XXXX, XXX, XXX−XXX

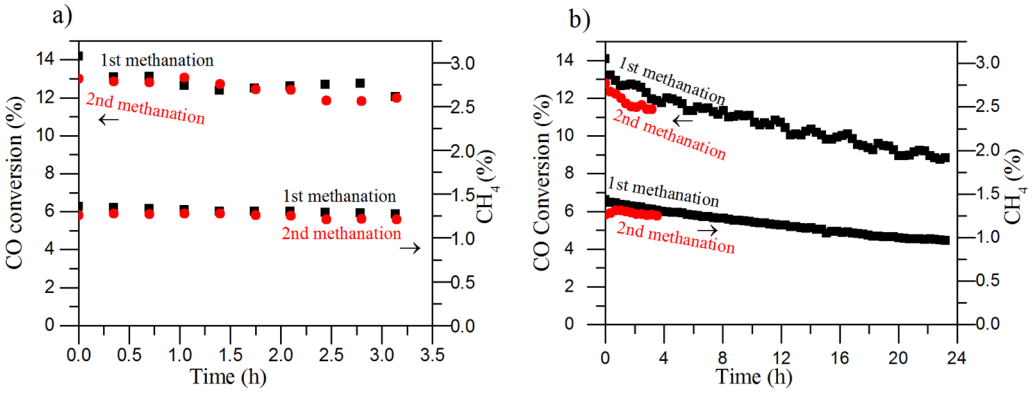

Figure 1. (a) CO conversion (left *y*-axis) and methane % (right *y*-axis) for methanation experiments of just under 4 h, separated by TPH to 823 K, and continued hydrogen treatment at this temperature for 6 h (b) CO conversion (left *y*-axis) and methane % (right *y*-axis) for methanation experiments of 24 h, separated by TPH to 823 K, and continued hydrogen treatment at this temperature for 8 h.

established that any effect of the shutdown procedure is only relevant to carbon desorbing in TPH below the reaction temperature, and does therefore not affect the deactivating carbon types which desorb above 573 K in TPH as discussed in the Introduction. Experiments where the catalyst was exposed to either methane or carbon monoxide were done at ambient pressure and 500 K with a total flow of 100 mL/min on a TPH reduced catalyst that had been cooled while pumping out and flushing with Ar to limit residual hydrogen on the surface.

The exit gas of the reactor was analyzed on stream simultaneously by a quadrupole mass spectrometer (MS) through a glass capillary, the principle of which as described by Kasemo,[27] and an Agilent gas chromatograph (GC) equipped with five columns (two 3 ft Hayesep, 10 ft Hayesep, PPQ-HT CP7557, and 9 ft Molsieve 5A) leading to either one of the two FIDs or the one TCD. Preselected masses were recorded in the MS and the GC provided evidence for whether more species were reacted off. However, as each injection into the GC occurs only every 20 min, the mass spectrometer was required for high time resolution.

RESULTS

Experiments were carried out to gain more fundamental knowledge on carbon formation during methanation and therefore needed to be free from the influence of sulfur. All tubes had been heated in a flow of pure hydrogen, and as mentioned, the high-purity gases were led through a reduced $Cu/Zn/Al_2O_3$ catalyst to remove trace elements such as sulfur. To further substantiate that experiments were sulfur-free, different kinds of experiments were done. A catalyst was regenerated after about 4 h of methanation (573 K, 3 bar, 1:4 ratio of $CO:H_2$, p_{CO} = 0.3 bar) by a TPH up to 823 K and held at 823 K for 6 h, because below 923 K, sulfur is known to be immobile.[28] As will be clear later, 823 K is sufficient to remove all carbon deposited during methanation, and thus, activity is regained if sulfur is not the culprit for deactivation. The result is summarized in Figure 1a as the CO conversion and methane percentage in the exit gas during methanation before the TPH up to 823 K and after. As the conversion returns to nearly the same level, the experiment supports that the setup is sulfur-free. Similarly, a catalyst after 24 h of methanation was regenerated by a TPH up to 823 K and held at 823 K for 8 h. In Figure 1b, it is seen that the CO conversion in the second methanation experiment amounts to a ∼6% lower relative conversion compared with the first. The oscillations in the CO conversion correlate with the change in pressure in the outlet resulting from when the GC does an injection but have not been further investigated. Since some minor sintering may be expected during an extended long methanation experiment and as 11 h CO_2 methanation with H_2/CO_2 = 5 at 550 K experiments showed no deactivation, the experiment seen in Figure 1b supports that the setup is sulfur-free. With respect to other potential reasons for loss of catalyst activity, Ni loss due to nickel carbonyl formation was excluded to occur because ICP-MS analysis showed no loss of nickel and activity was recovered within ∼8% after a 40 h methanation experiment by TPH to 1123 K. Experiments with a nickel foil in front of the catalyst bed were also performed, and the sulfur content of the foil was analyzed by XPS and ISS. These results, which can be found in the Supporting Information, further proved a negligible sulfur influence.

Having established that any influence of sulfur can be assumed to be negligible, we turn to results from testing the performance of the catalyst during methanation. The catalysts were tested for methanation at 3 bar and 573 K with 1:4 CO to H_2 ratio and a CO partial pressure of 0.3 bar for varying length of time, and results for a 60-h methanation are presented in Figure 2a. Activity data were generally analyzed from the gas chromatograph (GC) spectra and data for different methanation experiments were essentially identical. The main hydrocarbon components in the exit gas measured by the GC and CO conversion are plotted versus time on stream (TOS) in Figure 2a, and it is clear that methane is the primary hydrocarbon product by more than an order of magnitude. The methane concentration was over the 60 h of testing reduced by about 45% due to catalyst deactivation. The methane signal in Figure 2a is fitted as an exponential decay curve and by this fit the ratio of the higher hydrocarbons to methane is plotted in Figure 2b. Interestingly, it is observed that, whereas the alkane production (CH_4, C_2H_6, and C_3H_8) and CO conversion decrease at fairly similar relative rates over time, the absolute alkene (C_2H_4 and C_3H_6) rate of production actually increases with catalyst deactivation and loss of methanation activity. Similar results were found for methanation experiments at 543 K. Clearly, the catalyst hydrogenation activity drops as a result of the deactivation, affecting the higher hydrocarbon alkane-to-alkene ratio. The results bear resemblance with the increased alkene selectivity with catalyst deactivation observed in carbon deactivation studies of a Co-based FT catalyst.[29]

DOI: 10.1021/acs.jpcc.7b03754
J. Phys. Chem. C XXXX, XXX, XXX−XXX

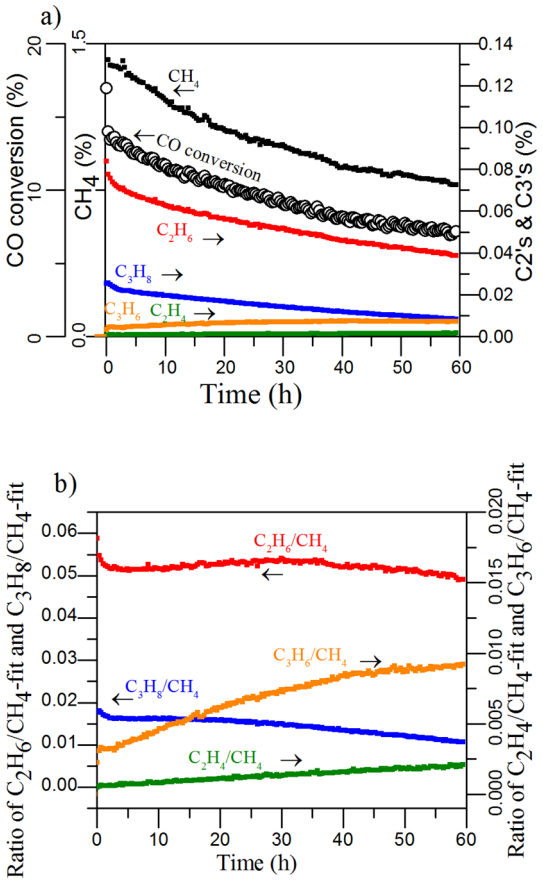

Figure 2. 60-h methanation experiment at 573 K and 3 bar, p_{CO} = 0.3 bar, H_2/CO = 4: (a) main hydrocarbon products and CO conversion versus time on stream; (b) alkane and alkene-to-methane ratio versus time on stream.

Succeeding a methanation experiment, temperature-programmed hydrogenation (TPH) was used to hydrogenate the deposited carbon into methane. In Figure 3, the results of such TPHs succeeding methanation experiments of varying duration are presented where each result is for a different experiment with fresh catalyst loaded initially. On the left in Figure 3a, the methane MS signals (m/z = 15) are plotted versus the temperature at which they were detected and three very characteristic peak temperatures are observed: ~460, ~650, and ~775 K. No hydrocarbons apart from methane were detected by either the MS or the GC. Catalysts carrying out methanation at 573 K shorter than 8 h display only the 460 and 650 K peaks, while catalysts that were tested for longer than 24 h no longer have a distinct 650 K peak; the 8- and 24-h experiments clearly have all three peaks. We note that the peak temperatures stay essentially fixed in all TPHs. In particular, the ~775 K peak does not shift toward higher temperatures despite drastically increasing magnitude; this differs from the behavior of the discussed β-carbon peak in the work by McCarty et al.,[22] induced by either pure CO or C_2H_4 dissociation.

Before settling on the final experimental procedure used for the results in Figure 3a, ten identical experiments starting with fresh catalyst every time were performed to judge experiment reproducibility. Each started by a reducing TPH, followed by 1 h methanation, followed by TPH, and the results of the second TPH in these tests are presented in Figure 3b. The results show good reproducibility.

We report that the same characteristic TPH peaks after methanation carried out at 573 K, H_2/CO = 4, and p_{CO} = 0.3 bar were also observed when performing methanation at 543 K. Similar deactivation rates were found for methanation at 543 and 573 K, and although the 775 K carbon TPH peak growth rate was slower at 545 K, the intensity of the ~650 K TPH peak was significantly higher. After 8 h of methanation at 573 K, roughly 3.5 times more 775 K TPH peak carbon was observed on the catalyst compared with after 10 h of methanation at 545 K, but only half the 650 K TPH peak carbon compared with methanation at 545 K.

In order to relate the methane signals in TPHs to known surface carbon species, a reduced catalyst was exposed to a low dose of methane at 500 K following the principles of surface science experiments. It is expected that a saturation layer of Ni surface carbide, Ni_2C (~0.5 C/Ni_{surf}) can be formed under these conditions.[30,31] The results based on 10 min, 2 and 10 h of exposure to 5% CH_4 in Ar are presented in Figure 4a and in Figure 4b the results for 5% CO in Ar for 2 h, and 5% CH_4 in Ar for 2 h (the red curve in Figure 4a) are presented. All curves in Figure 4 exhibit a strong peak at around 440 K and a significantly smaller feature at around 700 K. It is clear that the amount of carbon reacted off by hydrogen is quite insensitive to the duration of the 5% methane exposure beyond 2 h, supporting that a saturation layer of Ni surface carbide is formed. The second peak centered at ~700 K may be related to

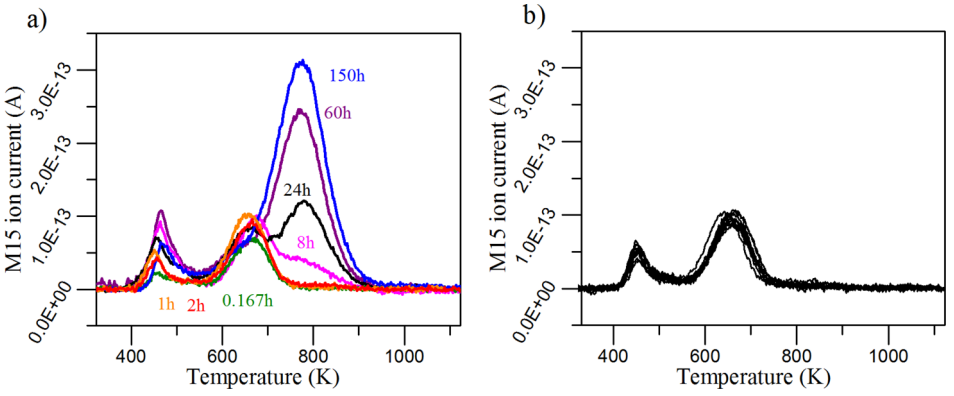

Figure 3. Methane signals (m/z = 15) during TPH succeeding methanation at three bar and 573 K. Mass 15 is measured every 26 s and the temperature is ramped up with 5 K/min: (a) TPH post methanation of various duration; (b) multiple TPHs subsequent to 1 h of methanation. Each experiment was performed on a fresh sample.

DOI: 10.1021/acs.jpcc.7b03754
J. Phys. Chem. C XXXX, XXX, XXX−XXX

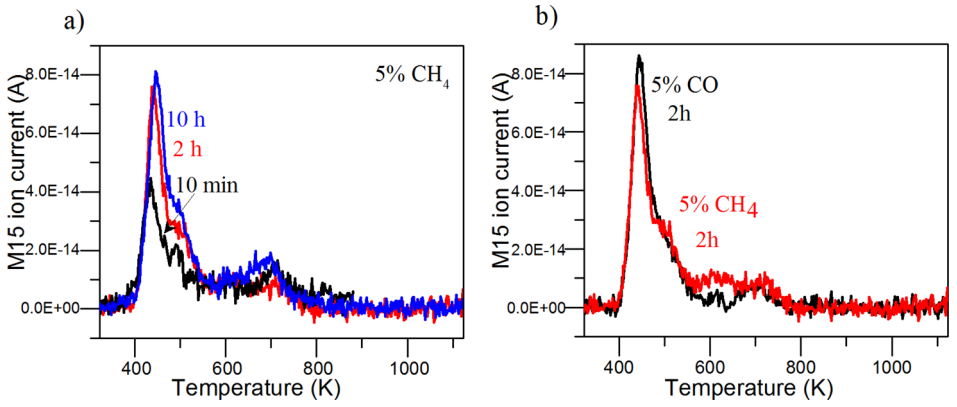

Figure 4. Methane signals during TPH following exposure at 500 K of (a) 5% CH_4 for various durations and (b) 5% CO for 2 h and 5% CH_4 for 2 h.

less reactive polymerized carbon. However, this carbon hydrogenation feature differs significantly from the ∼650 K feature in Figure 3a by having a peak maximum at significantly higher temperature ($\Delta T \sim 50$ K), and a distinctly larger full width half-maximum, approximately 100 K for the ∼650 K feature in Figure 3a vs around 200 K for the ∼700 K feature in Figure 4.

In the attempt to quantify the carbidic carbon and hereby gain insight into its nature, the curves in Figure 4 were fitted as a first order approximation with Gaussian peaks. The result for a Gaussian multiple peak fit of the 5% CH_4 for a 10 h curve is presented in Figure 5.

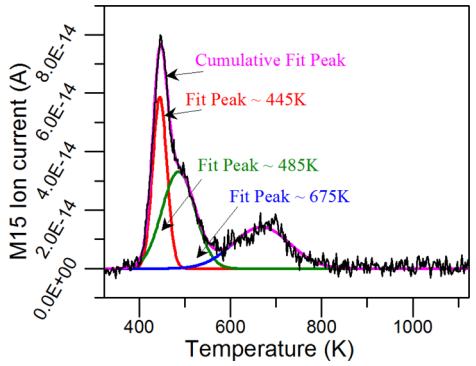

Figure 5. Resulting TPH curve following exposing the catalyst to 5% CH4 for 10 h fitted as first order approximation Gaussian peaks in order to quantify the carbon deposition.

It is clear from the fit in Figure 5 that the strongest peak is in fact two peaks which we interpret as the formation of the expected surface carbon and the second feature as carbon beneath the surface; dissolved carbon. The first peak of the fit in the strongest feature is at ∼445 K and yields a ratio between carbon and surface nickel of 0.43 in good agreement with Klink et al.[31] who found a carbon surface density of 0.45 ML for surface carbide (Ni_2C) on the Ni(100) surface. The second peak at ∼485 K yields a ratio of 0.7 C/Ni_{surf}. In the attempt to confirm dissolved carbon in the nickel, ex-situ X-ray diffraction measurements were performed. The resulting XRD patterns showed no evidence of the formation of bulk carbide (Ni_3C). Instead, all nickel-related diffraction peaks were shifted compared with the position of the reduced nickel diffraction peaks, consistent with an increased nickel lattice parameter. All samples that had been exposed to carbon-containing gases showed an increase in nickel lattice parameter. For example, the Ni(111) lattice parameter was by simple peak position analysis after 5% CH_4 treatment found to have increased by ≈0.02 Å; similar XRD observations for hydrogenation of CO over Ni were done by Znak et al.[32] Other groups have in similar ways during both methanation and CO disproportion reported carbon dissolved into the bulk of nickel or described carbon as interstitially bound.[33−35] We note that this suggestion of dissolved carbon is sufficient for this work but that additional work and analysis have been done and will be published separately. Although bulk carbide could not be detected by XRD, whereas dissolved carbon could explain the data, this does not entirely exclude the presence of bulk carbide in the samples. Bulk carbide could be present alongside with the dissolved carbon in the form of domains too small to give a significant contribution to the diffraction pattern, or may have been present during reaction conditions but not in the ex-situ samples.

For the purpose of determining whether any of the surface carbon species deposited during methanation was hydrogenated, Ar TPDs instead of TPHs were performed succeeding the methanation tests to measure any hydrogen desorption.

Simultaneously depressurizing to atmospheric pressure and turning off the reactor heating elements to cool down immediately after a methanation experiment, the setup was pumped down to some few millibars and subsequently flushed with Ar three times with Ar evacuation in between. Once the reactor was below 373 K, the temperature was ramped up to 1123 K with 5 K/min in Ar. To determine any background, two experiments identical in design, except only flowing H_2 and Ar during "methanation" for 2 and 24 h respectively, were performed. In Figure 6, the hydrogen signal ($m/z = 2$) during the Ar TPDs following 2, 24, and 80 h of methanation at 573 K, $H_2/CO = 4$, and $p_{CO} = 0.3$ bar are plotted as a function of temperature. Two hours of H_2 and Ar flow resulted in no significant H_2 TPD background peak shape differences compared with 24 h, and thus, only the 24-h signal is presented. The signals of CO ($m/z = 28$) and CO_2 ($m/z = 44$) for the 80 h of methanation have also been plotted because any formation of CO and CO_2 can suggest decomposition of surface oxygenates, for example formate.

The two main H_2 desorption features observed for 2, 24, and 80 h of methanation essentially overlap in peak temperature with the 650 and 775 K surface carbon hydrogenation features in Figure 3a. The primary H_2 desorption peak centered at about 650 K after 2 h of methanation has its onset at the temperature at which methanation was carried out (573 K), while the TPDs after 24- and 80-h methanation experiments share this feature,

DOI: 10.1021/acs.jpcc.7b03754
J. Phys. Chem. C XXXX, XXX, XXX−XXX

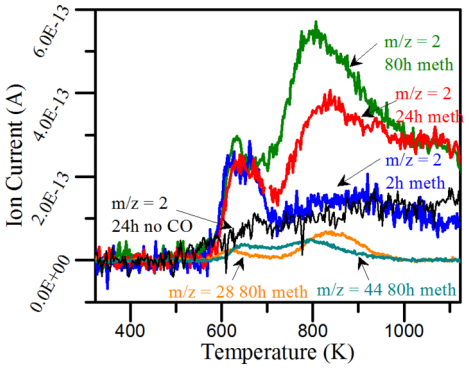

Figure 6. Hydrogen desorption (m/z = 2) as a function of temperature during an Ar TPD following methanation of 2, 24, and 80 h. The hydrogen background based on a similar experiment not containing CO is plotted in black. CO (m/z = 28) and CO_2 (m/z = 44) signals during the TPD following the 80 h methanation are plotted as well.

while also another much more intense and broader peak centered at ~775 K is detected. The curves do not return to the baseline within the applied temperature range up to 1123 K but do so eventually during cool down. Consistent with the complete lack of a ~775 K TPH peak in Figure 3a after 2 h of methanation, the H_2 TPD peak in Figure 6 after 2 h of methanation does essentially not differ from the H_2 "background" TPD curve above 700 K, suggesting that the carbon of the 650 K peak could be hydrogenated. The H/C ratio was approximated to as high as 2, but as some CO and CO_2 desorption is detected in the relevant H_2 desorption range, which could be due to the thermal decomposition of stable surface oxygenates, some additional hydrogen may be expected from such oxygenates. However, based on the TPH findings of Chen et al.[36] and Kistamurthy et al.,[37] the lack of methane desorption peaks in the region of 500−600 K in the TPHs in Figure 3a indicates few oxygenates on the surface, and neither methane (m/z = 15) nor acetone (m/z = 43) was observed during the TPD experiments as seen by Kistamurthy et al.[37] Also, we report that the H_2 desorption peaks cannot be explained by H_2O cracking in the MS as the m/z = 18 signal showed no similar features and its signal was much lower than that of m/z = 2. The second broad feature at 775 K is approximated to a staggering H/C ratio of 8, which cannot even be explained as a combination of hydrogenated carbon and surface oxygenates. OH-groups migrating from the alumina carrier to the nickel and decomposing there to oxidize carbon and the nickel surface with concomitant H_2 release may, however, explain the large hydrogen desorption above 700 K, and may also explain the difference at longer methanation run times compared with the Ar + H_2 treatments to determine background contribution from only H_2. Therefore, we are unable to assign the broad H_2 desorption feature above 700 K to the carbon type giving rise to the 775 K TPH peak.

DISCUSSION

McCarty and Wise[22] studied carbon deposited by CO and C_2H_4 on nickel catalysts by its reactivity with hydrogen. For the CO route they named the reactive carbon coming off at low temperature (470 K ± 20 K) as α-carbon and the less reactive coming off at 680 K ± 30 K as β-carbon. These carbon species were also observed for the C_2H_4 route, but at slightly higher temperatures with β-carbon now broad ranging from 600 to 800 K. In addition, they observed a peak at 55 K higher than the α-carbon (550 K) which they assigned to bulk carbide (Ni_3C). In this work, the high intensity feature in Figure 4 yields a peak assigned to surface carbide at ~445 K when the TPH curve is fitted by several Gaussian peaks but also a second peak at 485 K. The separation of about 40 K between peak 445 and 485 K in Figure 5 is similar to the 55 K McCarty et al. found at low carbon coverage. In contrast to McCarty et al., based on our XRD findings we do not assign the ~485 K peak to bulk carbide (Ni_3C) in our samples. We could not observe bulk carbide but measured an increased nickel lattice parameter and therefore we assign it to dissolved carbon. The 445 K peak matches reasonably well the low temperature feature at ~460 K in Figure 3, suggesting that they are in a similar state. We thus assign the lowest temperature peak in Figure 3a to carbidic carbon (atomic-like carbon) or α-carbon.[22]

In Figure 7, the areas of the peaks used to fit the TPH curves in Figure 3a converted to carbon-to-surface-nickel atomic ratio

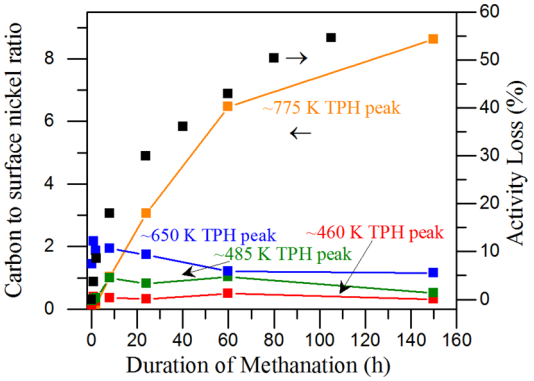

Figure 7. Area of the individual TPH peaks derived from Gaussian curve fits and converted to C/Ni_{surf} is plotted in color on the left y-axis for the respective methanation experiments with lines to guide the eye. Furthermore, the activity loss during the 150 h methanation experiment is plotted on the right y-axis.

is plotted for each TPH curve. The amount of carbon released from the catalyst under the TPH peak fits similar to the fitting in Figure 5 was determined by integrating over time, the molar flow of CH_4 as determined by the measured CH_4 concentration by MS, known pressure, and gas flows in the reactor. Additionally the activity loss of the 150 h methanation experiment is presented. As discussed in the Introduction, the specific degree of activity loss, though unsuitable in industry, is not a concern in this work since in industrial settings the gas composition from, e.g., coal/biomass gasifiers contains, besides CO and H_2, also significant amounts of the mild oxidants H_2O and CO_2 that drastically reduce the potential for carbon laydown.[11] It is clear in Figure 7 that, while the carbon amounts in the 460 K, 485 and 650 K TPH peaks are all relatively stable and low, it is the 775 K TPH peak that increases with time on stream. The shape of the activity loss curve and the 775 K peak development are very similar suggesting this peak comprises the main deactivating carbon. The carbon amount on the surface is, as expected, clearly increasing with time on stream. However, the trend seems to be leveling off which suggests a filling up of sites or surface. The 775 K TPH peak carbon after 150 h amounts to a large surface coverage of 8 C/Ni_{surf} or equivalently almost four layers of graphene that has a C/Ni_{surf} ratio of 2 on the Ni(111) surface. These amounts of carbon can be compared with the roughly five monolayers of deactivating

DOI: 10.1021/acs.jpcc.7b03754
J. Phys. Chem. C XXXX, XXX, XXX−XXX

carbon on Ni formed in ref 10, which, similar to our findings, could be removed by hydrogenation at 775 K.

In Figure 8, the activity loss experienced by the catalyst in the respective methanation runs is plotted as a function of the ratio

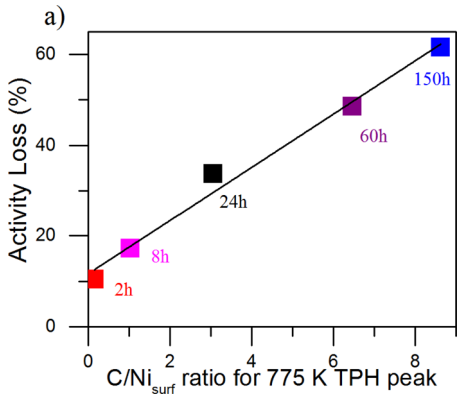

Figure 8. Activity loss during methanation as a function of carbon deposition related to the number of Ni surface atoms as calculated from specific Ni surface area and Ni(111) surface atoms density for the 775 K peak of the curves in Figure 3a.

of carbon to surface nickel atoms of the 775 K peak. The 150-h activity loss point is an extrapolation based on the activity from zero to 105 h as the GC had malfunctioned at that point, but MS confirmed that it is in the correct range.

In Figure 8, the relation is obviously linear, which is not surprising as it was already suggested in Figure 7 that the activity loss was related to the 775 K peak. However, the linear regression does not go through origo. Therefore, it seems as if the deactivation could also be due to the 650 K TPH peak carbon which is not unreasonable. The 650 K carbon species likely initiates the deactivation and there is likely an interdependence between the 650 and 775 K species. This is consistent with results for methanation at 545 K where more of the 650 K TPH peak carbon caused a similar deactivation despite less 775 K carbon compared with the 573 K methanation TPHs. An interdependence suggests a conversion of carbon species/morphologies over time: a short methanation run under the specified conditions was not sufficient to result in the 775 K TPH peak whereas after a long methanation run the 650 K TPH peak is less intense and only a mere shoulder riding on the more intense 775 K peak. This agrees well with the work by Yang et al.[25] where CH-species couple and form C_2H_2 and eventually form imperfect benzene, i.e., partially dehydrogenated C_6-rings which then further polymerize into larger cyclic hydrocarbons; the most stable type of surface carbon on Ni would eventually become more and more graphene-like.[38] Although the carbon-to-surface-nickel ratio calculation suggests eight carbons per surface nickel atom, the catalyst was only deactivated by approximately 55% suggesting carbon deposition on not only the most active Ni methanation sites, i.e., the Ni step sites.[1,39] Alternatively, the carbon growth distribution over the Ni nanoparticle surfaces is strongly inhomogeneous.

Although we, to the best of our knowledge, for the first time have established a direct and linear correlation between the degree of Ni catalyst deactivation and quantitative amount of polymerized carbon deposited during low-temperature CO methanation conditions, our findings are fully in line with recent studies of carbon formation on and deactivation of Co-based Fischer–Tropsch (FT) catalysts[29,40−42] and earlier FT catalyst deactivation results partially discussed and reviewed by, e.g. Saib et al.[43] and Weststrate et al.[23] In all these recent deactivation studies involving catalyst characterization via carbon hydrogenation by TPH, carbon hydrogenation peaks in the 650−800 K range was found to be related to the deactivation of the Co-based FT catalyst, similar to our results on Ni and those discussed in the Introduction. Transmission electron microscopy studies of deactivated FT catalysts[41] clearly showed a polymeric, partly layered amorphous and partly more layered lamellar nature of thick carbon deposit layers on the Co particle surfaces. CH_x thermal dehydrogenation of more stable olefinic, aromatic and graphenic-like local configurations, molecules and thin films are found in the temperature range of 600−900 K[25,44−51] matching the temperatures of our TPD and TPH results. On the basis of our observations, it is not unreasonable to assign the carbon structure/morphology giving rise to the TPH and TPD peaks centered at ∼650 K to be related to a defective and partially dehydrogenated polycyclic aromatic hydrocarbon-like submonolayer, whereas the TPH peak centered at ∼775 K can be assigned to more graphene-like carbon of both mono- and multilayer character. Both morphologies are expected to grow as rather open structures consisting of smaller patches randomly distributed over the Ni surfaces given that a significant amount of the sites active for methanation, i.e., the Ni step sites[1,39] are still available to carry out the methanation reaction at an average carbon surface coverage on Ni corresponding roughly to four monolayers of graphene. The early monolayer structures may resemble the randomly distributed patchy polymeric carbon structures studied by scanning tunneling microscopy on surfaces such as Ru(0001),[48] Pt(111),[52] and, although not with an observable polymeric carbon low energy electron diffraction pattern for C_2H_4 exposures, also on Ni(111).[53] They may also resemble various open structures, although not partially hydrogenated, suggested by kinetic Monte Carlo studies of carbon deposition on Co(0001) under FT conditions.[54] The sequence of dehydrogenation and polymerization events of smaller surface hydrocarbons into polycyclic aromatics and further to graphene patches that we believe is taking place on Ni under low-temperature CO methanation conditions have very recently been captured in beautiful structural detail on Rh(111).[55]

Besides the potentially open, patchy, and randomly or strongly inhomogeneously distributed (hydro)carbon structures our data suggests, we note that the significantly higher local hydrogen coverage, and thus faster hydrogenation rates, expected near Ni step sites compared with terrace sites under methanation conditions[1] may also contribute to a locally improved resistance toward carbon deposition near step sites. The initial growth mechanism for these larger (hydro)carbon morphologies could very well follow along the CH* surface coupling route suggested by Weststrate et al.[23,24] for deactivating carbon formation on Co under Fischer–Tropsch conditions, with the deactivating carbon formation surface chemistry similar to that taking place on Ni.[25,56]

CONCLUSION

In the presented work:

- We have taken great care to ensure that the experimental setup is sulfur-free and thus that the studied carbon deposition during low temperature CO methanation is free from the influence of sulfur.

DOI: 10.1021/acs.jpcc.7b03754
J. Phys. Chem. C XXXX, XXX, XXX−XXX

- We show that TPH curves hydrogenating carbon off the catalyst after methanation exhibit three distinct peaks: at ~460, ~650, and ~775 K where the high temperature carbon types (centered at 650 and 775 K) are interdependent. There is a linear correlation between carbon deposition and catalyst deactivation, from which we discern, that the primary cause for deactivation is the 775 K TPH peak carbon which is not preferentially deposited at the Ni step sites, nor uniformly distributed over the Ni nanoparticle surfaces.
- We suggest that while the low temperature TPH peak (centered at 460 K) formed during methanation is due to carbidic carbon as well as carbon dissolved in the nickel, Ar TPDs suggest that the 650 K TPH peak carbon built up during methanation contains hydrogen, and it could thus be of a polycyclic aromatic-like nature. We assign the 775 K TPH peak carbon to be more graphene-like in nature.

■ ASSOCIATED CONTENT

Supporting Information

The Supporting Information is available free of charge on the ACS Publications website at DOI: 10.1021/acs.jpcc.7b03754.

ISS (Figure S1a) and XPS spectra (Figure S1b) of nickel foils, presented to support the conclusion of no sulfur poisoning influence in the experiments (PDF)

■ AUTHOR INFORMATION

Corresponding Author

*(I.C.) E-mail: ibchork@fysik.dtu.dk.

ORCID

Ib Chorkendorff: 0000-0003-2738-0325

Notes

The authors declare no competing financial interest.

■ ACKNOWLEDGMENTS

This work was supported by a research grant (9455) from VILLUM FONDEN and was cofunded by Haldor Topsoe A/S.

■ REFERENCES

(1) Wind, T.; Falsig, H.; Sehested, J.; Moses, P. G.; Nguyen, T. T. M. Comparison of Mechanistic Understanding and Experiments for CO Methanation over Nickel. *J. Catal.* **2016**, *342*, 105−116.

(2) Gao, J.; Liu, Q.; Gu, F.; Liu, B.; Zhong, Z.; Su, F. Recent Advances in Methanation Catalysts for the Production of Synthetic Natural Gas. *RSC Adv.* **2015**, *5*, 22759−22776.

(3) Kopyscinski, J.; Schildhauer, T. J.; Biollaz, S. M. A. Production of Synthetic Natural Gas (SNG) from Coal and Dry Biomass − A Technology Review from 1950 to 2009. *Fuel* **2010**, *89*, 1763−1783.

(4) Kazempoor, P.; Braun, R. J. Hydrogen and Synthetic Fuel Production Using High Temperature Solid Oxide Electrolysis Cells (SOECs). *Int. J. Hydrogen Energy* **2015**, *40*, 3599−3612.

(5) NREL *A Comparison of Hydrogen and Propane Fuels*; DO/EGO-102009-2813; 2009.

(6) Pedersen, K.; Skov, A.; Rostrup-Nielsen, J. R. Catalytic Aspects of High Temperature Methanation. *Prepr. Pap. Am. Chem. Soc., Div. Fuel Chem.* **1980**, *25*, 89−100.

(7) Bartholomew, C. H.; Pannell, R. B.; Fowler, R. W. Sintering of Alumina-Supported Nickel and Nickel Bimetallic Methanation Catalysts in H2/H2O Atmospheres. *J. Catal.* **1983**, *79*, 34−46.

(8) Rostrup-Nielsen, J. R.; Pedersen, K.; Sehested, J. High Temperature Methanation Sintering and Structure Sensitivity. *Appl. Catal., A* **2007**, *330*, 134−138.

(9) Nguyen, T. T. M.; Wissing, L.; Skjøth-Rasmussen, M. High Temperature Methanation: Catalyst Considerations. *Catal. Today* **2013**, *215*, 233−238.

(10) Gierlich, H. H.; Fremery, M.; Skov, A.; Rostrup-Nielsen, J. R. Deactivation Phenomena of a Ni-based Catalyst for High Temperature Methanation. *Stud. Surf. Sci. Catal.* **1980**, *6*, 459−469.

(11) Bartholomew, C. H. Carbon Deposition in Steam Reforming and Methanation. *Catal. Rev.: Sci. Eng.* **1982**, *24*, 67−112.

(12) Sehested, J. Four Challenges for Nickel Steam-Reforming Catalysts. *Catal. Today* **2006**, *111*, 103−110.

(13) Mirodatos, C.; Dalmon, J. A.; Martin, G. A. Nature and Role of Carbon Species During CO and CO-H2 Reactions over Ni/SiO2 Catalysts. *Stud. Surf. Sci. Catal.* **1984**, *19*, 505−512.

(14) Hayes, R. E.; Ward, K. J.; Hayes, K. E. The Nature of Surface Carbon on y-Alumina Supported Nickel Catalysts During CO-Disproportionation in the Presence and Absence of Hydrogen. *Appl. Catal.* **1986**, *20*, 123−131.

(15) Agnelli, M.; Swaan, H. M.; Marquez-Alvarez, C.; Martin, G. A.; Mirodatos, C. CO Hydrogenation on a Nickel Catalyst - II. A Mechanistic Study by Transient Kinetics and Infrared Spectroscopy. *J. Catal.* **1998**, *175*, 117−128.

(16) Mirodatos, C.; Praliaud, H.; Primet, M. Deactivation of Nickel-based Catalysts during CO Methanation and Disproportionation. *J. Catal.* **1987**, *107*, 275−287.

(17) Hayes, R. E.; Thomas, W. J.; Hayes, K. E. A Study of the Nickel-Catalyzed Methanation Reaction. *J. Catal.* **1985**, *92*, 312−326.

(18) Gardner, D. C.; Bartholomew, C. H. Kinetics of Carbon Deposition during Methanation of CO. *Ind. Eng. Chem. Prod. Res. Dev.* **1981**, *20*, 80−87.

(19) Moeller, A. D.; Bartholomew, C. H. Deactivation by Carbon of Nickel, Nickel-Ruthenium, and Nickel-Molybdenum Methanation Catalysts. *Ind. Eng. Chem. Prod. Res. Dev.* **1982**, *21*, 390−397.

(20) Erekson, E. J.; Sughrue, E. L.; Bartholomew, C. H. Catalyst Degradation in High Temperature Methanation. *Fuel Process. Technol.* **1981**, *5*, 91−101.

(21) Wentrcek, P. W.; McCarty, J. G.; Ablow, C. M.; Wise, H. Deactivation of Alumina-Supported Nickel and Ruthenium Catalysts by Sulfur Compounds. *J. Catal.* **1980**, *61*, 232−241.

(22) McCarty, J. G.; Wise, H. Hydrogenation of Surface Carbon on Alumina-Supported Nickel. *J. Catal.* **1979**, *57*, 406−416.

(23) Weststrate, C. J.; Ciobîca, I. M.; Saib, A. M.; Moodley, D. J.; Niemantsverdriet, J. W. Fundamental Issues on Practical Fischer−Tropsch Catalysts: How Surface Science Can Help. *Catal. Today* **2014**, *228*, 106−112.

(24) Weststrate, C. J.; van Helden, P.; Niemantsverdriet, J. W. Reflections on the Fischer−Tropsch Synthesis: Mechanistic Issues from a Surface Science Perspective. *Catal. Today* **2016**, *275*, 100−110.

(25) Yang, Q. Y.; Maynard, K. J.; Johnson, A. D.; Ceyer, S. T. The Structure and Chemistry of CH3 and CH Radicals Adsorbed on Ni(111). *J. Chem. Phys.* **1995**, *102*, 7734−7749.

(26) Rostrup-Nielsen, J. R. *Steam Reforming Catalysts: an Investigation of Catalysts for Tubular Steam Reforming of Hydrocarbons.*; Teknisk Forlag: 1975; p 240.

(27) Kasemo, B. Quartz Tube Orifice Leaks for Local, Fast-Response Gas Sampling to Mass Spectrometers. *Rev. Sci. Instrum.* **1979**, *50*, 1602−1604.

(28) Christensen, T. S.; Rostrup-Nielsen, J. R. In *Deactivation and Testing of Hydrocarbon-Processing Catalysts*; ACS Symposium Series; O'Connor, P., Takatsuka, T., Woolery, G. L., Eds.; American Chemical Society: 1996; Chapter 13, pp 186−200.

(29) Lee, D.-K.; Lee, J.-H.; Ihm, S.-K. Effect of Carbon Deposits on Carbon Monoxide Hydrogenation over Alumina-Supported Cobalt Catalyst. *Appl. Catal.* **1988**, *36*, 199−207.

(30) Alstrup, I.; Chorkendorff, I.; Ullmann, S. Interaction of Hydrogen with Carbidic Carbon on Ni(100). *Surf. Sci.* **1993**, *293*, 133−144.

(31) Klink, C.; Stensgaard, I.; Besenbacher, F.; Lægsgaard, E. Carbidic Carbon on Ni(110): an STM Study. *Surf. Sci.* **1996**, *360*, 171−179.

DOI: 10.1021/acs.jpcc.7b03754
J. Phys. Chem. C XXXX, XXX, XXX−XXX

(32) Znak, L.; Kaszkur, Z.; Zieliński, J. Evolution of Metal Phase in the Course of CO Hydrogenation on Potassium Promoted Ni/Al2O3 Catalyst. *Catal. Lett.* **2010**, *136*, 92−95.
(33) Cale, T. S. Nickel Crystallite Thermometry during Methanation. *J. Catal.* **1984**, *90*, 40−48.
(34) Kuijpers, E. G. M.; Kock, A. J. H. M.; Nieuwesteeg, M. W. C. M. A.; Geus, J. W. Disproportionation of CO on Ni/SiO2: Kinetics and Nature of the Deposited Carbon. *J. Catal.* **1985**, *95*, 13−20.
(35) Martin, G.-A.; Imelik, B. Adsorption of Hydrocarbons and Various Gases on Ni-SiO2 Catalysts Studied by High Field Magnetic Methods. *Surf. Sci.* **1974**, *42*, 157−172.
(36) Chen, B.; Falconer, J. L. Hydrogenation of Organic Oxygenates on Ni/Al2O3 and Ni/SiO2 Catalysts. *J. Catal.* **1994**, *147*, 72−81.
(37) Kistamurthy, D.; Saib, A. M.; Moodley, D. J.; Preston, H.; Ciobîca, I. M.; van Rensburg, W. J.; Niemantsverdriet, J. W.; Weststrate, C. J. The Role of Carboxylic Acid in Cobalt Fischer−Tropsch Synthesis Catalyst Deactivation. *Catal. Today* **2016**, *275*, 127−134.
(38) Bengaard, H. S.; Nørskov, J. K.; Sehested, J.; Clausen, B. S.; Nielsen, L. P.; Molenbroek, A. M.; Rostrup-Nielsen, J. R. Steam Reforming and Graphite Formation on Ni Catalysts. *J. Catal.* **2002**, *209*, 365−384.
(39) Andersson, M. P.; Abild-Pedersen, F.; Remediakis, I.; Bligaard, T.; Jones, G.; Engbæk, J.; Lytken, O.; Horch, S.; Nielsen, J. H.; Sehested, J.; et al. Structure Sensitivity of the Methanation Reaction: H2-Induced CO Dissociation on Nickel Surfaces. *J. Catal.* **2008**, *255*, 6−19.
(40) Moodley, D. J.; van de Loosdrecht, J.; Saib, A. M.; Overett, M. J.; Datye, A. K.; Niemantsverdriet, J. W. Carbon Deposition as a Deactivation Mechanism of Cobalt-Based Fischer−Tropsch Synthesis Catalysts under Realistic Conditions. *Appl. Catal., A* **2009**, *354*, 102−110.
(41) Fei Tan, K.; Xu, J.; Chang, J.; Borgna, A.; Saeys, M.; et al. Carbon Deposition on Co Catalysts during Fischer−Tropsch Synthesis: A Computational and Experimental Study. *J. Catal.* **2010**, *274*, 121−129.
(42) Keyvanloo, K.; Fisher, M. J.; Hecker, W. C.; Lancee, R. J.; Jacobs, G.; Bartholomew, C. H. Kinetics of Deactivation by Carbon of a Cobalt Fischer−Tropsch Catalyst: Effects of CO and H2 Partial Pressures. *J. Catal.* **2015**, *327*, 33−47.
(43) Saib, A. M.; Moodley, D. J.; Ciobîca, I. M.; Hauman, M. M.; Sigwebela, B. H.; Weststrate, C. J.; Niemantsverdriet, J. W.; Van De Loosdrecht, J. Fundamental Understanding of Deactivation and Regeneration of Cobalt Fischer−Tropsch Synthesis Catalysts. *Catal. Today* **2010**, *154*, 271−282.
(44) Zhao, W.; Gebhardt, J.; Späth, F.; Gotterbarm, K.; Gleichweit, C.; Steinrück, H.-P.; Görling, A.; Papp, C. Reversible Hydrogenation of Graphene on Ni(111)-Synthesis of Graphone. *Chem. - Eur. J.* **2015**, *21*, 3347−3358.
(45) Patera, L. L.; Bianchini, F.; Troiano, G.; Dri, C.; Cepek, C.; Peressi, M.; Africh, C.; Comelli, G. Temperature-Driven Changes of the Graphene Edge Structure on Ni(111): Substrate vs Hydrogen Passivation. *Nano Lett.* **2015**, *15*, 56−62.
(46) Curcio, D.; Omiciuolo, L.; Pozzo, M.; Lacovig, P.; Lizzit, S.; Jabeen, N.; Petaccia, L.; Alfè, D.; Baraldi, A. Molecular Lifting, Twisting, and Curling during Metal-Assisted Polycyclic Hydrocarbon Dehydrogenation. *J. Am. Chem. Soc.* **2016**, *138*, 3395−3402.
(47) Rim, K. T.; Siaj, M.; Xiao, S.; Myers, M.; Carpentier, V. D.; Liu, L.; Su, C.; Steigerwald, M. L.; Hybertsen, M. S.; McBreen, P. H.; et al. Forming Aromatic Hemispheres on Transition-Metal Surfaces. *Angew. Chem., Int. Ed.* **2007**, *46*, 7891−7895.
(48) Günther, S.; Dänhardt, S.; Ehrensperger, M.; et al. A High-Temperature Scanning Tunneling Microscopy Study of the Ordering Transition of an Amorphous Carbon Layer into Graphene on Ru (0001). *ACS Nano* **2013**, *7*, 154−164.
(49) Buijnsters, J. G.; Gago, R.; Redondo-Cubero, A.; Jiménez, I. Hydrogen Stability in Hydrogenated Amorphous Carbon Films with Polymer-like and Diamond-like Structure. *J. Appl. Phys.* **2012**, *112*, 093502.
(50) Peter, S.; Günther, M.; Richter, F. A Comparative Analysis of a-C:H Films Deposited from Five Hydrocarbons by Thermal Desorption Spectroscopy. *Vacuum* **2012**, *86*, 667−671.
(51) Zecho, T.; Güttler, A.; Küppers, J. A TDS Study of D Adsorption on Terraces and Terrace Edges of Graphite (0 0 0 1) Surfaces. *Carbon* **2004**, *42*, 609−617.
(52) Land, T. A.; Michely, T.; Behm, R. J.; Hemminger, J. C.; Comsa, G. Direct Observation of Surface Reactions by Scanning Tunneling Microscopy: Ethylene - Ethylidyne - Carbon Particles - Graphite on Pt (111). *J. Chem. Phys.* **1992**, *97*, 6774−6783.
(53) Nakano, H.; Ogawa, J.; Nakamura, J. Growth Mode of Carbide from C2H4 or CO on Ni(111). *Surf. Sci.* **2002**, *514*, 256−260.
(54) Jansen, A. P.; Agrawal, R.; Spanu, L. Thermodynamics and Kinetics of Carbon Deposits on Cobalt: A Combined Density Functional Theory and Kinetic Monte Carlo Study. *Phys. Chem. Chem. Phys.* **2016**, *18*, 28515−28523.
(55) Wang, B.; König, M.; Bromley, C. J.; Yoon, B.; Treanor, M.-J.; Garrido Torres, J. A.; Caffio, M.; Grillo, F.; Früchtl, H.; Richardson, N. V.; et al. Ethene to Graphene: Surface Catalyzed Chemical Pathways, Intermediates, and Assembly. *J. Phys. Chem. C* **2017**, *121*, 9413.
(56) Steinbach, F.; Kiss, J.; Krall, R. Identification and Stability of CH3, CH2, and CH Species on Co and Ni Surfaces, a Pes Investigation. *Surf. Sci.* **1985**, *157*, 401−412.
(57) Agrawal, P. K.; Fitzharris, W. D.; Katzer, J. R. Sulfur Poisoning and Carbon Deactivation of Alumina-Supported Ni, Co, Fe and Ru Catalysts in CO Hydrogenation. *Stud. Surf. Sci. Catal.* **1980**, *6*, 179−200.

DOI: 10.1021/acs.jpcc.7b03754
J. Phys. Chem. C XXXX, XXX, XXX−XXX

Paper 2

-in preparation

A study of carbon in and on nickel nanoparticles by XRD and TEM.

Authors:

Sine E. Olesen[1], Christian Danvad Damsgaard[1,2], Klas J. Andersson[3], and Ib Chorkendorff[1]

1: The Villum Center for the Science of Sustainable Fuels and Chemicals, Department of Physics, Technical University of Denmark, Building 312, 2800 Kgs. Lyngby, Denmark

2: Center for Electron Nanoscopy (CEN), Department of Physics, Technical University of Denmark, Building 307 & 314, 2800 Kgs. Lyngby, Denmark

3: Haldor Topsøe A/S, Nymøllevej 55, 2800 Kgs. Lyngby, Denmark

Abstract

Carbon formed during low temperature CO methanation as well as surface adsorption measurements with CO and CH_4 was studied for a Ni/Al_2O_3 catalyst. Previous work showed three carbon temperature programmed hydrogenation following methanation at ∼460 K, ∼650 K, and ∼775 K and the lowest temperature peak was assigned to carbidic carbon. Ex-situ XRD showed an increase in the nickel lattice constant indicative of dissolved carbon into the nickel particles. In-situ XRD performed on the same system to investigate the timescale over which this happened. Full profile analysis of the XRD patterns revealed a second nickel-related phase which had to be included to fit the profile sufficiently well. The formed carbon types were investigated by TEM & EELS as well.

Outline

- Introduction
- Ex situ x-ray diffraction (XRD) measurements. Patterns analysed by full profile analysis in TOPAS.
- In-situ XRD to observe the structural changes as they evolve.
- High resolution TEM supported by EELS to observe carbon and nickel
- Discussion on whether the expanded nickel crystal structure is indeed proof of dissolved carbon
- Conclusion

Appendix A

GC Configuration

Agilent Technologies	Valve System	Date :	S/N :
		Order No :	Item :

FLOW SOURCE	OVEN LEFT SIDE	INJECTION PORT	VALVE COMPARTMENT ALL VALVES SHOWN IN OFF POSITION	DETECTOR

○ = #87X

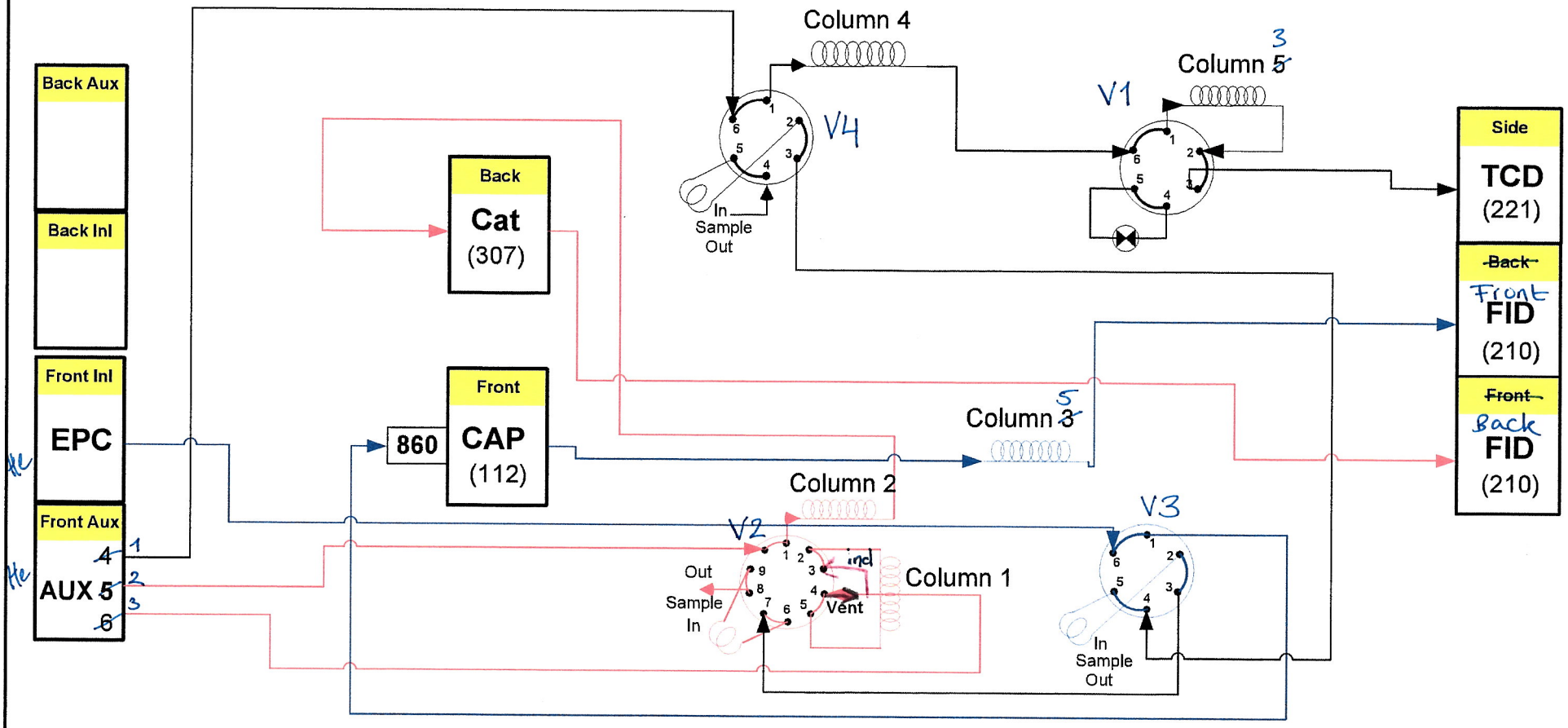

Blue Channel = MeOH, CH4, Dimethyl Ether, Ethane, Ethylene, C3s
Black Channel = CO, CO2, H2, Ar
Red Channel = Low CO and CO2 (backflush of everything else)

Column 1 3ft Hayesep Q 80/100
Column 2 10ft Hayesep Q 80/100
Column 3 PPQ-HT CP7557
Column 4 3ft Hayesep Q 80/100
Column 5 Molsieve 5A 9ft 80/100